Helium Line Emission Spectroscopy in the Prototype Material Plasma Exposure eXperiment for Evaluation of Electron Temperature and Density

A Dissertation Presented for the

Doctor of Philosophy

Degree

The University of Tennessee, Knoxville

Holly Beth Ray

May 2020

I wish to dedicate this doctoral thesis to my fiancé and future husband, Matthew Ramsey Flynn, for always being there for me. He has been my rock through the toughest of times and was always there to help motivate me when I believed moving forward was impossible. He encouraged me to not give up and was there to lend an ear or a shoulder.

\

Acknowledgements

I would not be where I am today if it was not for the incredible support of my family and friends. My parents, James and Nancy Ray, and sister, Elisha Locke, have always encouraged and supported me through everything. My fiancé and future husband, Matthew Flynn, and step-son, Jacob Flynn, have shown such amazing patience and support through all of this, and my friend, Guinevere Shaw, has always made a point to check in on my mental health and give me that extra laugh to get me through the day. I can never thank these great people enough for being there.

A special acknowledgement goes to my thesis advisor, Dr. Theodore M. Biewer, for his patience and support throughout my thesis work. If not for him none of this would have been possible. His expertise in diagnostics, plasma physics, and scientific research helped guide me through my work. His ability to relate to me on a personal level, acknowledging my tough times and listening to me, was invaluable. I am extremely grateful. I wish to also extend my sincere gratitude to Prof. David C. Donovan, Prof. Maik K. Lang, and Dr. Ezekial A. Unterberg for serving on my thesis committee.

I wish to thank all of those on the Prototype Material Plasma Exposure Experiment team at Oak Ridge National Laboratory. I have had the pleasure to learn so much from everyone involved. I acknowledge the faculty, staff, and students of the Bredesen Center for Interdisciplinary Research for giving me the opportunity to pursue a Doctorate in science research and for supporting me. A thank you goes to Prof. Oliver Schmitz of the University of Wisconsin-Madison and Dr. Jorge Munoz Burgos for working closely with me on my research, offering opportunities to better my research, and being available for my many questions.

Abstract

The helium-line Optical Spectroscopy (HELIOS) diagnostic measures T_e and n_e using a collisional radiative model (CRM) to interpret the relative intensity of neutral helium emission lines in the presence of plasma. The emission intensity can be measured at a data digitization rate of up to 1 MHz with a Filtered radiometer. A HELIOS system was installed and tested on the Prototype Material Plasma Exposure eXperiment (Proto-MPEX), which is a precursor to the planned MPEX facility at Oak Ridge National Laboratory (ORNL). The open magnetic geometry of Proto-MPEX is ideal for testing and characterizing diagnostics. Validation studies were performed in a deuterium plasma and compared HELIOS measurements of T_e and n_e to Thomson Scattering (TS) measurements and edge Double Langmuir Probe (DLP) data. It was found that the helium line emission measured by HELIOS was localized to the plasma edge. The high plasma density ($> 2.0 \times 10^{12}\ cm^{-3}$) of the discharge core was preventing the neutral helium gas puff from penetrating past the plasma edge. In order to penetrate to the plasma core, the gas puff pressure was increased, which resulted in an increased ambient neutral pressure in the chamber. The increased neutral density in the plasma chamber caused radiation trapping of the singlet transition helium lines ($3^1S \rightarrow 2^1P$ and $3^1D \rightarrow 2^1P$). To account for radiation trapping, the ORNL CRM was modified using the optical emission factor (OEF) method. The HELIOS core data for the increased gas puff experiment was re-analyzed using the new ORNL OEF CRM ($T_e \approx 3.4\ eV$; $n_e \approx 7.80 \times 10^{12}\ cm^{-3}$) and compared to DLP data collected on axis at the plasma core ($T_e \approx 2.8\ eV$; $n_e \approx 1.90 \times 10^{13}\ cm^{-3}$). While the n_e measurements from HELIOS are somewhat low compared to the DLP data, the measurements are still within range of the estimated systematic errors. The inferred T_e values from the ORNL OEF CRM are consistent with the DLP data, supporting the conclusion that radiation trapping is an important consideration and needs to be included in the CRM for accurate HELIOS measurements of n_e and T_e.

Table of Contents

List of Tables

List of Figures

List of Abbreviations

Atomic Data Analysis System [ADAS]
Axially Symmetric Divertor Experiment upgrade [ASDEX-U]
Beam Emission Spectroscopy [BES]
Central Chamber side mounted gas puffer [6.5S]
Central Chamber top mounted gas puffer [6.5T]
Charged Coupled Device [CCD]
Collisional Radiative Model [CRM]
Conflat Flange [CF]
Current-Voltage [I-V]
Demonstration power plant [DEMO]
Deuterium [D or ^{2}H]
Double Langmuir Probes [DLP]
Edge Localized Modes [ELMs]
Electron Bernstein Wave [EBW]
Electron Cyclotron Heating [ECH]
Electron Energy Distribution Function [EEDF]
fast Visible Camera [fVC]
Full Width Half Maximum [FWHM]
Fusion Power Plant [FPP]
Gas Penetration Experiment [GPE]
HElium Line-ratIO Spectral-monitoring[HELIOS]
High Confinement Mode [H-mode]
High Flux Isotope Reactor [HFIR]
Hot hELicon eXperiment [HELIX]
Hybrid Time Dependent/Independent [HTD/I]
Infrared Cameras [IRC]
Ion Cyclotron Heating [ICH]
Korea Superconducting Tokamak Advanced Research [KSTAT]
Last Closed Flux Surface [LCFS]
Limiting Flux Surface [LFS]
Low Confinement Mode [L-mode]
Magnetically Confined Fusion [MCF]
Magnetohydrodynamics [MHD]
Material Plasma Exposure Experiment [MPEX]
Multipoint Thomson Scattering [MPTS]
NAGoya Divertor Simulator – I [NAGDIS-I]
Oak Ridge National Laboratory [ORNL]
Ocean Optics [OO]
Optical emission factor [OEF]
Optical emission spectroscopy [OES]
Photomultiplier Tube [PMT]
Plasma facing components [PFC]
Plasma Material Interaction [PMI]
Prototype Material Plasma Exposure Experiment [Proto-MPEX]

Scrape-Off-Layer [SOL]
Thomson Scattering [TS]
titanium, zirconium, molybdenum [TZM]
Tokamak Experiment for Technology Oriented Research [TEXTOR]
Tritium [T or ^3H]
Tungsten Environment in Steady State Tokamak [WEST]
University of Wisconsin – Madison [UW-M]
Virtual instrument [vi]
Wendelstein 7-X [W7-X]

List of Symbols

A	Aspect ratio	
A_{OEF}	Einstein Coefficient of Spontaneous Transitions after radiation trapping is accounted for	[s^{-1}]
$A_{i\rightarrow j}$	Einstein Coefficient of Spontaneous Transition	[s^{-1}]
B_{filter}	Spectrum measured by the McPherson as light passed through the one-inch filters	[Counts]
B_{filter_back}	Background measured by the McPherson spectrometer for the one-inch filters	[Counts]
$B_{McPherson}$	Spectrum measured by the McPherson as light passed through the fibers without the one-inch filters	[Counts]
B_{MCP_back}	Background measured by the McPherson fibers without the one-inch filters	[Counts]
$\mathbb{C}$	Conductance of viscous flow regime	[cm^3/s]
$\mathbb{C}_{UW-M}$	Conductance of the UW-M gas injection system	[cm^3/s]
$\mathbb{C}_{PV-10}$	Conductance of the PV-10 gas injection system	[cm^3/s]
$\mathbb{C}(A,L)$	Conductance thin hole approximation	[cm^3/s]
C	Capacitance	μF
$\boldsymbol{C}$	Generalized Collisional Radiative Matrix	[s^{-1}]
$CX_{P_I}/CX_{P_{I'}}$	Charge exchange or charge exchange recombination	[cm^3/s]
c	Speed of light	[cm/s]
c_s	Sound speed	[cm/s]
D_α	Deuterium alpha Balmer line	
D_p	Diameter of pipe/nozzle	[cm]
D_v	Diameter of the valve on the gas puffers	[cm]
$D_{v,trans}$	Critical diameter of the gas puffer valve	[cm]
d_{gas}	Depth of the gas puff	[cm]
E	Energy	[J]
ΔE	Difference in energy	[J]
Ei(-x)	Exponential integral	
e	Electron charge	[C]
$F_{i\rightarrow j}/F_{j\rightarrow i}$	Excitation/De-Excitation rate coefficient	[cm^3/s]
$f(E)$	Electron energy distribution function	[eV]
$f_{i\rightarrow j}$	Oscillator strength	[s^{-1}]
f_θ	Scattering amplitude	
$\frac{G_{Cal}}{G_{PMT}}$	Calibration gain coefficient ratio	
g_0	Optical escape factor	
g_i	Degeneracy of state i	
I/I_{out}	Current	[A]
I^a/I^b	Intensities involved in the ratios dependent on T_e and n_e for HELIOS	[Photons/s]
$I_{667.90}$	Intensity of 667.90 nm line	[Photons/s]

$I_{706.53}$	Intensity of 706.53 nm line	[Photons/s]
$I_{728.00}$	Intensity of 728.00 nm line	[Photons/s]
$K(A,L)$	Transmission probability for the thin hole conductance approximation	
Kn	Knudsen number	
k_B	Boltzmann Constant	[m^2kg/s^2K]
k_o	Absorption coefficient	[cm^{-1}]
L_p	Length of pipe/nozzle	[cm]
M	Mach number	
m_e	Mass of electron	[kg]
m_{He}	Mass of helium	[kg]
N_A	Avogadro's Number	[particles/mol]
n^+	Number density of helium atoms in the first ionized state	[cm^{-3}]
n_0	Number density of helium atoms in the ground stat	[cm^{-3}]
n_{He}	Neutral helium in the system	[cm^{-3}]
$n_{He\ Injected}$	Density of helium gas injected into the plasma column	[cm^{-3}]
$n_{He\ wall}$	Neutral density of helium at the wall	[cm^{-3}]
$n_{He\ Plasma}$	Neutral helium in the plasma	[cm^{-3}]
n_I	Hydrogenic ion density	[cm^{-3}]
$n_I^{+z}/n_{I'}^{z'}$	Arbitrary ion densities that may remove or add a charge exchange electron from n_p	[cm^{-3}]
n_p	Population Density of the pth term	[cm^{-3}]
n_q	Population Density of the qth term	[cm^{-3}]
P	Pressure in the gas puffer plenum	[mbar]
R	Radius between center of the plasma and the collection optics	[cm]
$\boldsymbol{R}$	Ideal gas constant	[J/Kmol]
Re	Reynolds number	
R_{n_e}	Density dependent ratio	
R_{T_e}	Temperature dependent ratio	
$RC_{p,q}$	Rate coefficient	[a.u.]
$\mathcal{R}$	Responsivity of the Filterscope system	[Photons/s cm^2]
r_{shell}	Hard shell radius of a gas particle	[pm]
r_P	Plasma radius	[cm]
S_i	Ionization rate coefficient	[cm^3/s]
T	Temperature	[K]
$T_{\frac{1}{100}}$	Fractional transmission of the one-inch bandpass filters	
T_e	Electron Temperature	[eV]
T_{He}/T_g	Temperature of the gas	[K]
T_i	Ion Temperature	[eV]
$T_{McPherson}$	Filter transmission measured by the McPherson	[%]
t	Time	[ms]

Δt	Time response of the piezo crystal	[ms]
$\dot{V}$	Volumetric flow rate	[cm^3/s]
V_{PV-10}	Volume of the PV-10 nozzle	[cm^3]
V_{UW-M}	Volume of the UW-M nozzle	[cm^3]
V_{cont}	Control bias on the photomultiplier tubes	[V]
V_{PMT}	Voltage recorded by a specific PMT during operations	[V]
ΔV	Change in voltage supplied to piezo crystal	[V]
υ_e	Free electron velocity	[cm/s]
$\upsilon/\, \upsilon_{th}/\, \upsilon_{He}$	Velocity of helium gas	[cm/s]
χ_i	Ionization potential	
x	Position	[mm]
Δx	Displacement of viton plate	[mm]
z	Next ionization stage	
α_p	Three-body recombination rate coefficient	[cm^6/s]
β_p	Radiative recombination rate coefficient	[cm^3/s]
ε_λ	Line emission of a specific wavelength	[Photons/s cm^3]
ϵ_0	Permittivity of a vaccum	[A s/V m]
γ_p	Di-electronic recombination rate coefficient	[cm^3/s]
λ	Wavelength	[Å]
$\Delta\nu$	Full Width Half Max	
$\Omega_{j,i}$	Collisional strength of transition j, i	
Φ_λ	Photon flux for a specific wavelength	[Photons/s cm^2]
$\sigma_{A_{i,j}}/\sigma_{A_{i,k}}$	Error in the Einstein coefficients of spontaneous emission for the transitions invoked in the ratios dependent on T_e and n_e for HELIOS	[s^{-1}]
σ_a/σ_b	Error in the intensities involved in the ratios dependent on T_e and n_e for HELIOS	[Photon/s]
σ_{n_e}	Error in the electron density	[cm^{-3}]
$\sigma_{p,q}$	Cross sections	[cm^2]
σ_R	Error in the experimentally measured and model calculated ratios dependent on T_e and n_e for HELIOS	
σ_R^{EXP}	Error in the experimentally measured ratios dependent on T_e and n_e for HELIOS	
σ_R^{MOD}	Error in the model calculated ratios dependent on T_e and n_e for HELIOS	
σ_{T_e}	Error in the electron Temperature	[eV]
$\Upsilon_{j,i}$	Effective collisional strength of transition j, i	
$\zeta_{McPherson}$	Normalized bandpass of the one-inch filters measured by the McPherson spectrometer	

Chapter 1 Introduction

1.1 Executive Summary

A HElium Line-ratIO Spectral-monitoring (HELIOS)[1] diagnostic was tested on the Prototype Material Plasma Exposure eXperiment (Proto-MPEX)[2] to obtain novel measurements of electron temperature (T_e) and density (n_e) on a high-density, low temperature linear plasma device. Linear devices are ideal for plasma material interaction (PMI) studies and are key to bridging the gap between current fusion technology and future fusion power producing devices. Diagnostics that measure T_e and n_e are important for understanding the plasma physics and PMI of these and future devices. HELIOS using a Filterscope[3] radiometer offers high time resolution (100 kHz to 1 MHz) measurements of T_e and n_e, which is able to resolve important temporal phenomena in plasmas, like turbulence.

The ambient neutral pressure in Proto-MPEX was determined to be a significant factor in HELIOS measurements of T_e and n_e. Background neutral pressures and hence neutral densities of helium ($> 3.00 \times 10^{12}\ cm^{-3}$), caused radiation trapping of the singlet line transitions ($3^1D \rightarrow 2^1P$ and $3^1S \rightarrow 2^1P$) to occur between the plasma and the collection optics. This required that the Oak Ridge National Laboratory (ORNL) collisional radiative model (CRM) be modified to support radiation trapping atomic physics. The optical escape factor (OEF) method was used to account for the radiation trapping in the CRM.

The OEF ORNL CRM was tested when the background neutral pressure in the vacuum vessel of Proto-MPEX was increased in an effort to achieve He penetration to the core of a D plasma. Validation experiments concluded that the helium emission from the gas puff was localized to the plasma edge. The high electron density of the deuterium plasma in Proto-MPEX ($> 2 \times 10^{-13}\ cm^{-3}$) was deterring the gas puff from penetrating into the plasma core and localizing the helium line emission to the plasma edge. An increase in the throughput of the gas puff allowed for the He I particles to reach the plasma core, increasing the neutral pressure in the vacuum chamber. Analysis of the gas puff penetration data with the ORNL CRM yielded inconsistent values between Double Langmuir Probes (DLP) measurements and HELIOS measurements. Re-analysis of the experimental data, using the OEF ORNL CRM, concluded that radiation trapping is a critical inclusion to the atomic physics to accurately measure T_e and n_e.

1.2 Background

Fusion is how our sun and other stars produce energy and is the ‘fusing’ of two atoms.. Typical isotopes used in the production of a fusion reaction on Earth or in Magnetically Confined Fusion (MCF) device are tritium [T or ^{3}H], a product used in fission enrichment facilities and dry cask storage, and deuterium [D or ^{2}H]. The resulting by-products from a fusion reaction, utilizing the aforementioned isotopes, is the non-radioactive isotope ^{4}He and a high energy neutron. Experimental MCF reactors, such as tokamaks and stellerators, use the ^{2}H—^{2}H reactions because of its low yield of neutrons and the fact that ^{3}H is export controlled and requires licensing and safeguards for a single campaign. The ^{2}H—^{3}H reaction will be used in near term fusion reactor prototypes.

In contrast, nuclear fission is the splitting of a heavy atom, typically with more neutrons than protons, into lighter isotopes, or fission products, high energy neutrons, and energy. This process results when the heavy atom collides with high speed particles, commonly a neutron. Traditional fission reactions such as that found in light water (LW) and boiling water (BW) reactors use Uranium-235 (^{235}U). ^{235}U fuel rods are inserted into a moderator, commonly water, where the released neutrons in the fission reaction start the nuclear chain reaction. The nuclear chain reaction heats the water into steam, which is how a fission reactor continues to produce energy. The isotopes that result from a ^{235}U fission reaction (Iodine-131, Cesium-137, and Strontium-90 to name a few) can have long half-lives (Cesium-137 has a half-life of ~30 years) and health related issues (Iodine-131 is related to thyroid diseases and cancers). The long half-life of fission byproducts has created a nuclear waste storage crisis and has lent to the drive, in today’s climate, of moving away from large MW nuclear fission reactors.

Both fusion and fission energy focus on utilizing the power of the atom. Fusion is considered an advanced nuclear reactor type. There are many advanced nuclear reactor concepts in research and development (small modular reactors, molten salt, etc.) with the goal of overcoming future energy hurdles and help society move away from large MW reactors, which are no longer economically and environmentally sound. Fusion offers competitive benefits as an advanced reactor option. For example, fusion does not release the long-lived radioactive waste products that a traditional fission reaction does and utilizes isotopes of hydrogen which are the most common element found in the universe.

An effort has been ongoing for about 60 years to make use of this vast fusion energy source on Earth, resulting in MCF devices being built across the world to research and develop fusion energy. MCF devices are large structures made of steel and magnets to contain plasmas, the fourth state of matter, at temperatures on the order of $1.0 \times 10^{8}\ K$. The circular shaped magnets are used to confine the plasma to the center of the machines away from the wall or plasma facing components [PFC]. Future fusion devices will optimistically be designed to produce greater than ten times the power than is injected for operation, leading to a burning plasma that will sustain itself. The understanding of this plasma physics and the materials around it are necessary to utilize the vast amount of energy produced from nuclear fusion. Figure 1.1 is an image of the General Atomics tokamak DIII-D taken by Jon Kinsey[4] and Figure 1.2 is an image of a tokamak's magnetic components.[5]

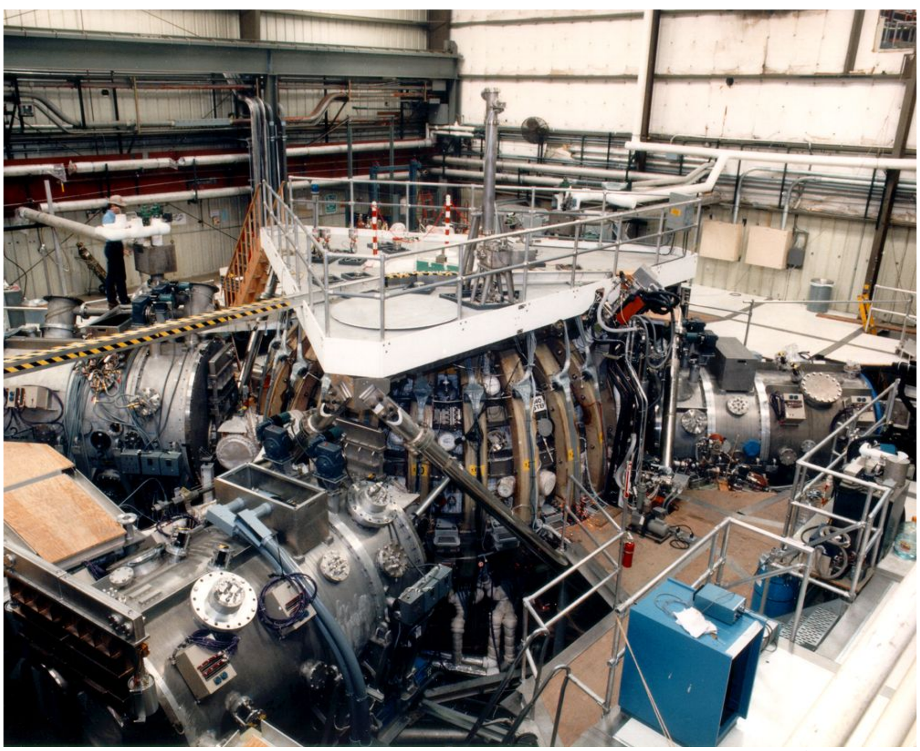

Figure 1.1. The tokamak DIII-D at general atomics[4].

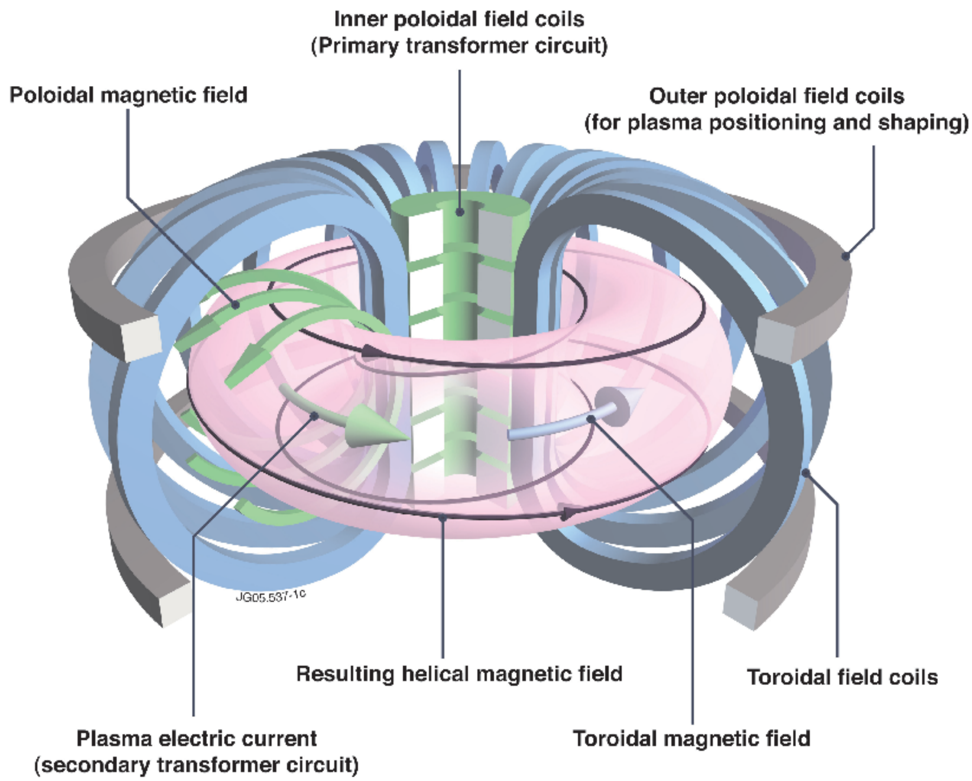

Figure 1.2. Image of the magnetic make-up of a tokamak.[5]

Plasma physics is the fundamental science behind fusion energy and involves the measurement and interpretation of particle temperatures and densities, bulk potential, velocities, movement, and forces to evaluate the changes in plasma conditions. For example, edge localized modes [ELM] and turbulence in the plasma edge that result in damages to PFCs can be studied by monitoring the plasma electron temperatures. There is a large suite of diagnostics used in plasma physics to address the hurdles that fusion faces, but this thesis only focuses on the measurement of electron temperature [T_e] and density [n_e]. Electron temperature and density are important measurements to be made in order to understand transport, disruptions, turbulence, and particle flux. Well known T_e and n_e diagnostics include the double Langmuir probe [DLP], Thomson Scattering [TS], and the helium line ratio technique we have termed HELIOS. The HELIOS technique has been used to measure T_e and n_e in fusion devices across the world (detailed in section 1.5) and will be the focus of this study.[6,1,7,8,9] HELIOS has progressed over the years as a diagnostic both in hardware application and atomic data. This fact motivated an interest in using HELIOS on the linear plasma device Proto-MPEX. Proto-MPEX has a suit of diagnostics. Including a radiometer known as the Filterscope[3,10] and a (McPherson) Czerny Turner 1-meter spectrometer. Each of the spectroscopic instruments can measure light from the plasma utilizingtwenty-four collection optics at the plasma, with a 12 cm resolution of the plasma radius. The Filterscope and McPherson are used to measure the optical emission of the three separate He I lines [$I_{667.9}$, $I_{706.53}$, and $I_{728.0}$]. Ratios are calculated from the data and T_e and n_e measurements are infereed from a CRM. By using the Filterscope (100 kHz Proto-MPEX digitization rate) to perform HELIOS, temporally resolved T_e and n_e measurements can be made and compared to TS (10 Hz) and DLPs (200 Hz). The McPherson measurements (20 – 40 Hz typically) are a spectrally resolved signal for comparison. The two instruments, Filterscope and McPherson, are both used to validate the CRM in HELIOS on Proto-MPEX.

HELIOS as a spectroscopic diagnostic offers noticeable advantages for devices such as Proto-MPEX and tokamaks. In a linear plasma device, port allocation and alignment can be difficult for a diagnostic such as TS, and the high-power input from the radiofrequency (200 kW) and microwave (50 kW- 100 kW) systems tend to damage Langmuir probes. Furthermore, HELIOS has the potential of being used near the helicon source. This can be used in transport and power modelling to properly represent the helicon source region. Probes in a linear device can hinder the plasma propagation, ultimately altering the plasma downstream, and if the helicon source alters the electron energy distribution function (EEDF)[8] then any diagnostic that makes a Maxwellian assumption will be inaccurate. This is also the case for other power sources such as microwaves. An alternative diagnostic technique to the DLP and TS to measure T_e and n_e, such as the HELIOS diagnostic, can potentially overcome these hurdles and offer great diagnostic support for PMI studies. In a tokamak, especially a power producing device that utilizes the D-T reaction, HELIOS can potentially utilize the edge exhaust helium to measure T_e and n_e.[11,12]. The modelling application of this potential use of HELIOS is explored in Chapter 6 of this work. HELIOS utilizing the Filterscope is the fastest T_e and n_e diagnostic on Proto-MPEX and has the potential of being used on fusion devices such as tokamaks and stellerators for edge turbulence monitoring. Also, while HELIOS is based on helium line ratios the CRM is used for many atomic species and applications, meaning that understanding the atomic model is very significant to the fusion community. The information used in and obtained from using a CRM is used in transport modelling,[13,14] spectroscopic measurements of neutral density from Balmer lines,[15] and tungsten PMI research.[16,17]

In the following sections of this chapter these statements will be expanded upon in the motivation section. A description of HELIOS and how the CRM works will be detailed, followed by a section on experiments performed on other devices. The final section will outline the remaining chapters of the thesis.

.

1.3 Motivation

Ideally, HELIOS as a mostly passive diagnostic allows for T_e and n_e to be measured with little to no perturbation to the background plasma. Moreover, the diagnostic itself is unperturbed by the plasma column. DLPs, which are two long insulated (except for the tips) biased wires, must be inserted into the plasma edge or column to measure the electron current with respect to the plasma potential.[18] LP theory allows for the determination of the electron temperature and density of a plasma by "sweeping" the bias voltage of the probe from negative to positive values.[19] Figure 1.3 shows a generalized current-voltage (I-V) trace where the voltage has been swept from a negative region (left) to a positive region (right) with respect to the plasma potential.[19,19] LPs and DLPs have provided most of the information regarding the scape off layer [SOL] region of the plasma at relatively low temperatures, $T_e \leq 100$ eV, due to their simple structure and inexpensive application into a plasma device.[20]

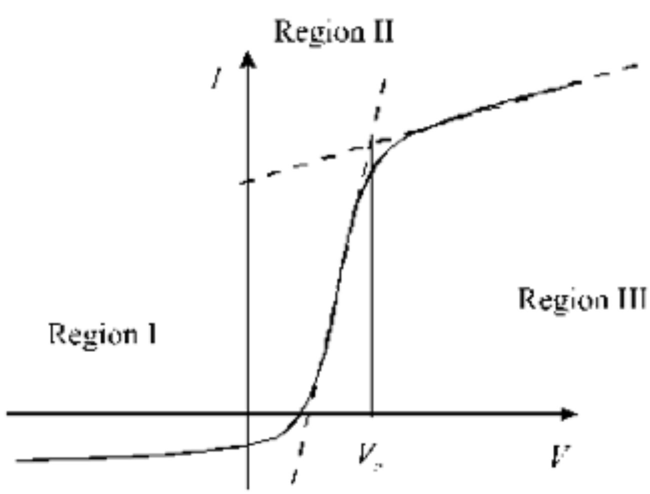

Figure 1.3. DLP I-V Trace.[19]

Probes may be the easiest diagnostic to implement and have provided the fusion community with a plethora of information regarding plasma edge physics, but they are not without their problems. Since DLPs are directly inserted into the plasma they perturb the plasma and make the diagnostic vulnerable to damage that could release impurities into the plasma edge. Figure 1.4 is two images demonstrating how a probe can be damaged inside of a fusion relevant device. The left-hand image is a helicon only (< 100 kW) plasma and the probe is the dark spot at the right edge of the image near the center. The probe is roughly 2 cm away from the plasma core. In the right-hand image the probe is damaged when the Electron Cyclotron Heating (ECH) microwave system is turned on. The burst of white and purple light erupting from the probe is a large arc that caused the probe tips to weld together and pieces of the ceramic to fly off. Furthermore, the helicon power in Figure 1.4 is less than 100 kW, so as the helicon power is increased (~200 kW) the probes will be damaged in the helicon only plasma, too, not just with the auxiliary power supplies active. HELIOS would be able to overcome this hurdle due to its passive nature to the plasma column.

Figure 1.4. Helicon only plasma with DLP inserted (left) and the destruction of the DLP during microwave injection (right).

TS is an alternative to DLPs and would not suffer from the issue stated in the previous paragraph. TS is the elastic scattering of a photon off of a free plasma electron, which is demonstrated by the drawing in Figure 1.5. By measuring the wavelength of the scattered photon the velocity of the free electron, v_e, can be determined.[21,22] The scattering of electromagnetic radiation as a plasma diagnostic is non-perturbing to the plasma and offers more detailed information regarding the electron distribution function.[22,23] The application of TS (Figure 1.5) involves a coherent beam of light (laser of wavelength λ_0) directed through a plasma, allowing for the individual photons to "Thomson scatter" off of the individual plasma electrons to produce a spectrum of scattered light with a distribution of wavelengths, $\lambda_0 + \Delta\lambda$. The shape of the produced spectrum represents the electron velocity distribution function, allowing for the electron temperature of the plasma to then be calculated.[21]

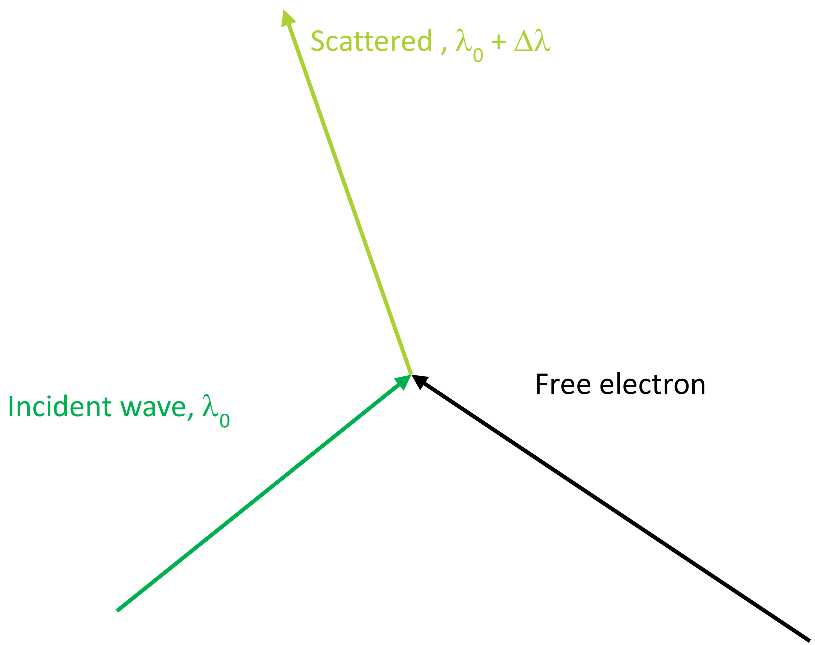

Figure 1.5. Cartoon diagram of the Thomson scattering of light from a plasma free electron.

Whereas, TS is an excellent form of T_e and n_e measurements, the measurements are compromised when there is too much stray light,[23] or the density is too low. Also, TS requires lasers of a specific wavelength and high energy, meaning that TS systems can be extremely expensive due to laser installation, training, and maintenance. Furthermore, the application of TS on plasma devices can be difficult because of access requirements. For example, the laser must pass directly through the plasma and into a laser dump, so the geometry and path of the diagnostic and laser is very specific. Also, the laser alignment takes time and careful consideration because not only does the laser have to pass through the plasma into a dump, but the optics must be aligned to the thin laser axis to measure the wavelength of the scattered light.

HELIOS is in no danger of being damaged by the plasma conditions, can be little to non-perturbative, is less expensive than a TS system, may be more easily installed than TS, can have up to 1 MHz digitization rates, and is simple to align. This makes HELIOS, as compared to DLP and TS, a great alternative diagnostic to measure T_e and n_e.

Over the years plasma physics has gradually progressed toward a commercial power producing fusion reactor. However, there are still hurdles to overcome and many of these issues lie in the edge plasma of an experimental fusion reactor. The edge plasma is the boundary layer between the plasma core and the PFCs. Edge plasmas have considerably lower T_e and n_e than the plasma core, creating a density and temperature gradient that can have direct effects on the plasma stability. Transport processes in the plasma edge can directly affect the core stability and the core-edge transport process like heat and particle fluxes. [24] One such transport process is turbulence which are not fully understood and can cause damage to the PFCs if violent enough. Turbulence in the plasma edge is a field of study that has progressed significantly over the years through modelling and edge diagnostics. Turbulence can induce particle flux to the PFCs and is relevant in understanding cross-field transport. [25] Cross-field transport of particles is the movement of particles from the core plasma past the last-closed-flux surface [LCFS] or "separatrix" into the scape-off-layer [SOL]. Figure 1.6 is a cross-section of the General Atomics tokamak, DIII-D, demonstrating each of these boundaries. [26]

Edge turbulence has a typical frequency range between 10 kHz and 1 MHz and can be monitored by the fluctuations in T_e and n_e. Edge turbulence studies are usually performed by using edge diagnostics: 2D probe arrays, [27,28] 2D beam emission, [29] and gas puff imaging. [30] Early designs of the 2D probe contained a square array of 64 probes arranged in a 3.24 cm^2 area.[27] Current designs have significantly improved. These new designs are called fast reciprocating probes that are designed to enter the SOL of the plasma and retract within a 0.2 second period. [31,32] These multi-point probes have several tips that are designed to simultaneously measure plasma potential, n_e, and T_e.

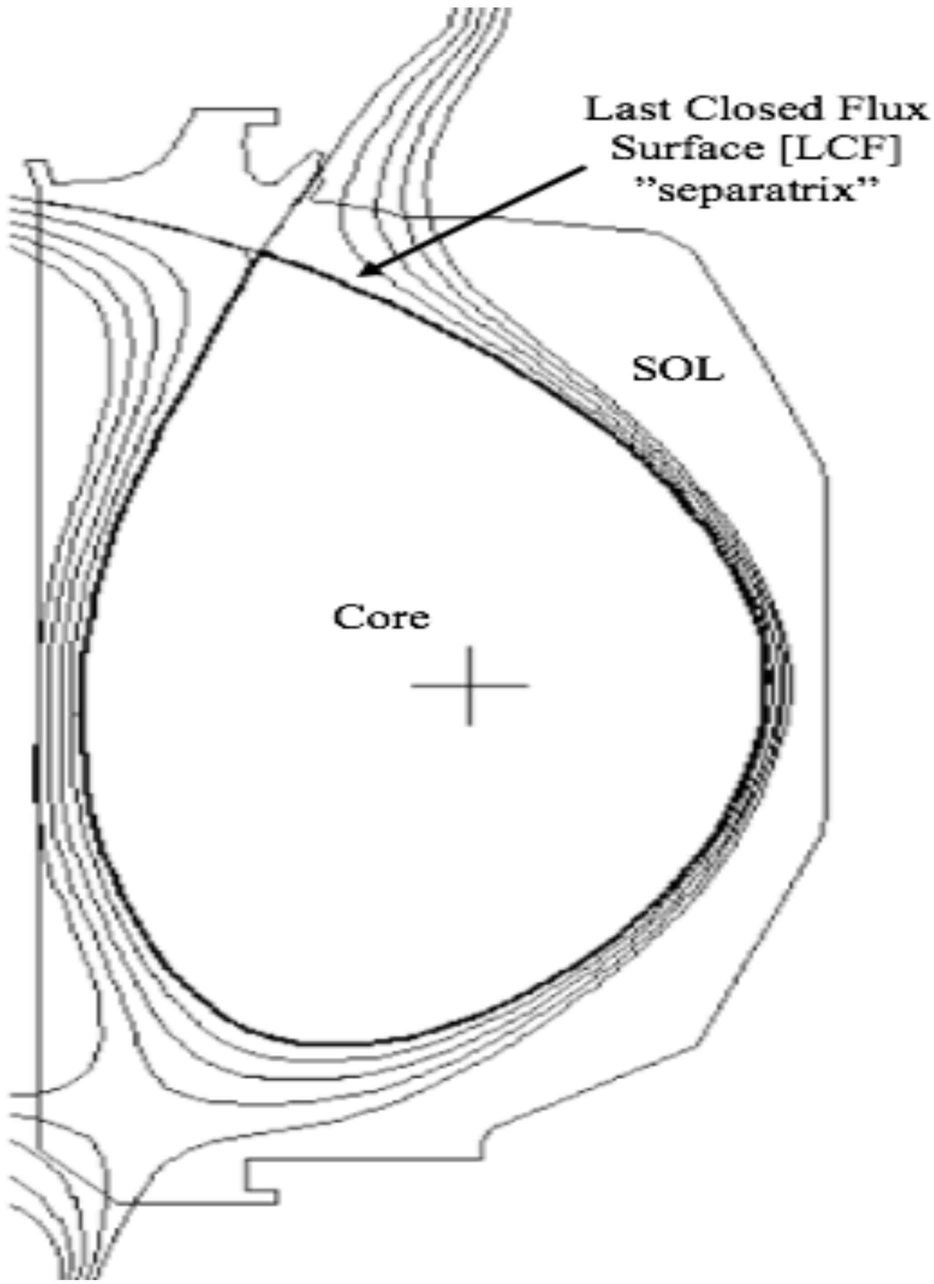

Figure 1.6. Cross-section of a tokamak.

The harmonic technique, a probe drive with high-frequency sinusoidal voltage is used to generate harmonics in the current spectrum, is employed to measure T_e at sampling rates of 5 MHz for the 0.2 seconds that the probe is inserted into the plasma, making this diagnostic significant for measuring T_e fluctuations in the plasma edge.[31-33] 2D beam emission and gas puff imaging have been employed to spatially resolve the dense turbulent structures, “blobs”, in the plasma edge as shown in left-hand image of Figure 1.7.

The chord measured HELIOS diagnostic proposed in this thesis has a sampling rate of 100 kHz (up to 1 MHz) and can employ several chord measurements, increasing the spatial resolution. As an optical emission spectroscopy (OES) diagnostic, the HELIOS measurement duration is only limited by the length of the He gas puff requested. ELMs, which are shown in the right-hand image in Figure 1.7 are magnetohydrodynamic (MHD) instabilities that occur in high confinement, or “H-mode,” plasmas.

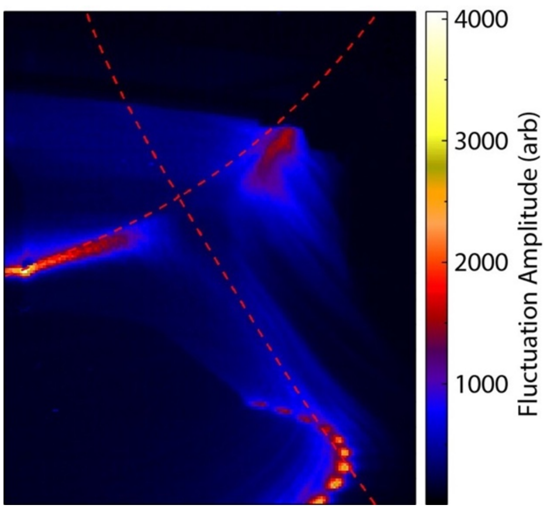

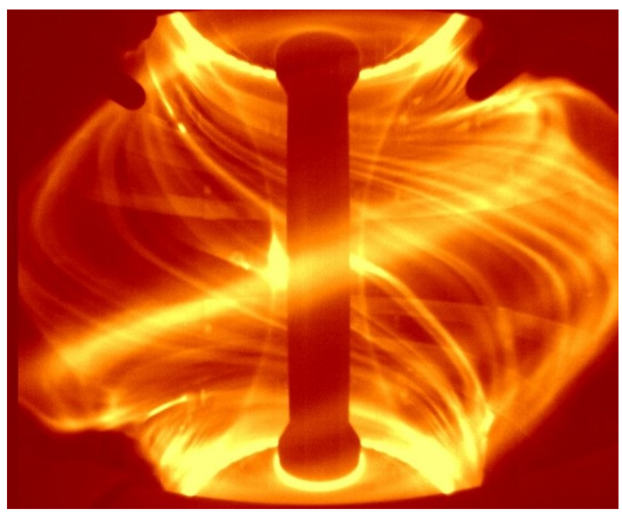

Figure 1.7. Visual representations of the dense turbulent structure known as a “blobs” (left)[34] and the beginning of an ELM (right) in the Mega Amp Spherical Tokamak [MAST].[35]

An ELM exposes the PFC to a burst of increased heat load and particle flux, putting the material in danger of being damaged. When an ELM occurs, there is a rapid decrease in the electron temperature within the LCFS.[36] This rapid transport heats the SOL outside of the LCFS, suggesting that ELMs can be monitored by measuring the electron temperature of the edge plasma in a tokamak.[36,37] Simple LPs usually cannot survive the heat flux of an ELM and even though TS has made improvements in multi-point Thomson Scattering [MPTS][38,39] it can only measure along the line of the laser and is an extremely expensive diagnostic.

Turbulence and ELMS pose a danger to the PFCs. The interaction between the plasma and the PFC is its own field of study known as PMI studies. Understanding the interaction between the plasma and the PFCs must be understood before fusion power plants can be built. The development of fusion energy has been for a long time a plasma confinement issue. However, in recent years, due to progression in the fusion community, the development of fusion energy has also become a materials and engineering issue. The PFCs are the inner wall materials directly adjacent to the plasma either in a tokamak, stellarator, or linear device. The PFCs are exposed to extremely harsh conditions inside of a fusion device during operations. For example, the ITER divertor region will be exposed to high heat fluxes ($\sim 10\ \frac{MW}{m^2}$)[40] and sometimes damaging plasma transients ($50\ \frac{MW}{m^2} - 100\ \frac{MW}{m^2}$)[41] from ELMs or turbulent phenomena. ITER, being built in the south of France, is a large experimental fusion device that is designed to maintain fusion for ~500 seconds and plasma pulses for ~3000 seconds, exposing the PFC to long periods of harsh fusion conditions .[40] Furthermore, fusion devices such as the DEMOnstration power station (DEMO) or the Fusion Pilot Plant (FPP), which is set to be built for net electricity production, will need PFCs that can withstand years of harsh treatment. Therefore, PMI studies are vital for the future of fusion energy. To properly perform PMI studies an understanding of the plasma interacting with the material is necessary.

The CRM and OES are essential for understanding PMI studies. Helium line ratios are the main focus of this thesis, but the CRM can be used for other atomic species such as W.[17,16] Continued work on, and improvement to the CRM is invaluable to the fusion community and ensures that spectroscopic diagnostics are up to date and working properly for PMI research. Furthermore, these spectroscopic techniques and CRM can be used for transport modelling of particles in the plasma, including W, and neutral density measurements in the plasma core and edge, using hydrogen.

The fundamental plasma parameters, T_e and n_e, can be used to monitor turbulence and ELMs and understand PMI physics in toroidal fusion devices. Even though linear machines do not typically produce turbulence and ELM phenomena, PMI studies are very relevant in these devices. The Prototype Material Plasma Exposure eXperiment [Proto-MPEX] produces low temperature ($T_e < 10\ eV$), high density ($n_e > 2 \times 10^{13}\ cm^{-3}$) plasmas, which are similar to the divertor conditions found in large fusion devices. Proto-MPEX has an open field line geometry unlike toroidal machines (Figure 5.12). The open geometry of Proto-MPEX allows for a multi-chord HELIOS diagnostic to produce superior spatially and temporally resolved measurements of T_e and n_e as a function of magnetic field near the target's surface. This fact makes the Proto-MPEX linear device an excellent candidate for fusion relevant PMI research.

1.4 Optical Emission Spectroscopy and HELIOS

The HELIOS diagnostic, similar to other diagnostics, has both a theory/modelling part and a hardware part. Experimentally it involves a gas injection system and an optical emission spectrometer that will be discussed in detail in Chapter 3 and 4. The experimental setup is used to measure the helium line intensities $I_{667.9}$, $I_{706.53}$, and $I_{728.0}$ in the plasma during a set puff length of helium gas. The measured intensities are used to calculate the T_e dependent ratio, $R_{T_e} = \frac{I_{706.53}}{I_{728.0}}$, and n_e dependent ratio, $R_{n_e} = \frac{I_{667.9}}{I_{728.0}}$. The ratios are then used to derive T_e and n_e of the plasma region from a CRM. This section of Chapter 1 will explain the theory behind the CRM.

The CRM is used to calculate the same helium intensities measured experimentally by solving Equation 1.2.1 for each wavelength, λ.

$$I_\lambda = A_{p \to q} \frac{dn_p}{dt} n_e \qquad \textit{Equation}\ 1.2.1$$

$A_{p \to q}$ is the known spontaneous transmission coefficient from state *p* to state *q*, or the Einstein coefficient of spontaneous emission, and $\frac{dn_p}{dt}$ is the rate of change of the population density of the upper state *p*. Electrons transition between quantum states (e.g. *p* and *q*) in an ion or atom through radiative and collisional processes.[42,43] Therefore, if $\frac{dn_p}{dt}$ is the rate of change of population density of state *p* (rate of change of the number of electrons in state *p*) then $\frac{dn_p}{dt}$ can be explained through a series of radiative and collisional processes. Solving for $\frac{dn_p}{dt}$ is the most computationally demanding part of the CRM, and hence the HELIOS diagnostic and can be represented by Equation 1.2.2.[44] The importance of 'can be represented by' depends on the plasma parameters being measured. For example, an experimentalist measuring T_e in the edge plasma of a tokamak where temperatures are usually greater than 100 eV would not be as concerned about recombination as an experimentalist measuring much lower temperature plasmas (< 2 eV). This is due to the recombination transition's inverse dependence on electron temperature. However, a quantitative understanding of the transitions included in the population density equation must be done, using the plasma of interests T_e and n_e, to understand the significant transitions.

$$\frac{dn_p}{dt} = -n_p\left[n_I^{+z}CX_{p,I} + n_eS_p^e + n_IS_p^I + \sum_{q\neq p}\left(n_eF_{p\to q}^e + n_IF_{p\to q}^I + A_{p\to q}\right)\right] + n_q\left[\sum_{q\neq p}\left(A_{q\to p} + n_eF_{q\to p}^e + n_IF_{q\to p}^I\right)\right] + n^+\left[n_{I'}^{z'}CX_{p_{I'}} + n_e\beta_p + n_e\gamma_p + n_e^2\alpha_p\right] \qquad \text{Equation 1.2.2}$$

Here p is the state of interest and q is any state above or below state p. The summations for "$q\neq p$" is the sum of all states energetically lower and energetically higher than state p respectively. The density terms $n_p, n_q, n_I, n_e, n^+, n_I^{+z}$ *and* $n_{I'}^{z'}$ are the population of the p^th term, the population of the q^th term, the hydrogenic ion density, the electron density, He^+ density, and the final two terms are arbitrary ion densities that may remove or add a charge exchange electron from n_p.[44] The rest of the terms $S, F, CX, \beta, \alpha,$ and γ are called rate coefficients. Each rate coefficient represents a probability of that transition occurring. Table 1.1 describes what each rate coefficient term represents. The $(\pm)$ means that either a positively charged ion or an electron is involved, *p'* and *+'* represent an external atom and ion such as H and H^+, $[\boldsymbol{p}]$ is the autoionization of an atom, and **z** represents a new ionization state.

Rate coefficients are calculated from their respective cross-sections $\sigma_{p,q}$ (i.e. the electron impact excitation would be calculated from the electron excitation cross-section). Cross-sections are considered the fundamental atomic data to determining the population density of a state, having units of area [cm^2], and are calculated quantum mechanically by approximating the scattering amplitude, f_θ.[43,,45] For rate coefficients, the probability of a transition occurring is determined by the cross-section. Whether or not a particle would impact on the cross-sectional area and cause a specific transition is included in the calculation of the population-density of state $\boldsymbol{p}$ by the rate coefficients. Rate coefficients are functions of energy and in most cases where a CRM has been used a Maxwellian distribution has been summed over. Equation 1.2.3 is an expression for the calculation of a rate coefficient.[43]

TABLE 1.1. THE RATE COEFFICIENT TERM, WHAT THE TERM REPRESENTS, AND THE REPRESENTING TRANSITION EQUATION.

RATE COEFFICIENT	REPRESENTING TRANSITION	TRANSITION EQUATION
$\boldsymbol{S_n^{\pm}}$	particle (±) impact ionization for state n	$\boldsymbol{p} + (\pm) \rightarrow (\boldsymbol{z}) + (-) + (-)$
$\boldsymbol{F_{q\rightarrow p}^{\pm}/F_{p\rightarrow q}^{\pm}}$	particle (±) impact excitation/de-excitation	$\boldsymbol{q/p} + (\pm) \rightarrow \boldsymbol{p/q} + (-)$
$\boldsymbol{CX_{p_I}/CX_{p_{I'}}}$	Charge exchange and charge exchange recombination	$(\boldsymbol{p/p'}) + (+'/+) \rightarrow \boldsymbol{p'/p} + (+'/+)$
$\boldsymbol{\beta_p}$	Radiative Recombination	$(\boldsymbol{z}) + (-) \rightarrow \boldsymbol{p} + \boldsymbol{h\nu}$
$\boldsymbol{\alpha_p}$	Three-body Recombination	$(-) + (-) + (\boldsymbol{z}) \rightarrow (-) + \boldsymbol{p}$
$\boldsymbol{\gamma_p}$	Dielectonic Recombination	$(\boldsymbol{z}) + (-) \rightarrow [\boldsymbol{p}] \rightarrow \boldsymbol{p} + \boldsymbol{h\nu}$

$$RC(p,q) = \int_a^b \sigma_{p,q}(E)\upsilon f(E)dE \qquad \textit{Equation } 1.2.3$$

In the above equation RC stands for rate coefficient of state p to q, a and b are the upper and lower bounds of the integration, $\sigma_{p,q}(E)$ is the cross-section as a function of energy, $f(E)$ is the EEDF, and υ is the speed of a beam of electrons. The above expression is a very basic mathematical understanding of a rate coefficient equation, but over the years the atomic and plasma physics community have worked together to create generalized collisional radiative coefficients.[46,47,48] Chapter 6, which delves deeper into the modeling portion of the HELIOS diagnostic, introduces some of the generalized rate coefficients. All of the fundamental data used in this study comes from the open Atomic Data Analysis System [ADAS].[49] Other atomic data repositories are available; however, due to improved approximation of the cross-sections the data used in ADAS is considered best for the intended plasma physics purpose.

Equation 1.2.2 is best thought of as a group of populating terms and a group of de-populating terms, which are illustrated in the helium Grotian Diagram in Figure 1.8. In the diagram the dotted lines are radiative transitions (light blue) and solid lines are collisional transitions (solid black). The information in Figure 1.8 plus the information of equation 1.2.2 better contributes to an understanding of the CRM. The first line of bracketed terms in the above population density equation (1.2.2) are the de-populating terms or the terms that remove an electron from the state of interest, p: charge exchange, ionization, de-excitation by electrons and ions from the $\boldsymbol{p}^{th}$ state, and spontaneous transmission from the $\boldsymbol{p}^{th}$ state. The second row of bracketed terms are the populating terms, i.e. the terms that add electrons to the state of interest, p: spontaneous transmission from the upper $\boldsymbol{q}^{th}$ state and electron and ion excitation terms from the lower $\boldsymbol{q}^{th}$ state. The last set of bracketed terms in the third line are recombination terms: charge exchange recombination, radiative recombination, three-body recombination, and dielectronic recombination. Dielectronic recombination will be ignored here due to it being significant only for high temperature plasmas such as the solar corona.[50]

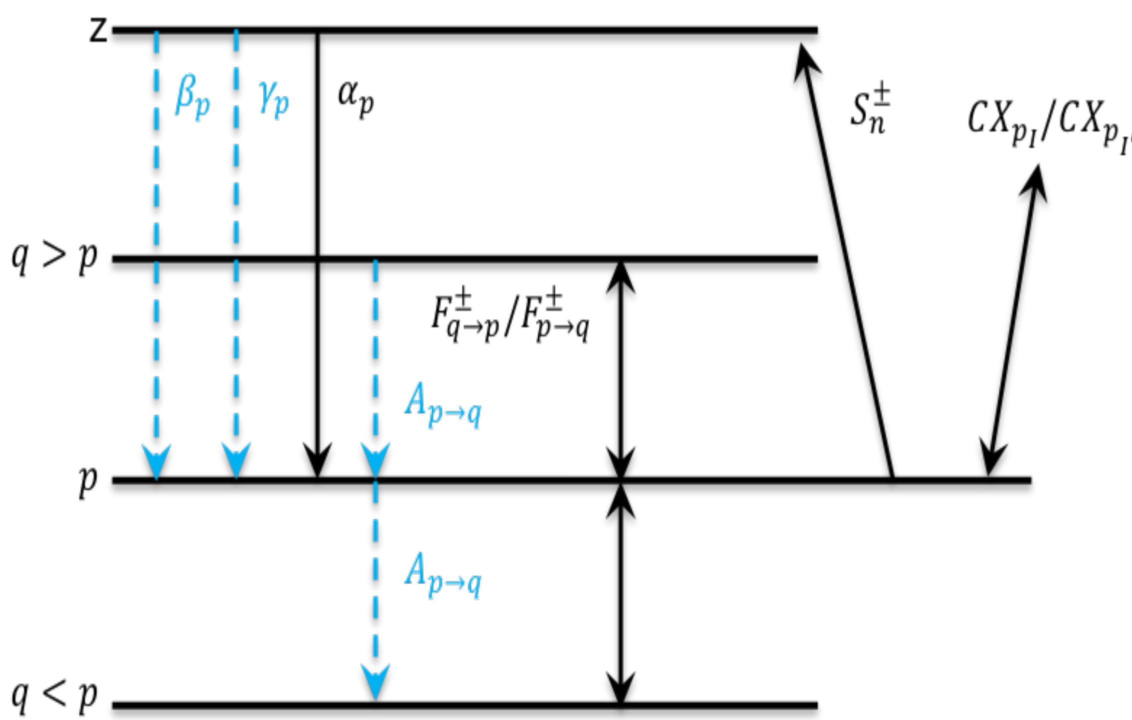

Figure 1.8. A general Grotian diagram of the transitions included in equation 1.2.2 and described in Table 1.1.

1.5 HELIOS Measurements in Tokamaks and Linear Devices

This section will be structured so that the motivation to improve HELIOS over the years by the community is highlighted through experimental results, interest of performing HELIOS on linear devices, and atomic data and modeling. HELIOS has been used on several devices over the years; five HELIOS applications will be reviewed in this section. The first three experiments were performed on the Tokamak Experiment for Technology Oriented Research [TEXTOR][1,6] and the Axially Symmetric Divertor EXperiment Upgrade [ASDEX-U].[7] These experiments are examples of the HELIOS diagnostic being implemented on tokamaks. They are also examples of a drive to improve the atomic data and the gas injection system for a more sophisticated HELIOS system. The last two experiments, performed on the Hot hELicon eXperiment [HELIX][9] and the NAGoya DIvertor Simulator – I [NAGDIS-I],[8] are examples of HELIOS performed on linear devices.

O. Schmitz, et. al.[6] performed beam emission spectroscopy [BES] on TEXTOR in 2008. Results from Schmitz's experiments can be considered the motivating factor toward improving the CRM and hardware for HELIOS. In the experiment, helium gas is injected into the low field side of the tokamak and the emission is optically viewed perpendicular to the gas puff. The same He I lines ($I_{667.9}$, $I_{706.53}$, and $I_{728.0}$) used in this thesis were used in the TEXTOR experiment. A CRM, denoted the TEXTOR CRM, is used for deriving T_e and n_e from the plasma edge and the measurements are compared to TS and fast probes. The TEXTOR CRM is a modification to a previous CRM by Brix[51] (that considered only electron processes) by adding collisions with heavy particles and a new atomic data set. Furthermore, an observation on the stationary solution and transient approach to solving the CRM is made as well. The stationary approach, which is usually calculated using a quasi-steady-state solution to the CRM, assumes rapid relaxation times for excited states. However, for the transient approach the quasi-steady-state solution is just an approximation. For the transient approach the time-dependent CRM must be solved iteratively.

The results showed that there were no significant deviations from the T_e and n_e values of the TEXTOR CRM and the BRIX CRM due to heavy particle collisions, but showed that higher T_e could be contributed to the new atomic data.[6] This is a significant result because it shows that determining T_e and n_e from the plasma depends heavily on the plasma physics and the quality of the atomic data that is used in the CRM. This fact is further shown in the result for the stationary and the transient comparison. Schmitz's experiment showed that this transient approach resolves longer relaxation times, which is significant for the metastable transition at low density. The transient algorithm mentioned in the paper would extend the HELIOS technique to further out into the SOL where densities are lower. O. Schmitz, et. al., presents HELIOS as a reliable diagnostic for $2.0 \times 10^{12}\ cm^{-3} < n_e < 2.0 \times 10^{13}\ cm^{-3}$ and $10\ eV < T_e < 250\ eV$.[6]

Four years later the first implementation of beam emission spectroscopy with the Filterscope system, officially dubbed HELIOS, was performed on TEXTOR.[1] In this experiment, the TEXTOR CRM and a new hybrid model was used to derive T_e and n_e measurements. This hybrid model, discussed briefly in Chapter 6, employed the improved cross-section data and the time-dependent algorithm to account for the significant metastable relaxation time at low density plasmas.[1,6,44] The hybrid CRM demonstrated improved T_e comparison with the TS measurements on TEXTOR than the original TEXTOR CRM.

Aside from the modeling improvements made over the years there has also been a focus on hardware improvements. In 2016, a new gas injection system (described in Chapter 2) was characterized and tested on ASDEX-U.[7] This new system can be placed inside the vacuum vessel of a plasma device, which allows the gas to be injected as close to the plasma edge as possible. The proximity to the plasma allows the new gas injection system to overcome the high divergence from the non-supersonic beam.

This section of the chapter has shown so far that the HELIOS technique has improved significantly and has been a consistent topic in the fusion community over an eighteen-year period. Since Proto-MPEX has $n_e > 2.0 \times 10^{13}\ cm^{-3}$ the most significant adjustment needed to the HELIOS CRM is the improved cross-section approximations for calculating the rate coefficients. However, the new gas injection system offers the possibility of improved gas penetration into the plasma. The final two experiments discussed in this sub-section are relevant to the linear nature of Proto-MPEX.

Both experiments performed on the HELIX ($1.0 \times 10^{9} \le n_e \le 5.0 \times 10^{12}\ cm^{-3}, 5.0 \le T_e \le 20\ eV$) and NAGDIS-I ($1.0 \times 10^{-11} \le n_e \le 1.0 \times 10^{13}\ cm^{-3}, 5 \le T_e \le 10\ eV$) are He discharges.[8,9] This is not directly comparable to the Proto-MPEX HELIOS, which uses neutral helium puffed into a deuterium plasma; however, the HELIX and NAGDIS-I experiments demonstrate the capability to perform helium line ratio spectroscopy on a linear device. HELIOS performed on Proto-MPEX will be more significant to the fusion community because

Proto-MPEX produces lower electron temperature and high electron density deuterium plasmas similar to the divertor region in a tokomak.

1.6 Overview of Thesis

This document will explore the use of HELIOS in the low T_e, high n_e plasmas of the linear device Proto-MPEX. The main focus of this study is to apply a 24-chord HELIOS diagnostic using a 100 kHz Filterscope and McPherson spectrometer. Chapter 2 and 3 will go into a detailed description of Proto-MPEX and its purpose and the gas injection system used for HELIOS. Chapter 4 is a description of the measurement instruments used for HELIOS. Chapter 5 is an overview of the validation data collected using HELIOS and the increased gas puff throughput experiment to improve the helium gas chance of reaching the plasma core. Chapter 6 introduces the concept of radiation trapping and re-analysis of the data, post modification of the CRM. Chapter 7 is the future work and conclusion of this thesis.

Chapter 2 Linear Plasma Devices and Proto-MPEX

Linear devices are necessary to bridge the materials gap between current MCF and power producing fusion plants. They offer dedicated experimental time for scientists to test different designs of PFCs due to the ability to swap out materials quickly between experiments. Testing these materials under different operational regimes, is feasible due to the capability to adjust radio frequency, microwave power, gas fueling, and magnetic fields in real time or between shots. Linear devices have reduced operational costs and offer improved diagnostic accessibility due to their circular cross-sections.

In the following sections of this chapter the motivation behind the user facility MPEX will be explained. The purpose of Proto-MPEX as it pertains to MPEX will be explained and the machine conditions used for the HELIOS validation studies and the gas penetration experiment will be described.

2.1 Motivational Drive behind MPEX

The motivating drive behind the user facility MPEX, a steady-state radiofrequency plasma source currently in design at ORNL, is a desire to have a facility that could study specific PMI needs by the fusion community. A tokamak does not have the diagnostic coverage necessary to understand PFCs. The plasma physics aspect of fusion development typically gets experimental priority over materials due to this inability to assess what is happening with the PFC itself. Therefore, it is necessary to build a dedicated linear plasma device to test and understand the PFC needs of future fusion reactors.

The user facility MPEX will allow scientists and engineers to perform novel experiments on materials. The materials will be exposed to high heat fluxes of 10-20 MW/m^2 and low temperature (< 2 eV), high density ($> 6 \times 10^{13} cm^{-3}$) plasmas, enabling more detailed erosion studies. Erosion can cause radiative power loss and dilution of the plasma fuel in a MCF device.[52] For future fusion machines with these heat fluxes it is expected that non-linear erosion will occur.[53] MPEX's ability to produce heat fluxes of 10 – 20 MW/m^2 on the target, coupled with its geometry that allows coverage by several diagnostics at the target region, will lead to a better understanding of the PMI physics..

Along with the high heat fluxes on the target is the question: "how does the plasma physics change?" In future devices it is expected that high densities (> $10^{15}\ cm^{-3}$) and low temperatures (< 1 eV) will dominate the divertor region of the tokamak.[53] The divertor region in Figure 2.1, is the exhaust region of the tokamak and where the strike points of the plasma reside. This plasma regime will need to be diagnosed to understand the plasma chemistry and atomic physics. Atomic physics plays a large roll in understanding PMI due to its use in transport codes. If the atomic data is not known then the transport, and ultimately the deposit, of impurities will not be understood. For example, if the eroded material is moving across fields into the core and the information supplied by the atomic physics is not accurate then this transport process will not be properly modeled, and corrective actions would be hard to make.

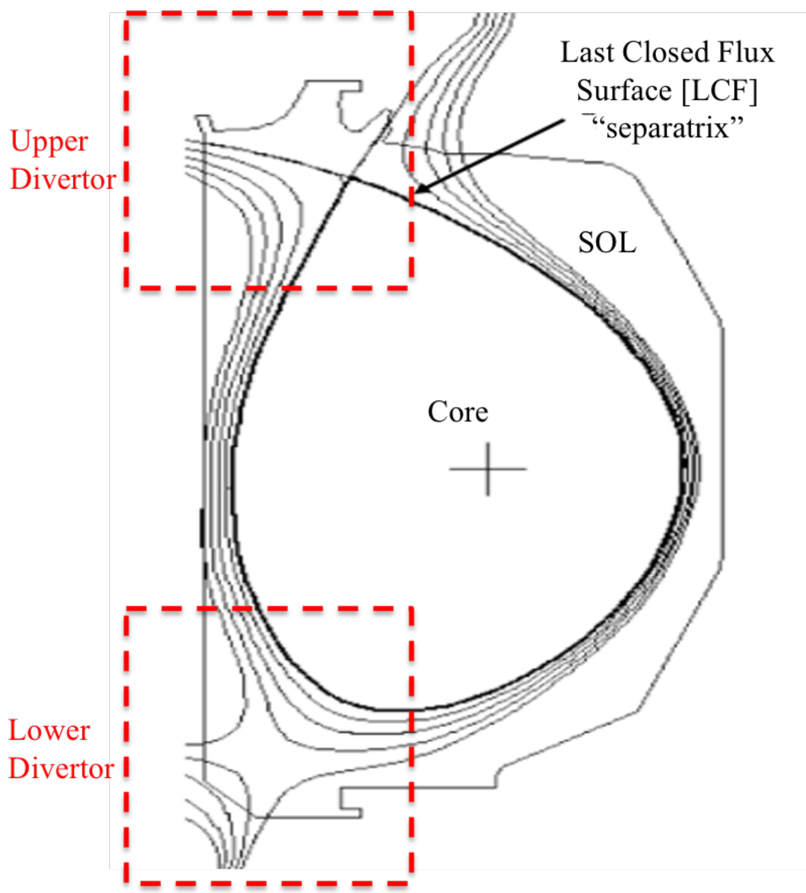

Figure 2.1Cross-Section of the Tokamak DIII-D

2.2 Proto-MPEX and Machine Parameters

Proto-MPEX, shown in Figure 2.2, is a linear plasma device that generates a low temperature ($1\ eV \geq T_e \geq 20\ eV$), high density ($n_e \geq 2e13\ cm^{-3}$) plasma. Proto-MPEX is the precursor to the user facility MPEX and is dedicated to source development and plasma conditioning. However, some preliminary PMI experiments will be performed. A helicon (whistler) antenna (120 kW/200 kW upgraded) is the primary source of heating on Proto-MPEX. Auxiliary heating is supplied by electron cyclotron heating/electron Bernstein waves [ECH/EBW] (50 kW – 100 kW) and Ion Cyclotron Heating [ICH] (30 kW). The helicon antenna and auxiliary heating sources are indicated on Figure 2.2. The half integer notation (1.5, 2.5, 6.5, 8.5, and 12.5) in Figure 2.2 is used by the Proto-MPEX team to indicate measurement, fueling, and diagnostic locations. Locations 1.5 and 2.5 are fueling locations, 6.5 is where the HELIOS studies were performed, and 2.5, 6.5, 8.5, and 12.5 are where pressure measurements are made. Figure 2.3 is an image of four separate machine parameters typical of a helicon only Proto-MPEX experiment (200 kW Helicon RF power, D_α emission, neutral pressure, and B-field). For source studies and plasma conditioning studies, several diagnostics have been installed on Proto-MPEX.

2D imaging capability on Proto-MPEX involves the fast Visible Cameras (fVC) and the Infrared Cameras [IRC].[54] The fVCs are commonly used for visible observations that include: ECH timing, gas puff timing and penetration, and probe positioning and survivability. The probes survivability can be seen in both images of Figure 2.4, where a 710 ± 20 nm filter is used to observe the plasma. Figure 2.4 also shows in the right-hand image the visible response of the plasma when ECH is turned on. The visible light of the plasma increases, and the plasma appears to increase in size. Within the ECH pulse the probe tip is actively arcing. The arcing is shown by the bright white light in the right-hand image of Figure 2.4. This means that the ECH pulse is damaging the probe tip. The probe was removed for repairs and it was found that the two tips had melted together

fVCs on Proto-MPEX have also been employed in 2D hydrogen Balmer series analysis at the target to observe the change in Balmer ratios[55] and are used in this thesis to show the localization of the gas puff using before and after gas puff images as can be seen in Figure 2.5. The images in Figure 2.5 are taken with a 710 ± 20 nm filter attached to the camera lens

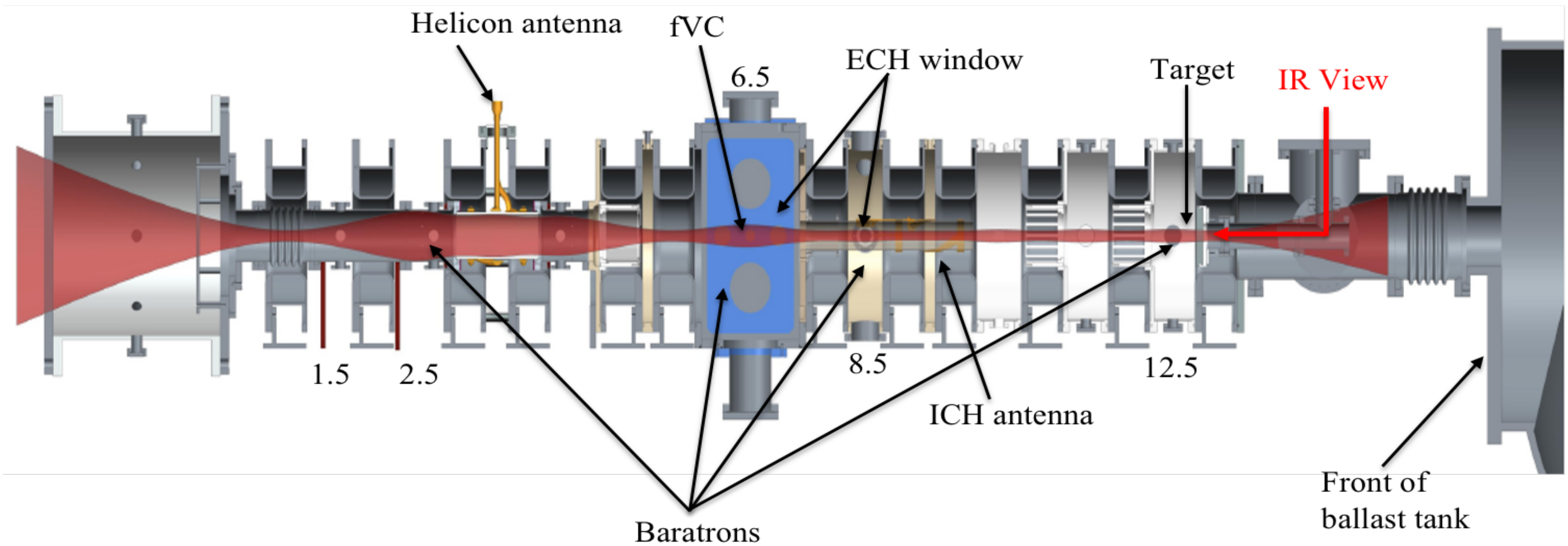

Figure 2.2 Cross-Section of Proto-MPEX

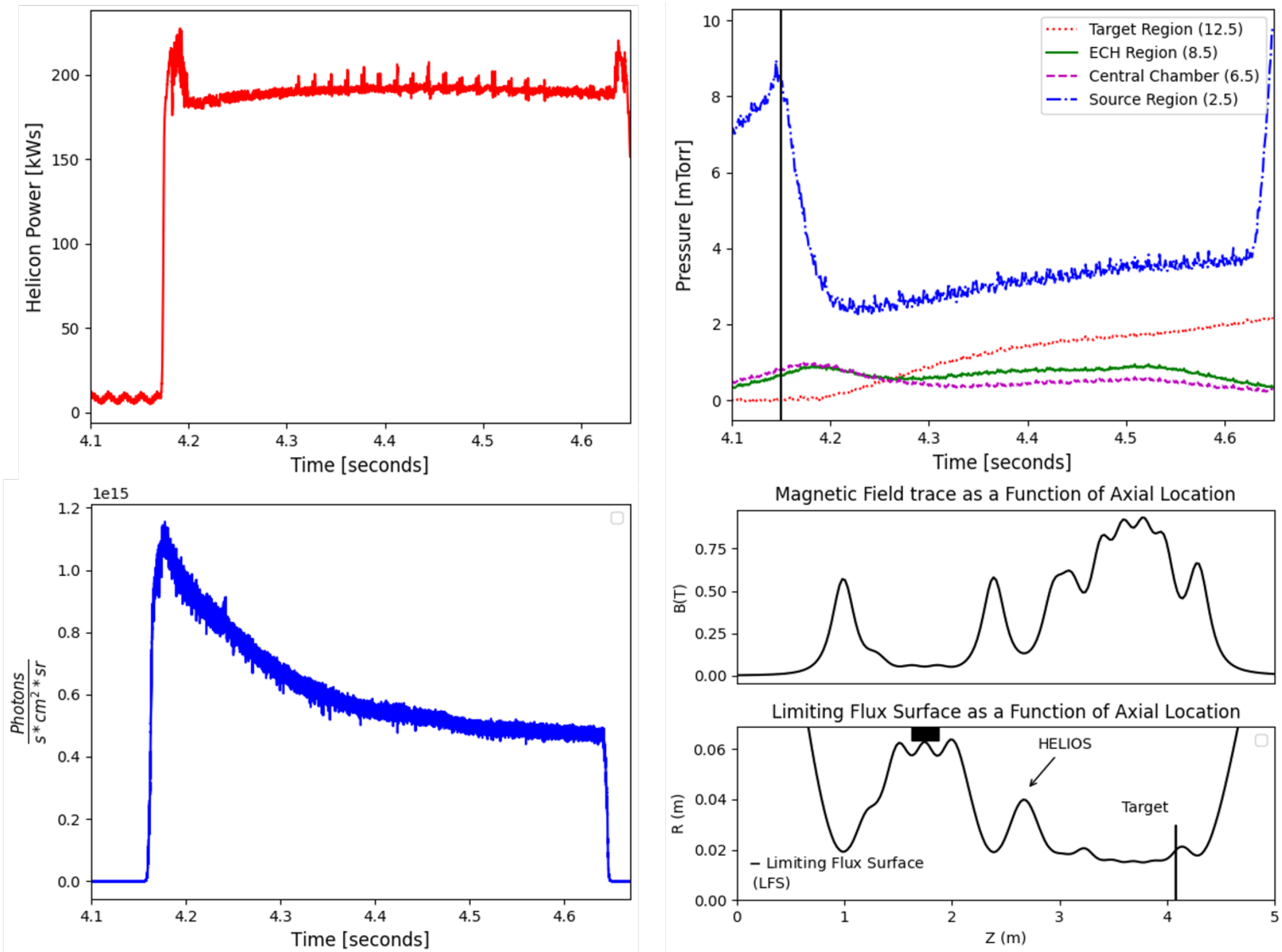

Figure 2.3. Typical machine parameters of Proto-MPEX during experiments.

Figure 2.4 Destruction of a DLP during microwave injection

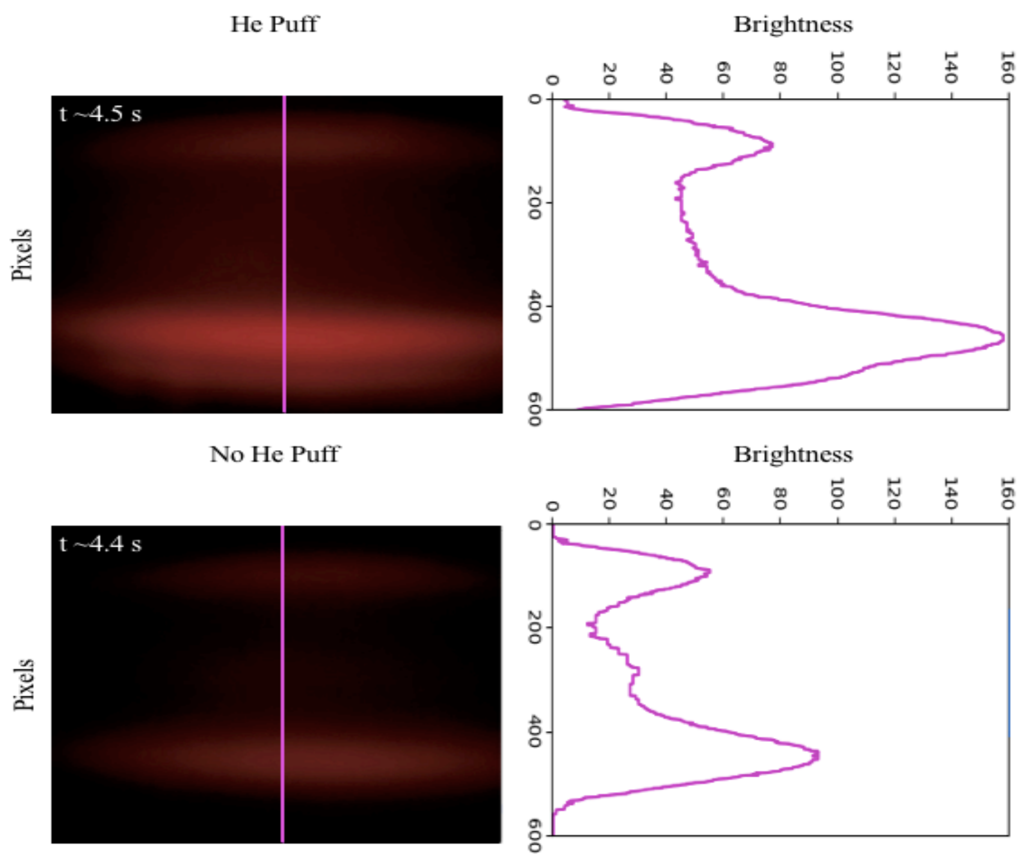

Figure 2.5 Two frames from the fVC video that is before and during the gas puff.

Infrared Cameras at the target and dump end of the machine have been used for heat transfer analysis and power accountability in Proto-MPEX.[54] Figure 2.6, a typical IR image at a specific time, shows the heat transferred to the target plate from the plasma. The red dashed circle is the size of the plasma footprint on the target plate and the red arrow indicates the radius of the plasma from core to edge. As can be seen the hot region of the plasma in this image is located at the bottom, which is very important information to be measured. This image shows that the core of the plasma is not the hot region as expected. Knowing where the hot spots are in the plasma column and on the target will improve understanding of plasma operations and future PMI experiments.

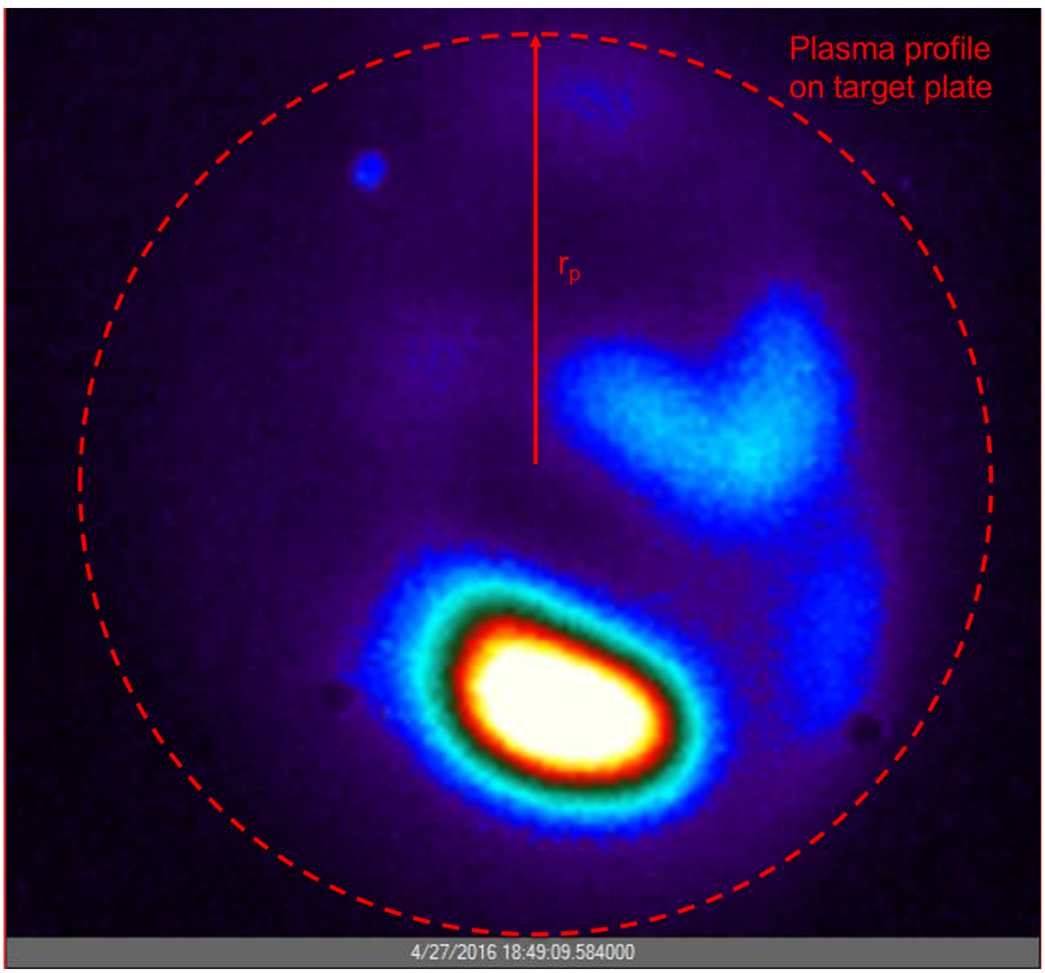

Figure 2.6 IR Image of the Target Plate

Spectroscopically, diagnostics such as the Filterscope radiometer, 1meter Czerny Turner McPherson spectrometer, and Ocean Optics [OO] spectrometer are available. Theses diagnostics are commonly used for HELIOS, D_α emission observation along the axis of the device, helium spectrum analysis,[56] ion temperature measurements,[57] and impurity observation.

Several of the filterscope Photomultiplier Tubes [PMTs] have a one-inch D_α (656.59 ± 1 nm) filter mounted in front of the PMTs to observe the signal from the plasma as it propagates down the machine. These signals are great for observing if the ECH is suspected to be arcing. When the ECH arcs there is clear disturbance in the Filterscope D_α signal during the ECH pulse as shown in Figure 2.6. The Filterscope is also used for HELIOS measurements and have the capability to measure hydrogen Balmer lines.

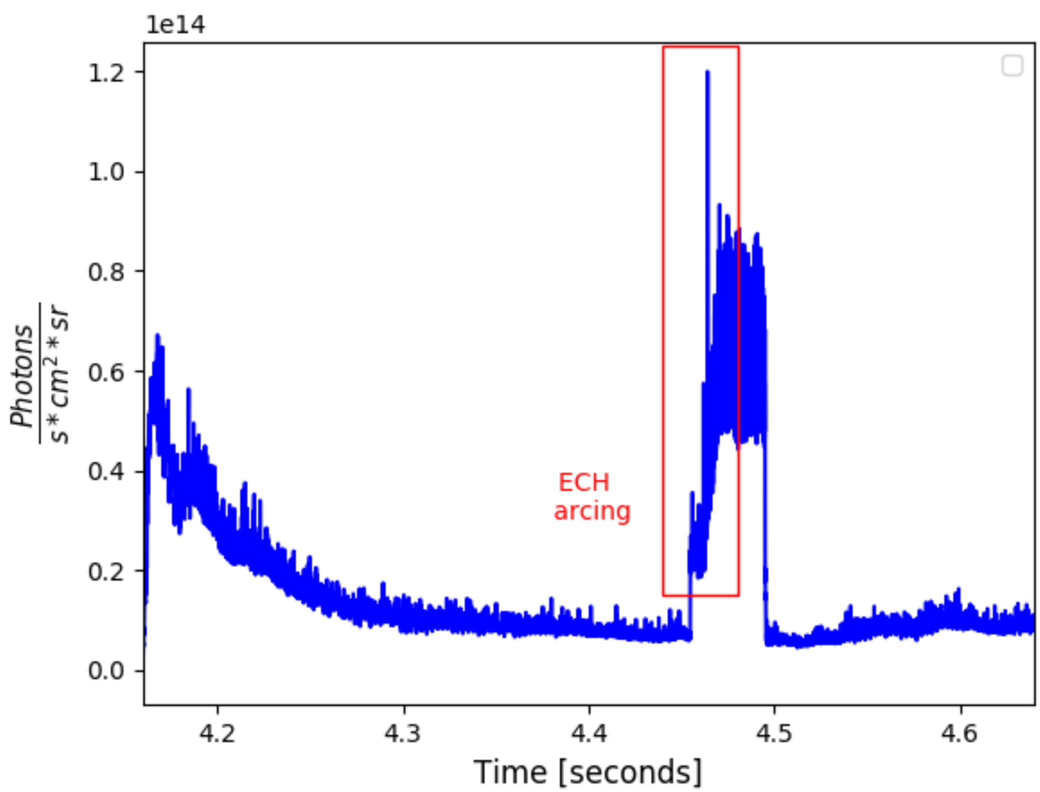

Figure 2.7. D_α signal showing an arc from the ECH during electron heating.

The McPherson spectrometer has been used in ion temperature, CH-band, and HELIOS measurements. It has also been used, prior to HELIOS installation on Proto-MPEX, to determine the optimal helium lines for HELIOS ratios.[56] The grating of the McPherson was scanned across all wavelengths during plasma operations. The data from the experiment showed that many of the helium lines were in very close proximity to other helium lines specifically ratio combinations. For the Filterscope to be used for HELIOS there cannot be polluting lines within the one-inch filters bandpass. The 667.90, 706.53, and 728.00 nm lines were remote enough to use the one-inch filters on the Filterscope without having to worry about polluting lines. Figure 2.8 is the peak intensity and the full spectrum from the McPherson helium scan experiment. In the right hand of the image, the peaks of the three He I lines of interest are shown. Their remoteness and decent intensity levels made them a great candidate for HELIOS on Proto-MPEX.

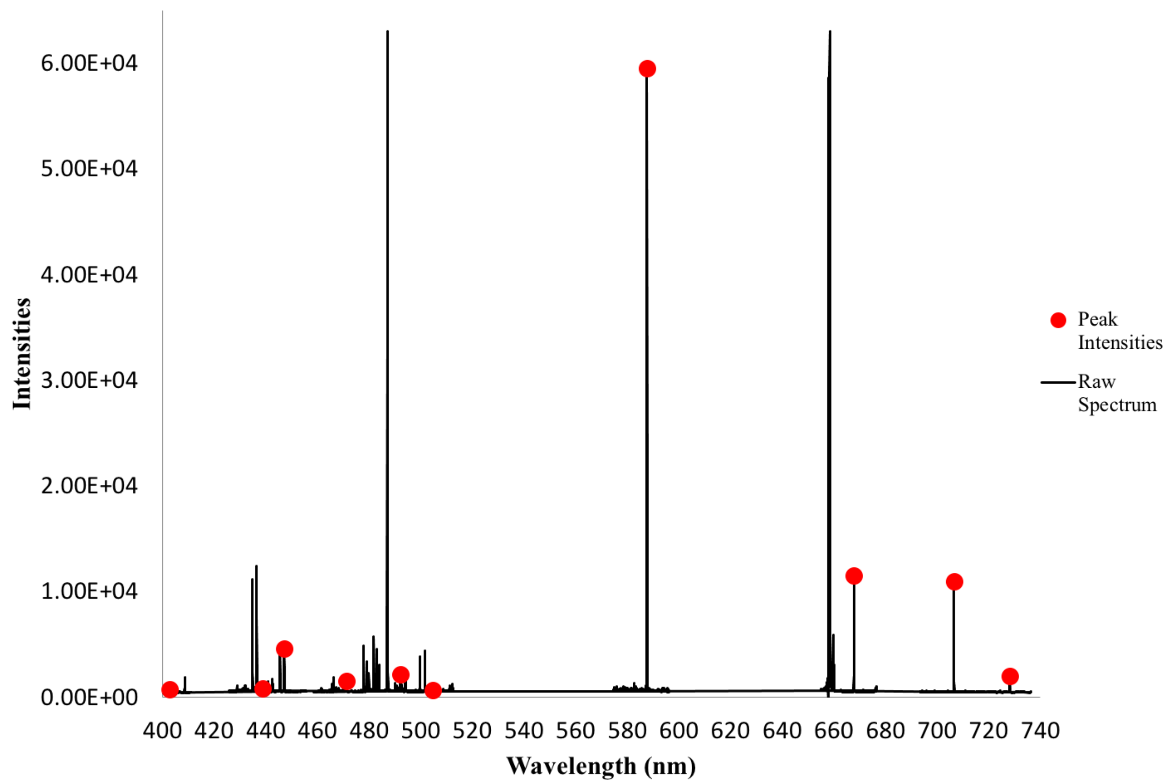

Figure 2.8. Average intensity of helium lines in Proto-MPEX[56]

The OO is a small portable spectrometer that is excellent for observing if there are impurities within the visible range in the plasma after a vent. For example, oxygen is an indicator that there are still levels of water vapor in the machine and that cleanup shots are still necessary. Figure 2.9 is a spectrum collected from the OO. The most notable thing about Figure 2.9 is the large peak at the center of the signal, D_α, and how it clearly dominates the spectrum with its high intensity. A prominent D_α peak is expected in Proto-MPEX's deuterium discharge. There are some low-level peaks that are close to the noise level of the instrument. The oxygen peak (O I) indicated on the spectrum is an example of a peak that is important, visible, but near to the noise level of the OO. If one wanted to analyze or inspect these signals the spectrum would need to be negotiated to focus on the peak of interest. Unfortunately, due to the large bandpass range of the OO (300 nm – 1100 nm) it has very low resolution. Finer resolution of wavelengths is not possible with this instrument. So, the OO is most often used for after vent machine operations to observe how well the machine is cleaning up after being exposed to the air.

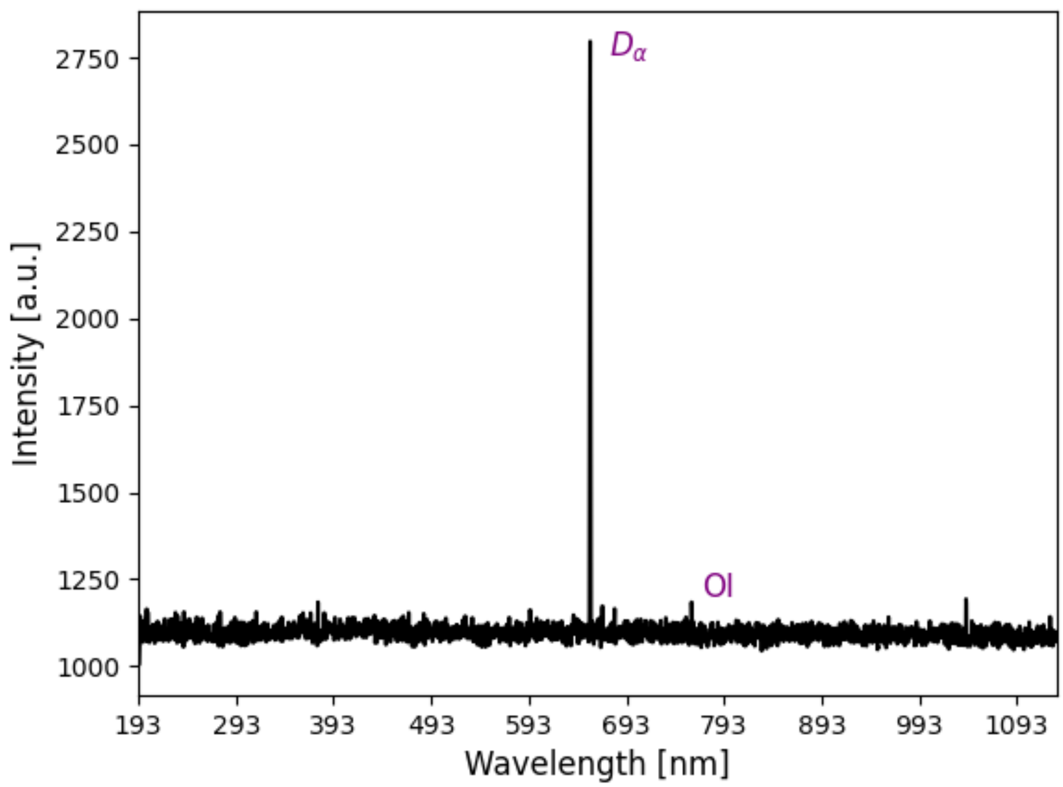

Figure 2.9. Ocean Optics spectrum from a Proto-MPEX plasma after a vent

The coil currents along Proto-MPEX are digitized and used in a field mapping code to understand the radius of the plasma during operations and where it might be limiting. In Proto-MPEX rather than a LCFS there is a Limiting Flux Surface (LFS) because none of the flux tubes make a complete closed surface, i.e. all flux tubes end on a material surface. Fluoroptic probes are attached to the helicon window so that the temperature of the window can be monitored between shots. This allows for operators to avoid overheating the window and causing any damages. The helicon window also operates more efficiently at certain temperatures. So, the Fluoroptic probes allow for more efficient operations.

Proto-MPEX has pressure gauges called Baratrons. The Baratrons record the pressure along key points of Proto-MPEX and are indicated in Figure 2.2: the source region (2.5), central chamber (6.5), ECH region (8.5), and target region (12.5). Pressure readings at the source help to ensure that the source plasma is not being altered between shots and to ensure the initial pressure during gas injection is right. The ECH region Baratron is used to monitor the pressure that the ECH/EBW operates with. The neutral pressure in the chambers give a nominal understanding of the neutrals in the vacuum chamber, which is good for understanding operations and maintaining a plasma. Figure 2.10 and Figure 2.11 are pressure readings during the validation study and during the gas penetration experiment, respectively.

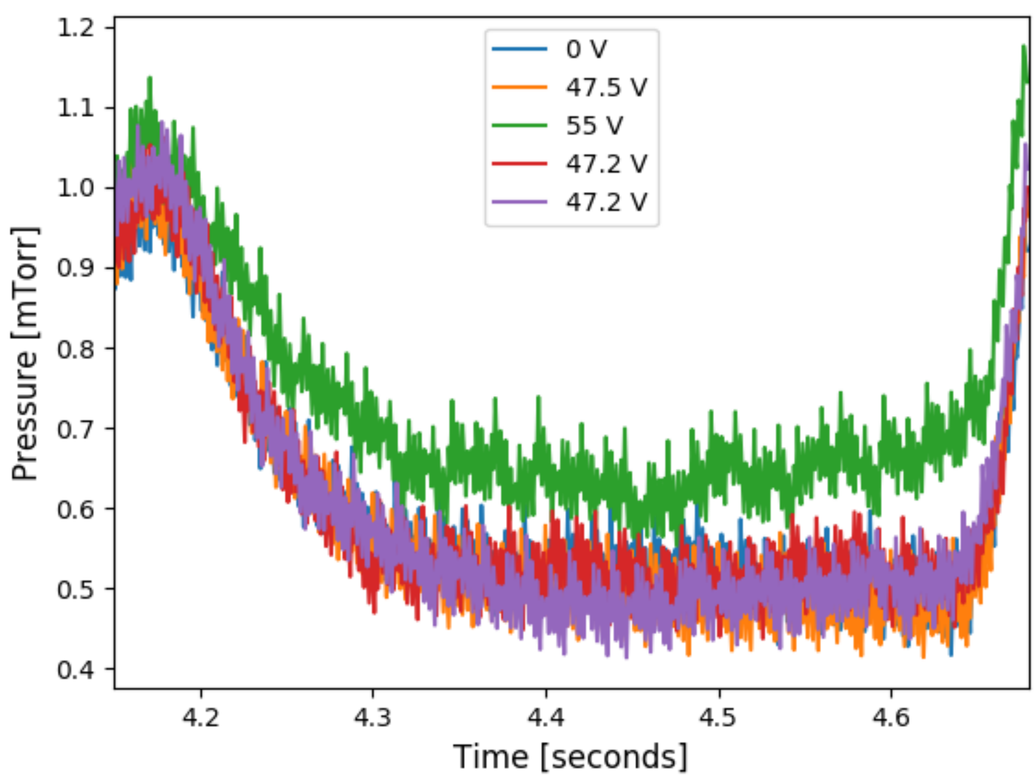

Figure 2.10. Pressure at the Central Chamber during Validation Studies

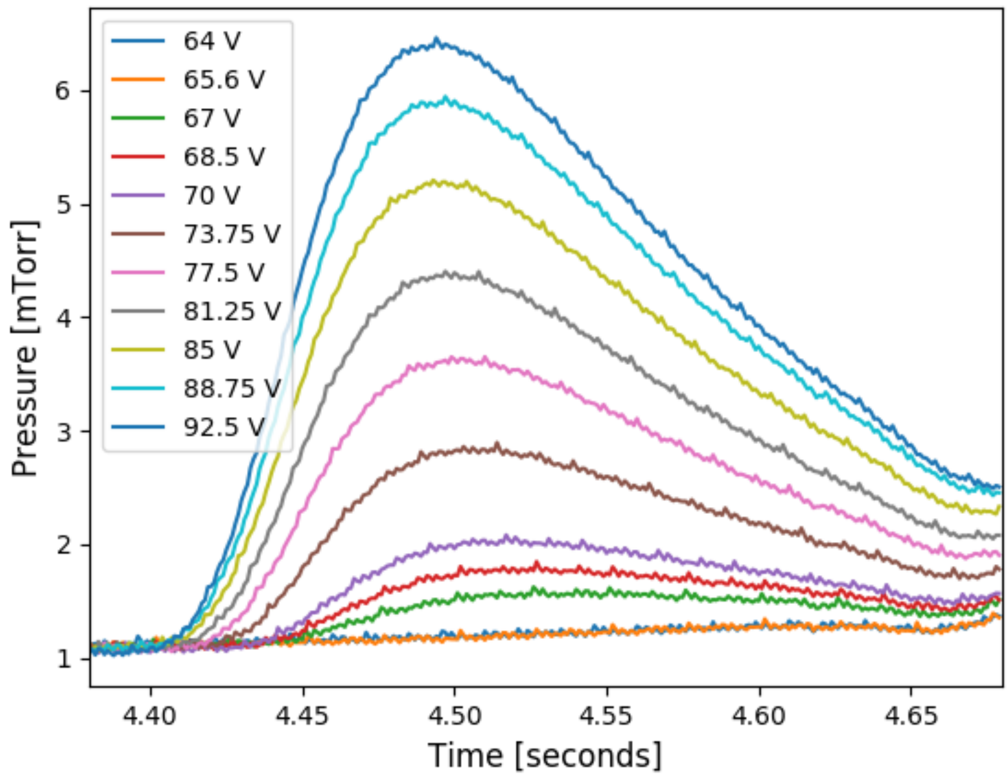

Figure 2.11. Baratron Pressure at the Central Chamber during the Gas Penetration Experiment

Double Langmuir probes (DLP), a Thomson Scattering (TS) system, and HELIOS are used for T_e and n_e measurements on Proto-MPEX. The following chapters will detail the gas injection system for the HELIOS diagnostic and DLP and TS data will be introduced.

Chapter 3 HELIOS Hardware Overview

The gas injection system for HELIOS is the primary subject of this chapter. When performing an experiment there is a drive to obtain the ideal system/diagnostic for measuring the optimal data; however, the ideal or perfect diagnostic is most of the time unattainable and an experimentalist must use what they have to achieve their goals. In the following sub-sections, the HELIOS diagnostic will be described in relation to an ideal system, while exploring the limitation imposed by the more realistic gas injection system and the light detection system. There are two gas injection systems on Proto-MPEX and their locations are indicated in Figure 3.1. The University of Wisconsin-Madison [UW-M] and PV-10 gas injection systems intrinsically operate the same way but are different in hardware implementation. There are two properties that make for a good gas injection system for HELIOS and will be discussed in the following sub-sections: Fast time response and localized gas puff.

3.1 Description of the Gas Injection Systems

Two different types of gas injection systems have been installed and used for HELIOS in two separate locations on Proto-MPEX. These gas injection systems are shown in Figure 3.2 and Figure 3.3. The design concept from the University of Wisconsin – Madison[3] [UW-M] utilizes a jenna[58] piezoelectric [piezo] crystal mounted in a stainless-steel, vacuum sealed box (133.35 cm^3). The UW-M design is pictured in Figure 3.2. The box is backfilled with gas at a specific pressure and the piezo crystal seals the outlet of the box by applying pressure to a Viton plate. When voltage (0 V – 130 V) is applied to the crystal it contracts for the duration of the voltage pulse, lifting the viton plate away from the outlet and letting the gas pass into the 400 μm diameter, 8 cm long titanium, zirconium, molybdenum [TZM] nozzle. The jenna piezo and viton plate that seals the valve outlet can be seen in the top image of Figure 3.5. The jenna piezo resembles an elongated hexagon and is fed an electric pulse by the wires attached to each end. The UW-M gas puff system is designed to withstand the harsh environment of the edge plasmas in a tokamak, allowing for the gas to be injected as close to the plasma edge as possible.[3]

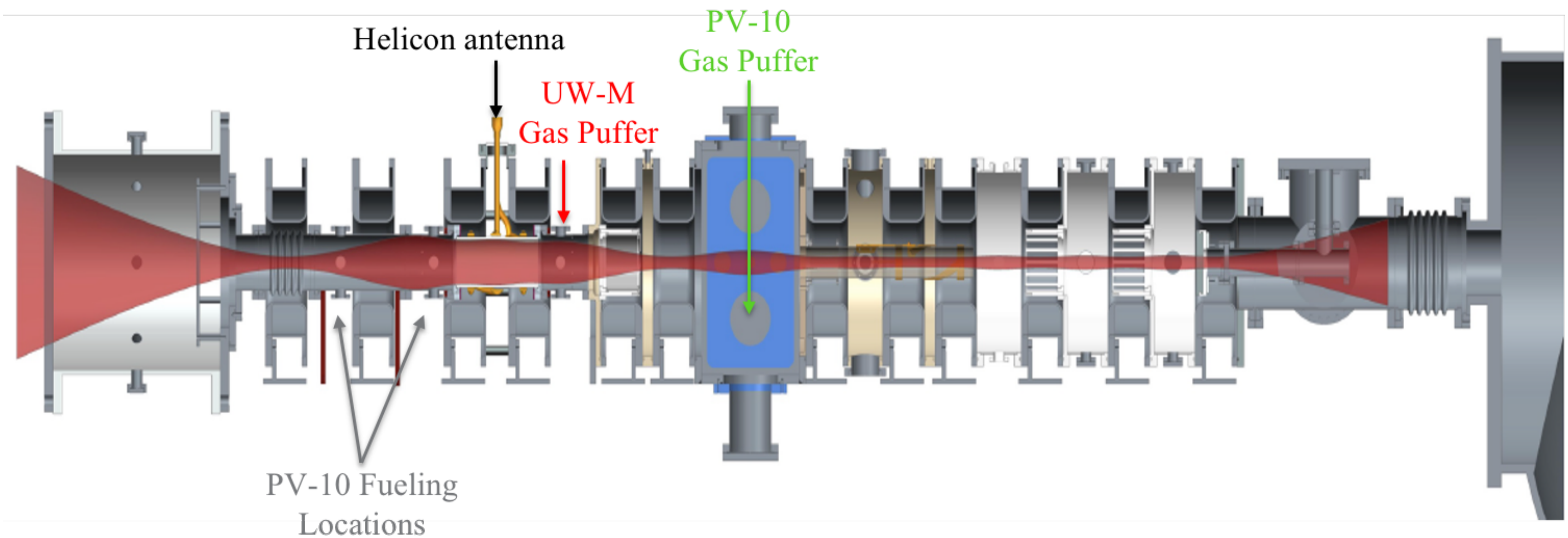

Figure 3.1. Axial cross-section of Proto-MPEX from when preliminary HELIOS data was taken.

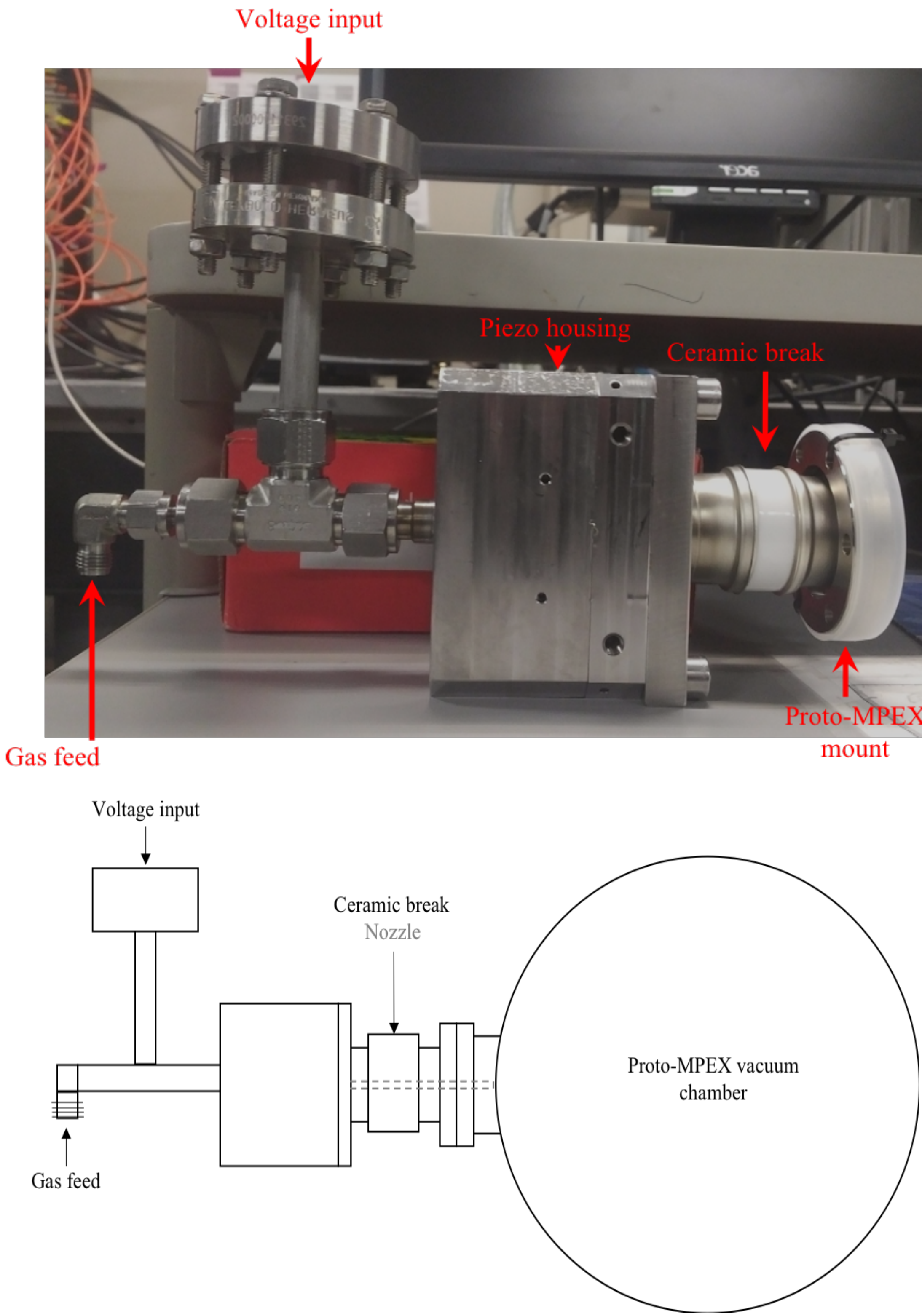

Figure 3.2. UW-M gas injection system design for Proto-MPEX.

Figure 3.2 points out the Proto-MPEX mount that allows the diagnostic to attach directly to the side of the machine. The early days of design for HELIOS on Proto-MPEX was driven by the need to measure $T_e$and n_e adjacent to the helicon window. Due to the perturbation of the DLP's to the helicon source coupling when inserted into the core near the helicon and no available TS beam line it became a priority to install HELIOS adjacent to the helicon antenna. Unfortunately, this location has a small vertical cross-section and 2 ¾ " flanges that would not accommodate the size of the setup. Hence, the UW-M gas injection system was mounted outside of the vacuum vessel as shown by the schematic in the bottom of Figure 3.2.

The second gas puff system, the PV-10 shown in Figure 3.3, was commercially made by Veeco Instruments and makes up the majority of the gas puff systems on Proto-MPEX. Similar to the UW-M gas puff design, a piezo crystal seals an exit aperture by applying pressure to a Viton plate in a stainless-steel cylinder of a smaller volume. The piezo, a small circular white plate, can be seen in the bottom image of Figure 3.5. PV-10s must be mounted external of the vacuum chamber and require a gas feed line to be installed. On Proto-MPEX a quarter inch pipe is welded to a 2 ¾" conflat [CF] flange that is connected to the PV-10 by a ceramic break. Ceramic breaks separate the gas puffer electrically from the machine ensuring that the electrical signal received by the piezo is undisturbed. The central chamber in Figure 3.4 is a rectangular volume of dimensions 40.64 x 68.58 x 66.04 cm so the length of quarter inch pipe to reach the edge of the plasma is much longer, ~35.56 cm from piezo to in vessel. The schematic in Figure 3.3 shows the angled pipe inside the vacuum vessel. This allows for the exit of the pipe to be somewhat closer to the plasma, but also attempt to have the gas puff normal to the collection optics.

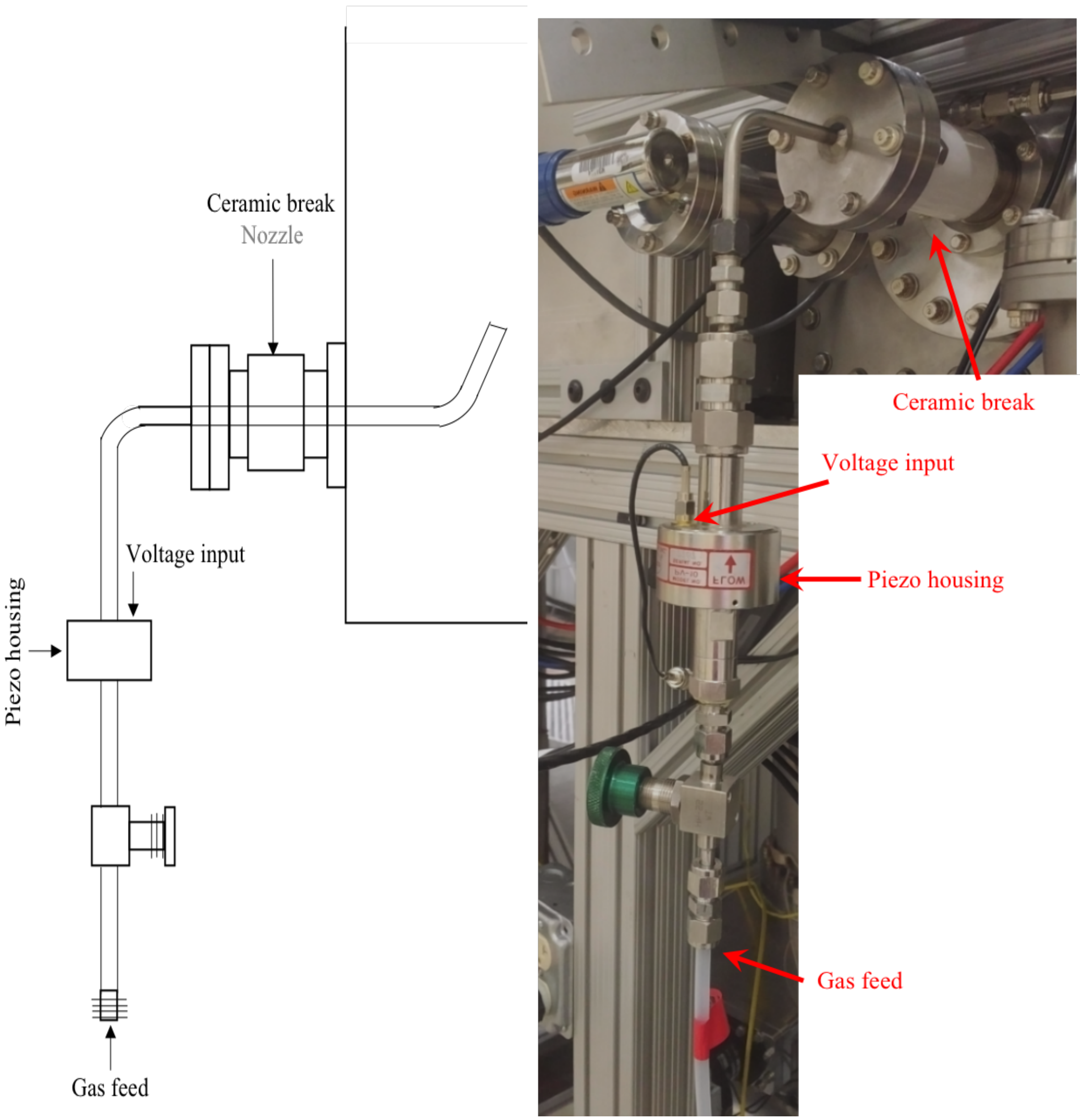

Figure 3.3. PV-10 at central chamber location.

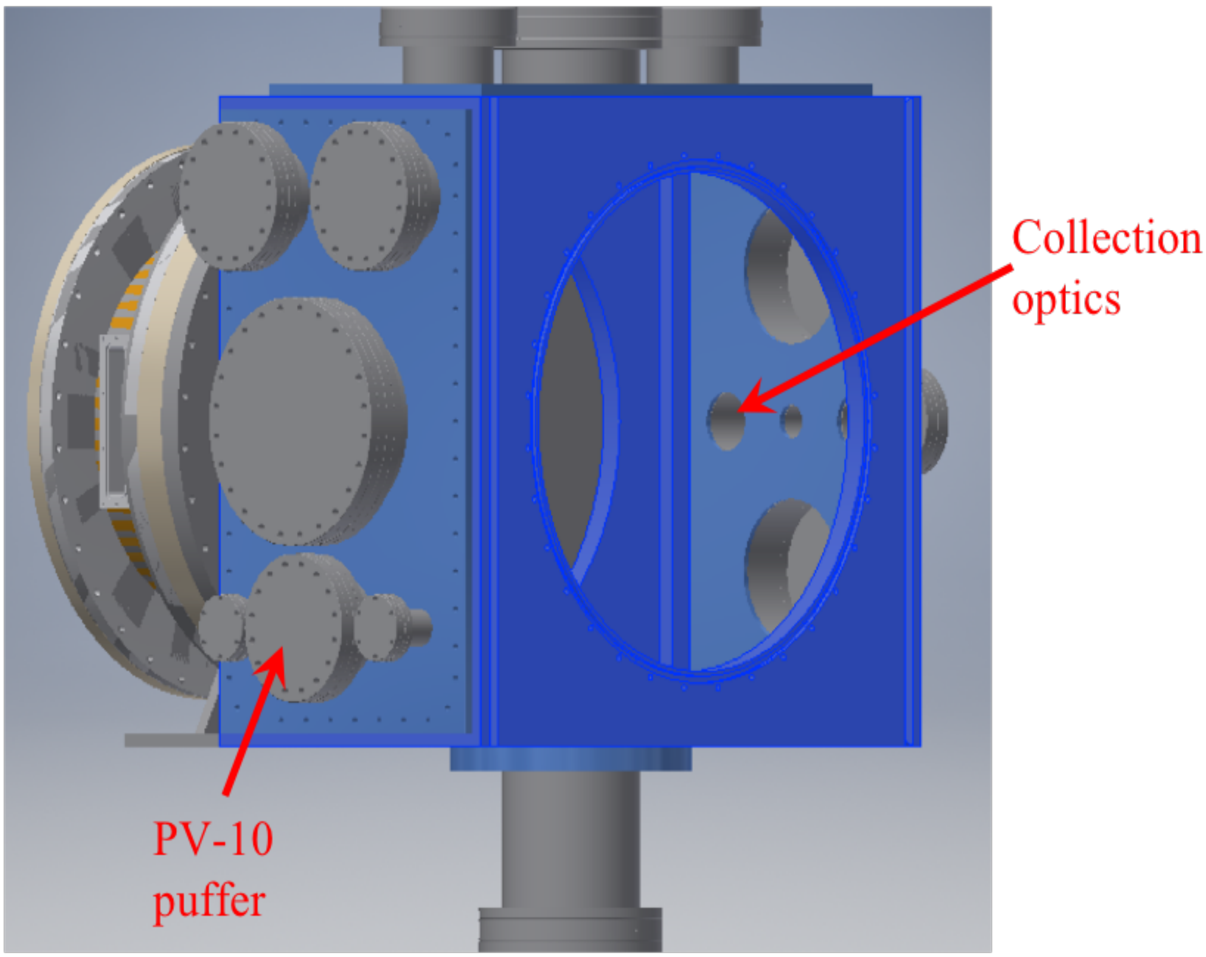

Figure 3.4. Engineering Drawing of the Central Chamber

Figure 3.5. The difference between the UW-M (top) and PV-10 (bottom) piezos and valve sealing mechanism.

3.2 Proto-MPEX Volume Calculation and Particles Injected by the Gas Puffers

Knowing the number of particles injected into the chamber by the injection systems is important because the helium is a secondary gas to the deuterium. If more helium particles are injected than the diatomic deuterium, then there is a high chance that the helium will be very perturbative and one would get a helium plasma. In order to measure, by pressure increase, the amount of gas particles entering the chamber when voltage is applied to the piezo the volume of Proto-MPEX must be determined. Using the UW-M gas injection system with a known plenum volume of $V_{box} = 133.35\ cm^3$ the Proto-MPEX volume can be calculated using Equation 3.2.1.

$$V_{Proto} = V_{box}\left[\frac{P_{final} - P_{box_{initial}}}{P_{test_{initial}} - P_{final}}\right] \qquad Equation\ 3.2.1$$

The box initial pressure is determined by back filling the plenum volume, which includes the piezo box and the gas line up to the piezo pin valve, and recording the pressure on the manifold gauge after the piezo pin valve is closed, $P_{box_{initial}} = 330\ \ Torr$. Closing the piezo pin valve isolates the gas in the plenum and keeps the initial pressure constant. The initial pressure in the vacuum vessel is recorded by the Baratrons after closing the turbo pump isolation valve, $P_{test_{initial}} = 0.14\ \ mTorr$. Before this step it is suggested that the turbo pumps should be pumping the chamber down to a low pressure, meaning that the isolation valve should be open during the initial box pressure measurements. Finally, the piezo is opened and the gas from the plenum is allowed to flow into the vacuum chamber and come to equilibrium. The equilibrium pressure recorded by the Baratrons is $P_{final} = 90\ \ mTorr$ and using equation 3.2.1 the volume of Proto-MPEX can be calculated, $V_{Proto} = 489.88\ L$.

The volume recorded here is the post 2018 modification volume after the ballasts tank was removed; however, the volume prior to this modification was $V_{Proto_{prior}} = 6621.71\ L$. The full equation derivation from the ideal gas law to equation 3.2.1 is written out in Appendix A. Figure 3.5 is a diagram to follow when calculating the volume of an unknown system such as Proto-MPEX and is labeled so that the above description can be repeated to solve for the volume of Proto-MPEX or similar system.

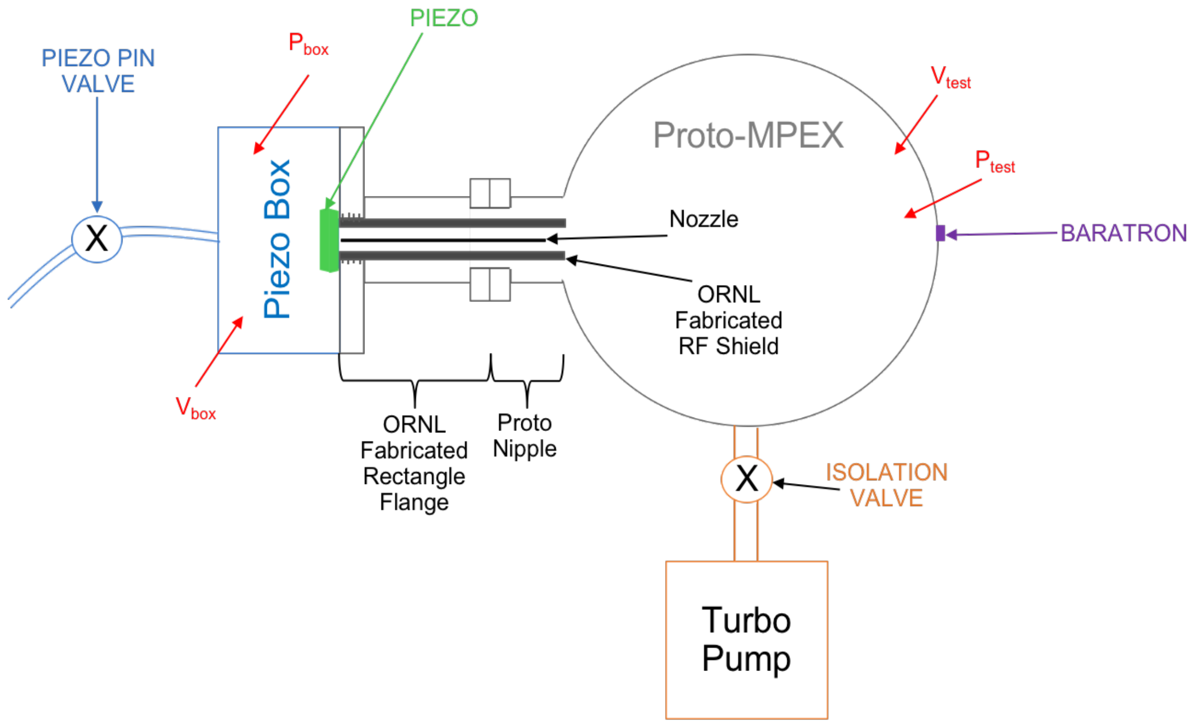

Figure 3.6. Schematic of the UW-M Gas Injection System and Vacuum Chamber to measure the Unknown Volume of Proto-MPEX.

The volume of Proto-MPEX was used to calculate the particles injected into the vacuum chamber by the gas puff systems. There are three fuel injectors for plasm operations: the mass flow control [MFC], 1.5 PV-10 (1.5B), and 2.5 manifold PV-10 (2.5M). The MFC was used for early machine operations and injected $N_{MFC} = 2.00 \times 10^{21}\ particles$. Figure 3.7 is the number of particles injected into the vacuum chamber using the PV-10 fueling injectors for 100 ms pulse lengths. The 1.5B piezo doesn't allow gas flow until ~66 V. It has a roughly parabolic increase in gas particle injection as the applied voltage increases. The 2.5M piezo at ~35 V allows flow, however, at ~47 V the amount of gas particles entering the vacuum vessel plateaus.

Figure 3.7 shows the particles injected into the vacuum vessel by two separate central chamber puffers in two separate configurations for 10 ms. The first configuration is the side mounted piezo (central chamber) and the second configuration is the top mounted piezo (central chamber), which is described in more detail in Chapter 4. Figure 3.8 shows that the gas puffed in by the HELIOS puffers is on the same order as the fueling injectors. Since the helium gas injected for HELIOS is on the same order as the fuel injectors, non-perturbing HELIOS will be more difficult to achieve. Also, the shorter the pulse width sent to the piezo the higher voltages required to open it. If the piezo is operated at higher pulse widths smaller voltages can be used to achieve different combinations of particles. Figure 3.9 is the particles injected and the throughput of particles injected into the vacuum chamber for different pulse widths (10 ms, 20 ms, and 50 ms) of the top-mounted central chamber gas puffer. The plenum pressure was ~1048 mbar. The top image is a great demonstration of how changing the pulse width allows for the piezo to open at earlier voltages. Since the piezo acts like a capacitor the longer the pulse length requested the longer the piezo has to charge at a specific voltage, leading to variation in the pulse width and voltage request for the HELIOS gas puffers.

The bottom plot of Figure 3.9 shows a very positive trend for the gas puffers. No matter what pulse width is chosen the throughput of particles exiting the piezo valve are close to identical. Only when the pulse width is small (10 ms) or at low voltages does the rate at which the particles exit the piezo valve not match up with the high pulse widths. This could mean that the small pulse widths represent that there is not enough time for the particle flow to level, meaning, they require a higher voltage to match the throughput. Pulse widths $\geq 50\ ms$ should have identical particle flows due to the higher pulse width.

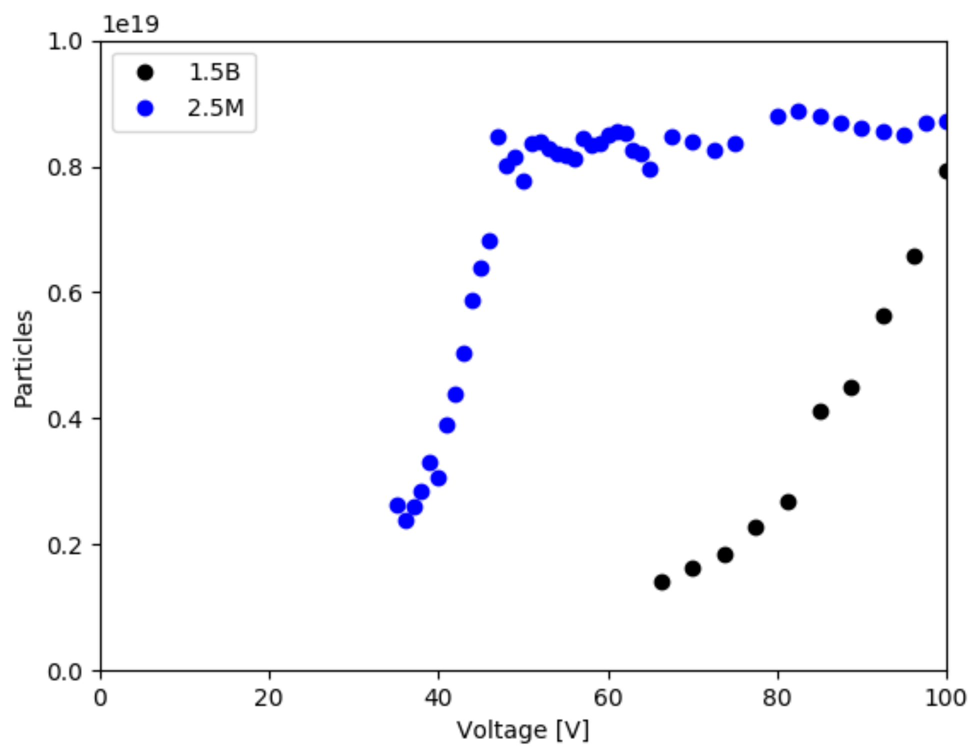

Figure 3.7. Fuel Injector Particles as a Function of Piezo Voltage

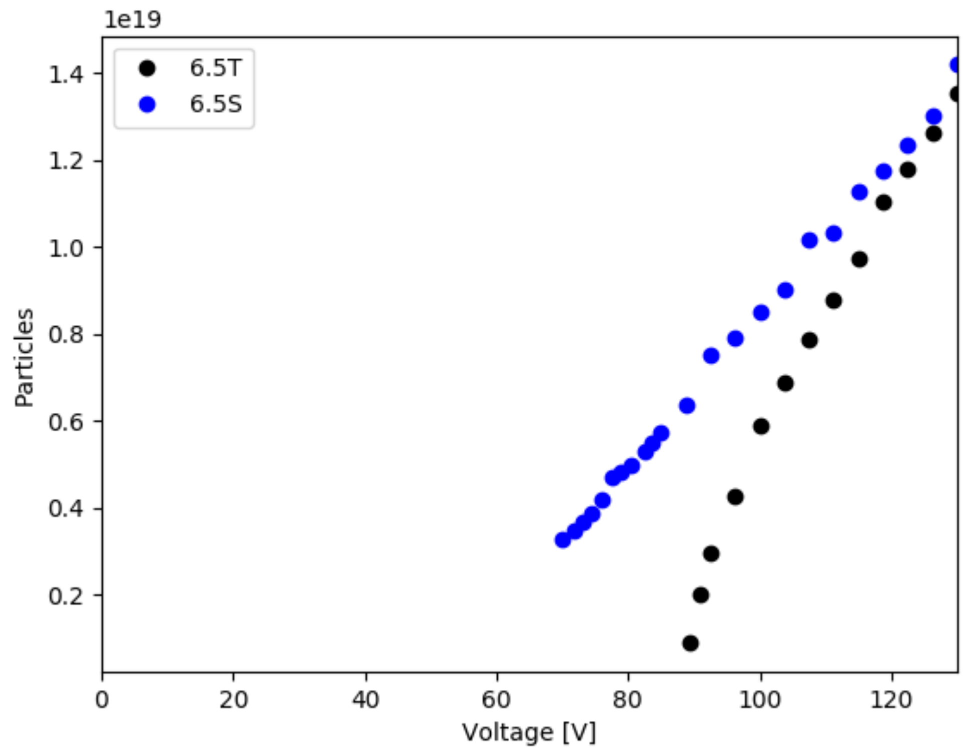

Figure 3.8. Central Chamber Gas Injection System for Two Separate Configurations

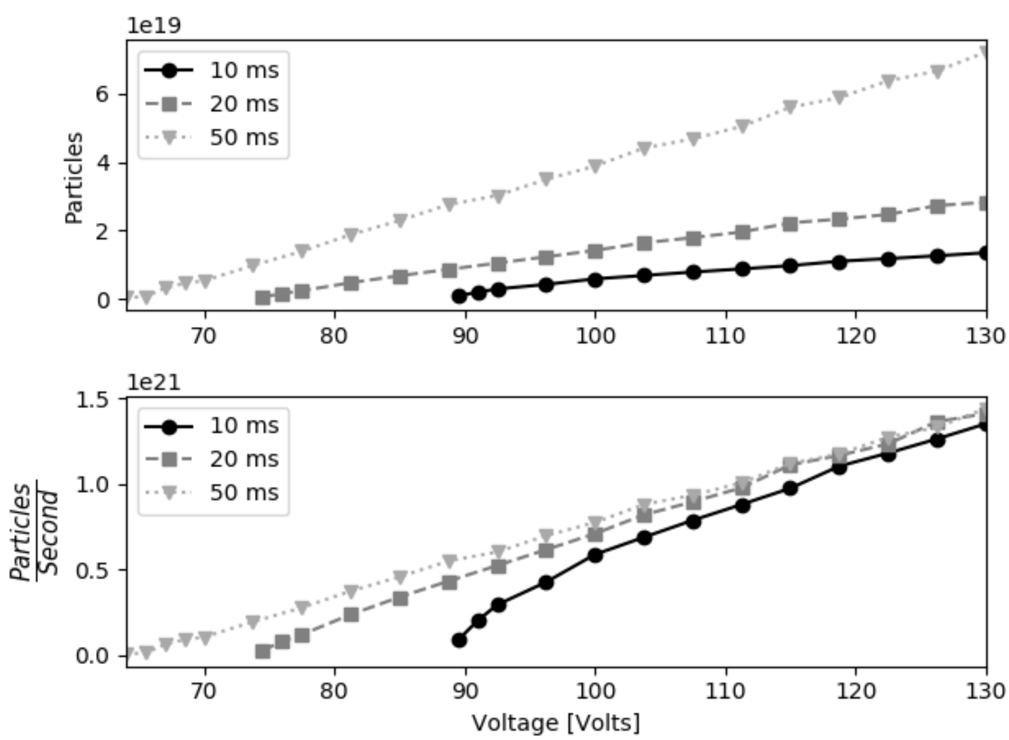

Figure 3.9. 6.5T Gas Injection System Particles and Rate of Particles Flow

3.3 Piezo Response Time

The gas is injected into the chamber by the contracting of a piezo, which opens an aperture and allows gas to flow freely through any nozzle or pipe. A voltage pulse of a specific pulse length and amplitude is requested by the user and sent to the piezo in the form of a voltage square wave. The piezo then contracts a distance, Δx, displacing a Viton plate originally at x = 0 mm, opening the aperture. In the ideal HELIOS puffer, the piezo would respond immediately to the voltage amplitude and only contract for the pulse width requested. For example, if a 40 V amplitude with an expected 0.3 mm displacement is requested by the operator for a 15 ms pulse width, then the piezo would instantaneously open at t = 0 ms when receiving the 40 V amplitude and close at t = 15 ms. Figure 3.10 is an ideal trace of the voltage response of the piezo when 40 V is applied to the crystal for 15 ms. The response of the ideal piezo would be instantaneous. This actual response, due to the fact that a piezo acts like a capacitor, can further be understood by considering Equation 3.3.1.

$$\Delta t = \frac{C * \Delta V}{I} \qquad \textit{Equation } 3.3.1$$

In the above equation, the capacitance, C, is a material property and is constant; therefore, the response time of the capacitor, Δt, is not only determined by the change in voltage, ΔV, but also the current output of the voltage supply or piezo driver, $I = I_{out}$.

For the example give in Figure 3.10, ΔV is supplied by the operator and equals 40 V. Therefore, for the response of the piezo to be instantaneous, Δt = 0 ms, the current output from the drive must approach infinity. Since $I_{out} = \infty$ is only viable for an ideal HELIOS piezo drive and not a realistic option for the systems on Proto-MPEX this response will be discussed further. Equation 3.3.1 introduced the governing equation for the time response of the piezos. The capacitance of the PV-10 and UW-M gas injection systems are $C_{PV} = 2.98 \times 10^{-2}\ \mu F$ and $C_{UW} = 3.27\ \mu F$, respectively. Since the time it takes for the piezo to respond is proportional to the capacitance one can already see that the UW-M will have a longer Δt than the PV-10, but since Δt is also inversely proportional to the current from the voltage driver, calculating out the Δt values for voltage drivers with different current outputs will help to determine the best hardware solutions for HELIOS.

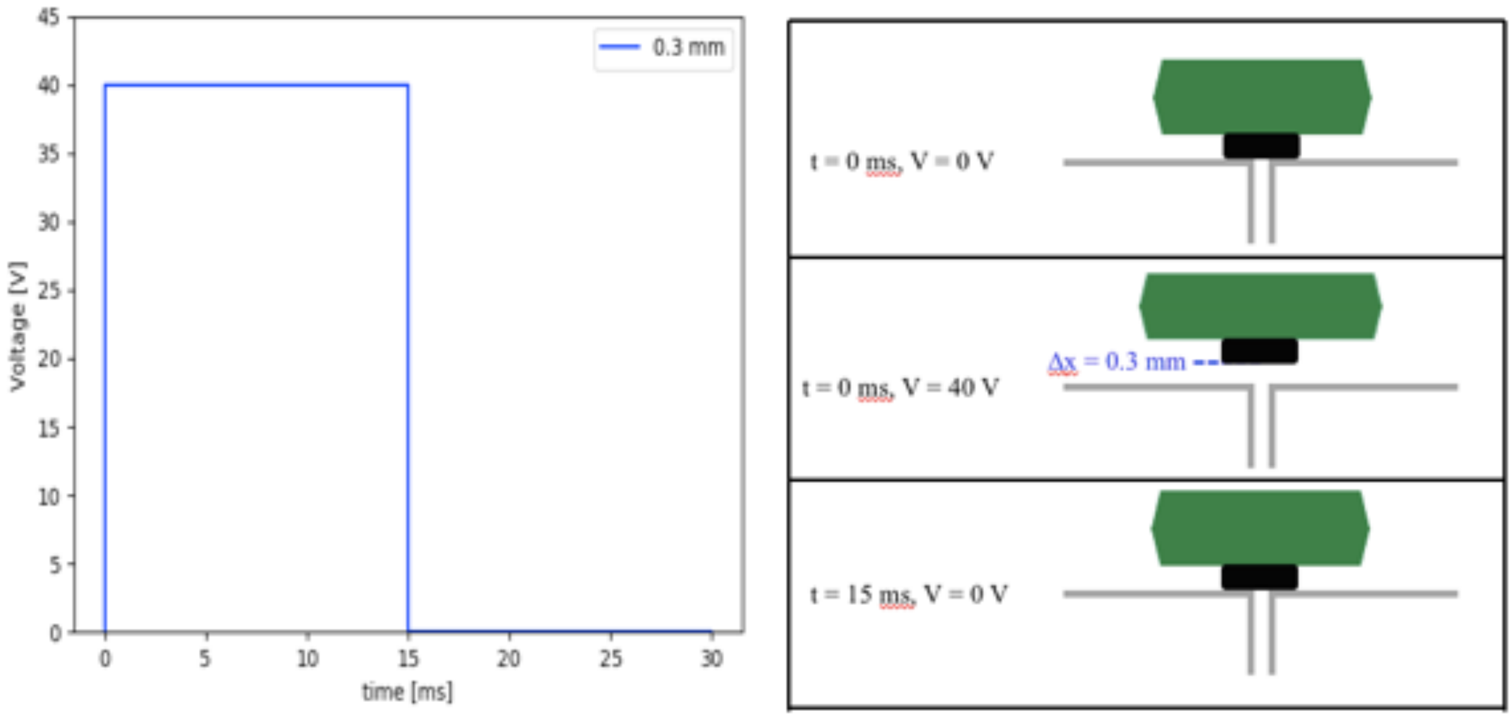

Figure 3.10. Ideal response of a gas injections system for HELIOS.

Proto-MPEX has three available voltage drivers for possible use with the piezos: a Jenna[42] system with $I_{JP} = 0.05\ A$ and two bi-polar amplifiers with $I_{B1} = 0.5\ A$ and $I_{B2} = 2\ A$. The Jenna system operates from -20 V to 130 V and the bi-polar amplifiers are from 0 V to 100 V. Each of these are compared to the response time of the $I_{JG} = 0.3\ A$ driver used for the design concept test of the UW-M gas injection system done by M. Griener.[3] The comparisons are shown in Table 3.1. The Jenna column and the Bi-Polar Amplifier columns in Table 3.1 show the response time of the UW-M and PV-10 piezos, respectively, for a range of voltages. The columns to the right of the ΔV column is the amount of time it takes for the piezo to respond to the voltage given or the Δt values. Table 3.1 shows that the fastest response is obtained with the $2\ A$ bi-polar amplifier and that the UW-M gas injection system is 110 times slower in responding than the PV-10.

TABLE 3.1. RESPONSE OF THE UW-M AND PV-10 GAS INJECTION SYSTEM TO FOUR VOLTAGE DRIVES WITH DIFFERENT OUTPUT CURRENTS.

	JENNA				Bi-Polar Amplifier			
	0.05 A		0.30 A		0.50 A		2.00 A	
ΔV	Δt UW-M (ms)	Δt PV-10 (ms)	Δt UW-M (ms)	Δt PV-10 (ms)	Δt UW-M (ms)	Δt PV-10 (ms)	Δt UW-M (ms)	Δt PV-10 (ms)
0	0.000	0.00E+00	0.000	0.00E+00	0.00E+00	0.00E+00	0.00E+00	0.00E+00
10	0.654	5.96E-03	0.109	9.93E-04	6.54E-02	4.28E-03	1.64E-02	1.07E-03
20	1.308	1.19E-02	0.218	1.99E-03	1.31E-01	8.55E-03	3.27E-02	2.14E-03
30	1.962	1.79E-02	0.327	2.98E-03	1.96E-01	1.28E-02	4.91E-02	3.21E-03
40	2.616	2.38E-02	0.436	3.97E-03	2.62E-01	1.71E-02	6.54E-02	4.28E-03
50	3.270	2.98E-02	0.545	4.97E-03	3.27E-01	2.14E-02	8.18E-02	5.35E-03
60	3.924	3.58E-02	0.654	5.96E-03	3.92E-01	2.57E-02	9.81E-02	6.42E-03
70	4.578	4.17E-02	0.763	6.95E-03	4.58E-01	2.99E-02	1.14E-01	7.49E-03
80	5.232	4.77E-02	0.872	7.95E-03	5.23E-01	3.42E-02	1.31E-01	8.55E-03
90	5.886	5.36E-02	0.981	8.94E-03	5.89E-01	3.85E-02	1.47E-01	9.62E-03
100	6.540	5.96E-02	1.090	9.93E-03	6.54E-01	4.28E-02	1.64E-01	1.07E-02
110	7.194	6.56E-02	1.199	1.09E-02	--	--	--	--
120	7.848	7.15E-02	1.308	1.19E-02	--	--	--	--
130	8.502	7.75E-02	1.417	1.29E-02	--	--	--	--
140	9.156	8.34E-02	1.526	1.39E-02	--	--	--	--
150	9.810	8.94E-02	1.635	1.49E-02	--	--	--	--

The 40 V example is shown again in Figure 3.11 but with the actual response of the UW-M and PV-10 gas injection systems from the highlighted red rectangle in Table 3.1 The UW-M piezo takes ~4 ms to respond to the full 40 V signal, but the PV-10's response is hard to discern from the ideal trace, making it an excellent choice for HELIOS. Even though the jenna did not produce the fastest response times its capability to reach higher voltage output (130 V) gives the puffer a better range of pulse lengths and gas densities, therefore, the PV-10 gas puffer with the Jenna is the leading gas puffer candidate for HELIOS. To make a complete study and decision of the gas injection systems the diagnostic setup (section 3.4) and gas dynamics (section 3.5) need to be understood.

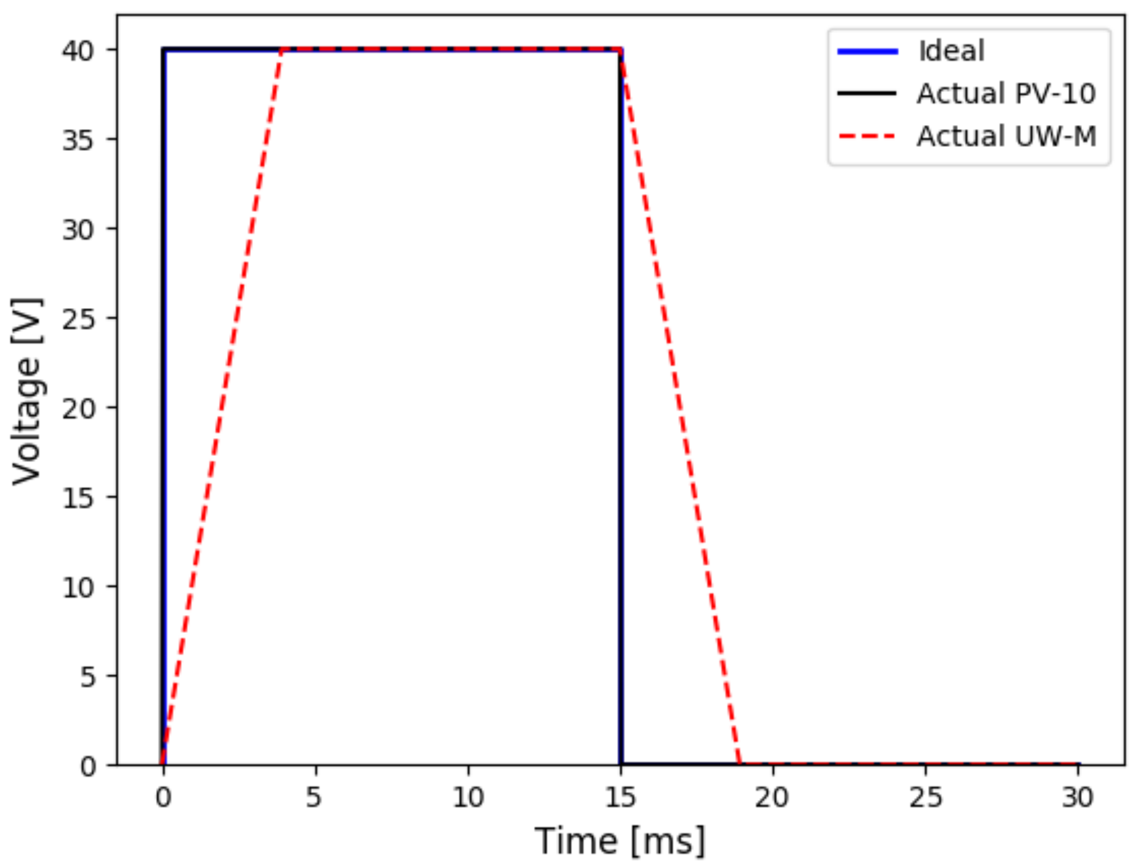

Figure 3.11. Actual Response of the PV-10 and UW-M Gas Puffers Compared to the Ideal Response

3.4 Ideal HELIOS Diagnostic Setup and Acquired Signal

Once the piezo contracts and the aperture is open the gas can flow through the opening and into the nozzle or pipe. Ideally the gas would flow through a narrow nozzle of minimum length and inject gas directly into the plasma as a thin collimated beam that penetrates and traverses all of the Proto-MPEX flux tubes. The injected particle flux would be, ideally, completely non-perturbative, meaning that all plasma parameters are undisturbed. Figure 3.12 is a cartoon illustration of the ideal HELIOS gas injection and optical setup. The nozzle is directly adjacent to the plasma edge and the red pencil thin line passing through the plasma cross-sectional area represents the gas puff. Figure 3.13 uses data from the cartoon in Figure 3.12 to illustrate the non-perturbative nature of the three He I lines, the quick response time of the piezo, the instant penetration of the gas puff (as shown as light intensity), and the resolved intensity of the 728 nm line. The helicon comes on at 4.15 seconds and stays on for a 350 ms pulse and the gas is puffed starting at 4.43 seconds. In Figure 3.13 the non-perturbative nature of the helium puffs (two hypothetical 10 ms gas puffs) is demonstrated by a lack of change in the D_α trace (magenta). The three He I line (I_{667}, I_{706}, and I_{728}) intensity signals quickly rise and fall for the two 10 ms gas puffs later in the trace between 4.44 seconds and 4.45 seconds. The helium signal prior to the gas puffs and after the helicon is turned on is the background helium in the chamber. This is subtracted off during the data analysis phase.

A well-defined duty cycle of 50% is visible in Figure 3.13 and is represented by the square wave signals of helium line intensities. The duty cycle is the percentage of time the gas puffer is puffing as compared to the total requested pulse width before another pulse width request is made of the piezo. Fast duty cycles is a perk of the fast-piezo response time and immediate penetration of the gas puff into the plasma. This quick response allows for background subtraction off the signals between gas puffs to account for any He I build up in the plasma. Ideally there would be no build up.

Eleven optical lines of sight measure the light intensity of the three He I lines considered in this paper. The eleven yellow chord lines of sight in Figure 3.12 terminate at the red beam of gas, meaning that the signals are localized to different radial locations on the x = 0 plane. Ideally, for a plasma of radius 3 cm, the HELIOS diagnostic would have enough optical chords to measure the light intensity of all three He I lines along the full diameter of the plasma column from r_P = 3 cm to r_P = -3 cm.

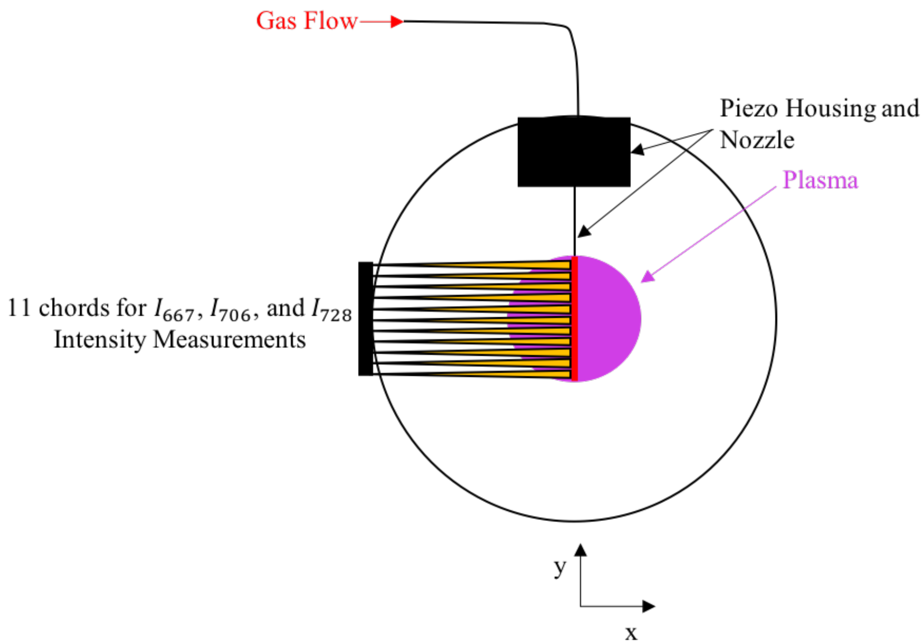

Figure 3.12. Cartoon illustration of the ideal HELIOS gas injection and measurement chords.

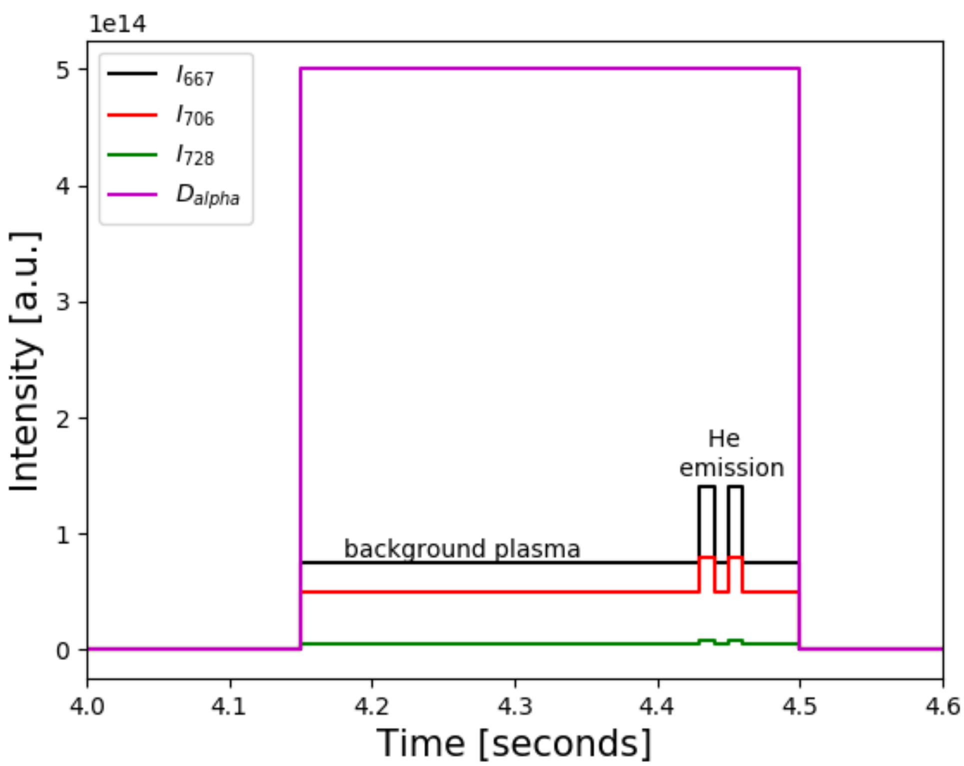

Figure 3.13. Ideal intensity data of the three He I lines considered in this paper (I_{667}, I_{706}, and I_{728}) and D_α.

This section has described the ideal HELIOS diagnostic and intensity signal; however, this is not the case with the actual system installed on Proto-MPEX. First, it has been determined in section 3.3 that the piezo response is not instant due to the driver output being finite and the inertia of the system. The length of pipe and distance between the plasma can cause the gas signal to be delayed and the conductance of the gas line plus vacuum chamber can cause the signal to last for longer than the requested pulse width. For the UW-M gas injection system this is not a huge issue because the 400 μm nozzle is adjacent to the plasma edge. Figure 3.14 is the signal response from the Filterscope when the UW-M gas injection system is used to request four separate gas puffs. The blue trace overlaid the intensities signals is the requested square wave sent to the piezo. Four waves were requested to start at 4.244 seconds (244 ms into the helicon pulse) at a voltage of 32.5 V for a duty cycle of 50% (10 ms on 10 ms off). The small signal at the lead is a great example of the piezo's need to charge because not only is it the smallest of the signals, but it is also delayed by 6 ms, meaning that the piezo needed at least 6 ms to reach 32.5 V and start responding. After this initial charge the following three signals response is comparable to the ideal signals in Figure 3.13. There is still a longer fall off time.

Similar to the signal response in Figure 3.14 is the central chamber PV-10 gas puffer response in Figure 3.15. The difference would be that there is only a single puff that lasts for much longer than the puffs in Figure 3.14. This longer rise and fall time can be observed in the He I signals shown in Figure 3.15. This suggests the need for improved response of the PV-10 gas injection system. The response of the piezo to the voltage applied is fine, but the ideal HELIOS has a response time that allows for background subtraction between gas puffs. The signal in Figure 3.15 is requested at 4.40 seconds into the helicon plasma with a pulse length request of 80 ms at 47.2 V, but the signal length is longer than 200 ms. The length is unknown due to the end of the plasma pulse, and because the signal did not show up until ~ 60 ms after the voltage request was sent. The side-mounted central chamber gas injection system is mounted external to the plasma chamber and has a long ¼ " diameter pipe as its nozzle. The nozzle is also some distance away from the plasma edge. The signal in Figure 3.15 suggests that due to the distance from the plasma column and the larger diameter pipe that the gas is delayed by ~60 ms reaching the plasma and the evacuation of the gas from the chamber and the plasma column takes a long time, especially compared to the length of the plasma pulse.

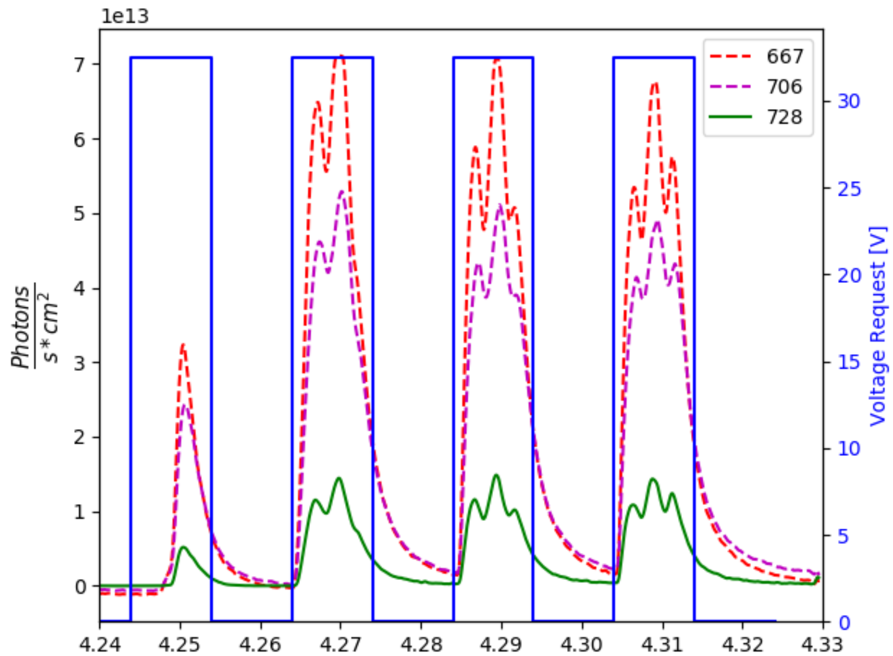

Figure 3.14. Signals from Proto-MPEX using the UW-M gas injection system, showing fast response and signal.

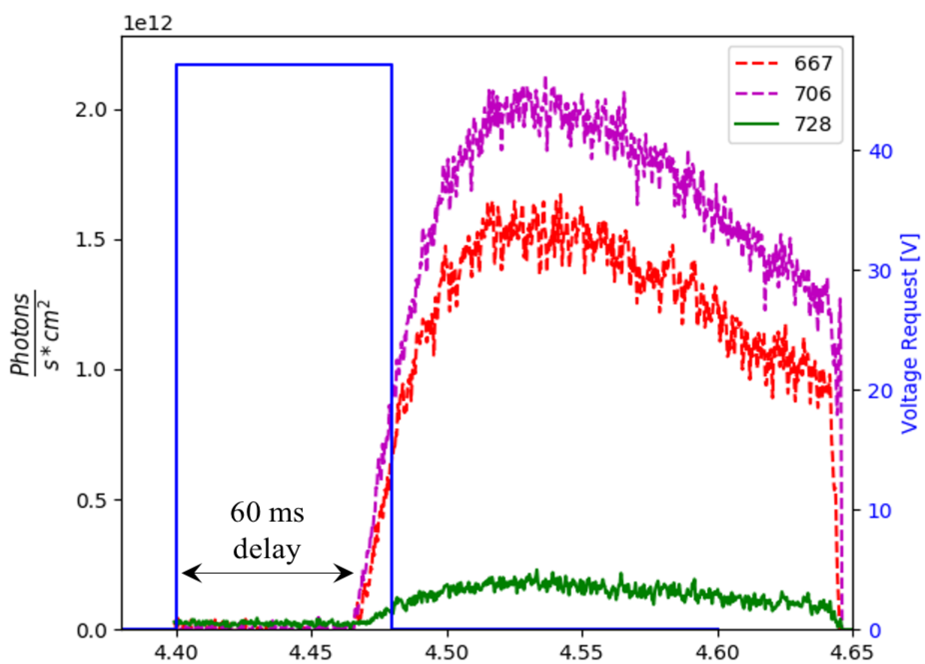

Figure 3.15. Signals from Proto-MPEX using the PV-10 gas injection system, showing long response and signal.

Figure 3.16 is a cartoon of how to explain the delayed phenomena of the signals. From Table 3.1 it is shown that for 40 V the 80 ms is an adequate amount of time for the piezo to charge. However, the intensity measured by the optical emission radiometer does not show until 60 ms after the requested voltage pulse. This is due to the second bracketed region in Figure 3.16. The slow rise time is due to the inertia of the piezo and the gas dynamics of the system. The gas dynamics include the pipe fill time and the amount of time it takes for the gas to reach the plasma column. The outlet of the PV-10 pipe is estimated to be 15 cm from the plasma column and the volumetric flow rate is calculated to be $\dot{V} = \nu D_p^2 = 4.518 \times 10^4 \frac{cm^3}{s}$, where the velocity, $\upsilon = 1.117 \times 10^5 \frac{cm}{s}$, is calculated from Equation 3.3.1, and the inner pipe diameter is $D_p = 6.360 \times 10^{-1}\ cm$. The Mach number, M, is assumed to be equal to 1, and the sound speed, c_s, is described by Equation 3.4.2.[59]

$$\nu = M * c_s \qquad \text{Equation } 3.4.1$$

$$c_s = \sqrt{\frac{2 * k_B * T}{m}} \qquad \text{Equation } 3.4.2$$

A single gas particle would take ~600 μs to reach the plasma column, $L_P \sim 50.8\ cm$, but it has been observed that the helium emission signal does not rise until 60 ms later. This implies that the outlet flow regime and the pipe distance from the plasma column plays a role in the time it takes for enough gas to reach the plasma for HELIOS signals with high response. The long fall off, shown as the last bracketed section in Figure 3.16, can be explained by the length of time it takes for the pipe to be fully evacuated of gas and the time it takes for the pumps to remove the gas from the chamber.

It has been observed that for the PV-10 it takes > 200 ms for the signal to fall off, meaning that it takes > 200 ms for the gas to exit the system. The large signal response of the PV-10 to the UW-M gas injection can be attributed to the differences in hardware installed on the gas injection systems and the locations. The PV-10 outlet was further away from the plasma column and has a larger diameter pipe to transfer the neutral helium to the plasma. The UW-M gas injection system is adjacent to the plasma column and has a 400 μm nozzle. Since the hardware effects of each gas puffer is understood there needs to be an examination of the gas dynamics of the two gas injection systems in order to fully grasp what is happening at the plasma.

The following section will discuss the important gas dynamics of the system that contribute to the operation of HELIOS on Proto-MPEX. The sub-section will be concluded by describing which of the gas puffers will be the leading HELIOS system and what will be done to improve the 1.) response time, and 2.) the localization of the gas puff.

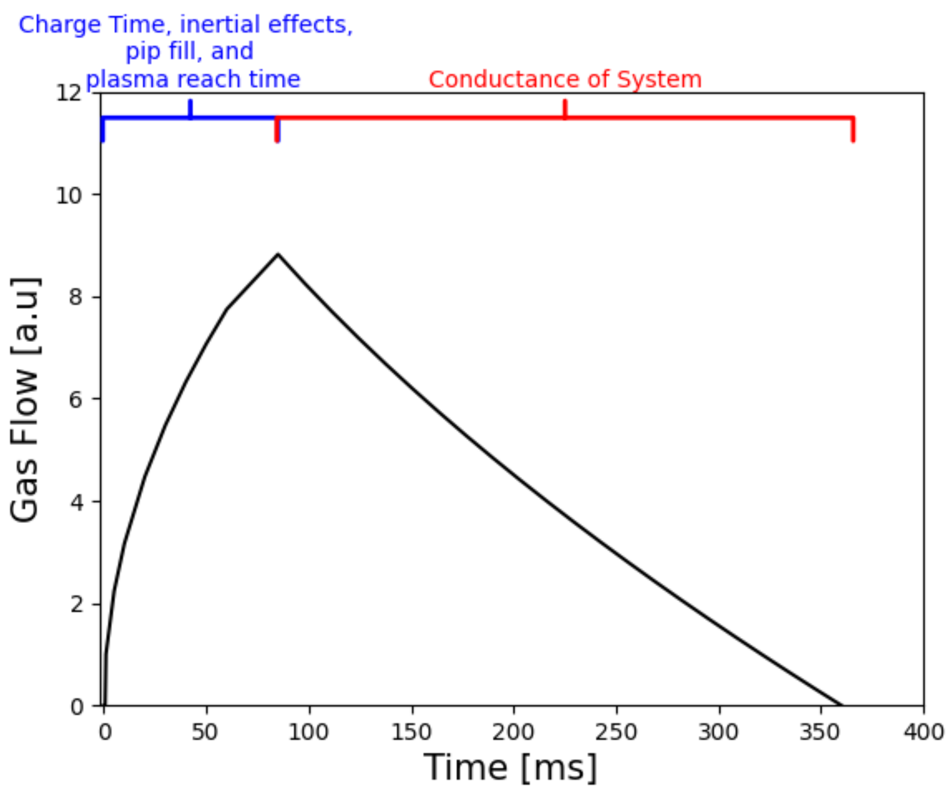

Figure 3.16. Cartoon illustration of the gas flow of the gas injection systems.

3.5 Gas Dynamics of both Systems

This section will describe the gas dynamics of the actual system of the Proto-MPEX HELIOS diagnostic, the shortcomings faced as compared to the outlined ideal system, and how to optimize the existing system for better results. There are several properties of gas flow that must be considered to have the best possible gas injection system. The first property to consider is the

Knudsen number [Kn], which determines the flow type and if fluid equations can be used to characterize the gas flow. The flow type is broken into three separate regimes: “molecular flow” is where wall-particle interactions are considerably greater than the particle-particle interactions (Kn ≫ 1), “transient flow” is where gas divergence at the outlet is improved and measured to be 20° (0.01 < Kn < 1),[7,60] and “viscous flow”, characterized by a large divergence at the outlet (120°), is the typical flow regime found in MCF gas injection systems (Kn < 0.01). In the last two regimes the gas flow can be characterized by fluid equations. The Kn is calculated using Equation 3.5.1.

$$Kn = \frac{\lambda_{mfp}}{D_p} \qquad \textit{Equation } 3.5.1$$

Where λ_{mfp} is the mean free path of the helium at $T = 300\ K$, and D_p is the inner diameter of the nozzle or pipe. The mean free path can be calculated by using Equation 3.5.2 and is inversely proportional to the backing pressure on the valve, P. Here, k_B is the Boltzmann’s constant and r_{shell} is the hard-shell radius of the gas particle (260 pm for He).

$$\lambda = \frac{k_B T}{\sqrt{2}\pi(2 * r_{shell}^2)P} \qquad \textit{Equation } 3.5.2$$

The central chamber gas injection systems with $P = 1117\ mbar$ and $D_p = 6.36\ mm$ has $Kn_{PV} = 1.94 \times 10^{-5}$. Similarly, the UW-M gas injection system at the same pressure but a $D_p = 0.4\ mm$ has $Kn_{UW} = 3.09 \times 10^{-4}$. Both gas injection systems can be characterized by fluid equations; however, since Kn_{PV} and Kn_{UW} are both less than 0.01 the flows fall into the “viscous flow” regime. This implies that no matter what change is made to the aspect ratio A, where $A = \frac{L_p}{D_p}$, the divergence at the outlet will not improve.[60]

However, Figure 3.17 shows that the flow can be moved into the “transient flow” regime by adjusting P. The top image in Figure 3.17 is an image of the Kn as a function of pipe diameter, D_p, at $P = 1117\ mbar$. At the chosen pressure all of the pipe diameters fall well into the “viscous flow” regime. The bottom graph in Figure 3.17 demonstrates what happens when P is changed for each of the pipe diameters in the top graph of Figure 3.17. As D_p decreases the Kn increases, but it is the decrease in P that makes the most significance. The bottom graph in Figure 3.17 shows that for the UW-M gas injection system, $D_p = 0.4\ mm$, $P < 35\ mbar$ produces flow that is in the "transient flow" regime. The larger diameter tube of the PV-10 at the central chamber does not shift into "transient flow" until $P \leq 2\ mbar$. It is important to note that the PV-10 valve diameter, D_v, is equal to about 2 mm, so even if the larger diameter pipe was removed the divergence of the PV-10 gas injection system would be in the "viscous flow" regime for $P = 1117\ mbar$.

With that said it is important to understand how the flow rate is affected by the nozzle or pipe after the valve outlet. Large diameter pipes attached to a small diameter valve may not influence the gas conductance. The best way to determine if a gas puff system is being 'valve limited' or 'friction limited' is to calculate the critical diameter, $D_{p,trans}$.[7,61] $D_{p,trans}$ is the transitional diameter between 'valve limited flow', meaning that the valve diameter influences the conductance of the gas puffer not the pipe diameter, and 'friction limited flow', meaning that the pipe friction reduces the outlet flowrate and the diameter of the pipe directly effects the conductance.[61] In order to calculate $D_{p,trans}$, a series of parametric equations must be solved that depend on the nozzle or pipe length, L_p, and valve diameter, D_v.[61] The UW-M gas injection system, $D_p = D_v = 400\ \mu m < D_{p,trans,UW}$, meaning that the nozzle is a gas flow limiting surface and a series of parametric equations must be solved to determine by how much.[61] The PV-10 gas injection system, $D_p = 6360\ \mu m > D_{p,trans,PV}$, is 'valve limited', meaning the pipe does not limit the gas flow and so the pipe attached to the end of the PV-10 does not influence the conductance of the gas puffer.

It has been determined that the PV-10 puffer is 'valve limited', meaning that the larger diameter pipe attached to the valve outlet does not affect the pipe conductance, and that the flow is in the 'viscous flow' regime. The conductance of the PV-10 gas puffer can be calculated. Since the PV-10 is 'valve-limited' the conductance, $\mathbb{C}_{PV-10} = 4.44 \times 10^{-5}\ \frac{m^3}{s}$, of the gas puffer is calculated using the valve diameter and equation 3.5.3. Equation 3.5.3 is a thin hole approximation with a thickness, $L_v \approx 1.27\ cm$, and transmission probability, $K(A, L) = 0.02$.[62,63]

$$\mathbb{C}(A, L) = \frac{Av}{4} K(A, L) \qquad \textit{Equation } 3.5.3$$

For the UW-M gas puffer, which is 'friction limited' and the gas flow is in the 'viscous flow' regime, the conductance, $\mathbb{C}_{UW-M} = 2.41 \times 10^{-5}\ \frac{m^3}{s}$, can be approximated using equation 3.5.4,[64] where $P_{Avg} = \frac{P_{chamber} - P_{plenum}}{2} \approx 5.58 \times 10^2\ mbar\ (5.58 \times 10^4 Pa)$, $L_{UW-M} = 8\ cm$, and $D = 0.04\ cm$.

$$\mathbb{C} = 1349 \left(\frac{D^4 P_{Avg}}{L_{UW-M}} \right) \qquad \textit{Equation } 3.5.4$$

It is important to note that the Reynolds number for the PV-10 gas injection system and the UW-M gas injection system are $Re_{PV-10} \approx 2105$ and $Re_{UW-M} \approx 421$, respectively. The PV-10 puffer is right on the border of transitioning to turbulent flow and the UW-M puffer is laminar, meaning that the calculations of conductance are good approximations of the flow. One can determine the amount of time it would take for the gas to flow through the pipes by dividing the conductance by the volume of gas injection systems' nozzle, $V_{PV-10} = 2.02 \times 10^{-5}\ m^3$ and $V_{UW-M} = 1.00 \times 10^{-5}\ m^3$. The UW-M gas injection system takes $0.42\ ms$ and the PV-10 takes $455 - 364\ ms$ to exit the gas nozzle. These measurements back the measurement observation made in section 3.4, Figure 3.14 and Figure 3.15, where the UW-M gas injection system demonstrated quick signal response and the PV-10 demonstrated a delayed, ~60 ms, and long lasting signal.

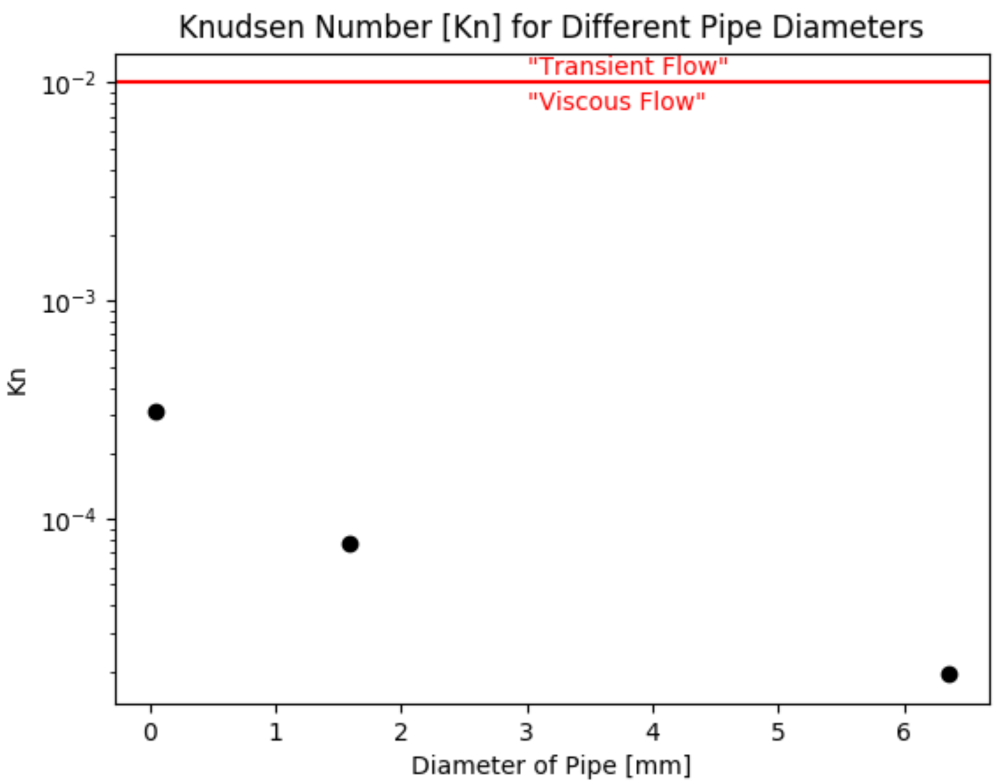

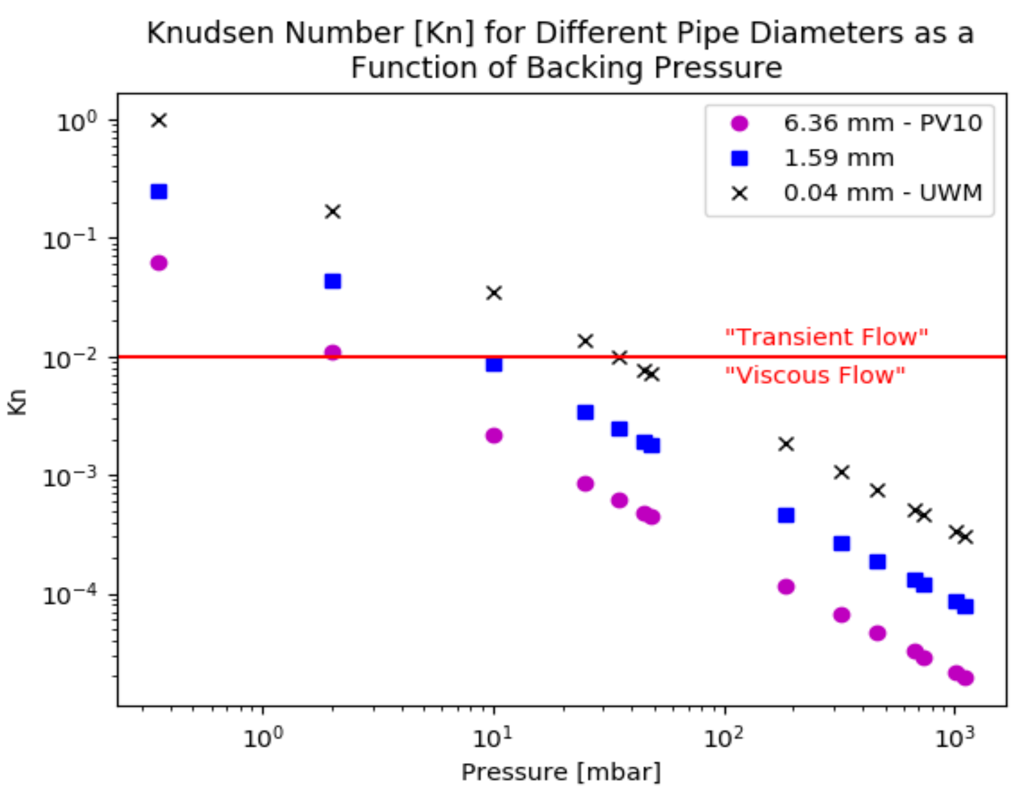

Figure 3.17. The effects of nozzle or pipe diameter, D_p, and backing pressure on Kn.

3.6 Hardware Summary

The results of this chapter are discussed, and the best gas injection system is chosen for subsequent HELIOS experiments in this thesis. The HELIOS gas puffers were shown to have the same order of magnitude of particles injected into the chamber as the fuel injectors, which implies that non-perturbing HELIOS measurements will be difficult to accomplish. The calculation of the time responses of the HELIOS piezos, section 3.3, determined that the 2 A driver from Table 3.1 was confirmed to supply the piezo with the fastest charging time; however since the Jenna 0.5 A system has a voltage range of -20 V to 130 V it was chosen as the current driver. The broader voltage range allows for more combinations of gas injection. This decision was further supported by the fact that for the PV-10, which has a smaller capacitance than the UW-M gas injection system, has a much faster charge time. The difference in response of the two drivers is minimal.

The UW-M gas injection system demonstrated an ability to inject consecutive gas puffs into the plasma column with enough time for background subtraction between each puff, but the PV-10, due to hardware constraints, demonstrated a single puff with a long fall off. The conductance values calculated in the final section explain this trend. The delayed response of signal and long fall can potentially be improved by modifying the PV-10 hardware. Furthermore, both gas injection system fall within the 'viscous flow' regime, meaning that they are characterized by wide angle dispersion. Ultimately, the PV-10 and the UW-M gas injection systems, at the outlet, will puff gas in the same way.

Due to the milestone driven research of Proto-MPEX, port allocation and vent time (time the machine is open to air for modifications) is limited. This fact also drove the choice of the gas injection system. Figure 3.18 shows the view of the plasma using the fVC at the location of the UW-M gas injection system. The nozzle from the UW-M gas injection system is recessed in the port to the right of this image outside of view. The cross-section near the helicon antenna was too small to insert the full puffer in vacuo, so it was mounted outside of the vacuum. The TZM nozzle also had to be protected from RF and a stainless steel shield was designed to mount around it. Due to the small port window, which offers a narrow field of view for the fVC, information pertaining to the gas puff was not visible. The PV-10 piezos were in greater quantity and had the ability to be modified so that gas could be puffed directly into the plasma column and, coupled with the fact that it has the fastest response it was chosen as the main gas injection system for this thesis. A PV-10 (6.5T) was modified and installed on a top port of the central chamber. The 6.5T gas injection system is shown in schematic form in the top image of Figure 3.19. The bottom image indicates where the 6.5T puffer is mounted on the central chamber's engineering drawing and the corresponding collection optics used for this puffer. The 6.5T was made by attaching a long pipe to a fresh PV-10 and feeding it through a quick connect on top of the central chamber. This allowed for the PV-10 outlet to be moved vertically up and down in the vacuum chamber and adjusted so that the outlet was periphery to the plasma column. The new location allowed for the HELIOS system to take advantage of the TS 24-chord optics, which are normal to the gas puff

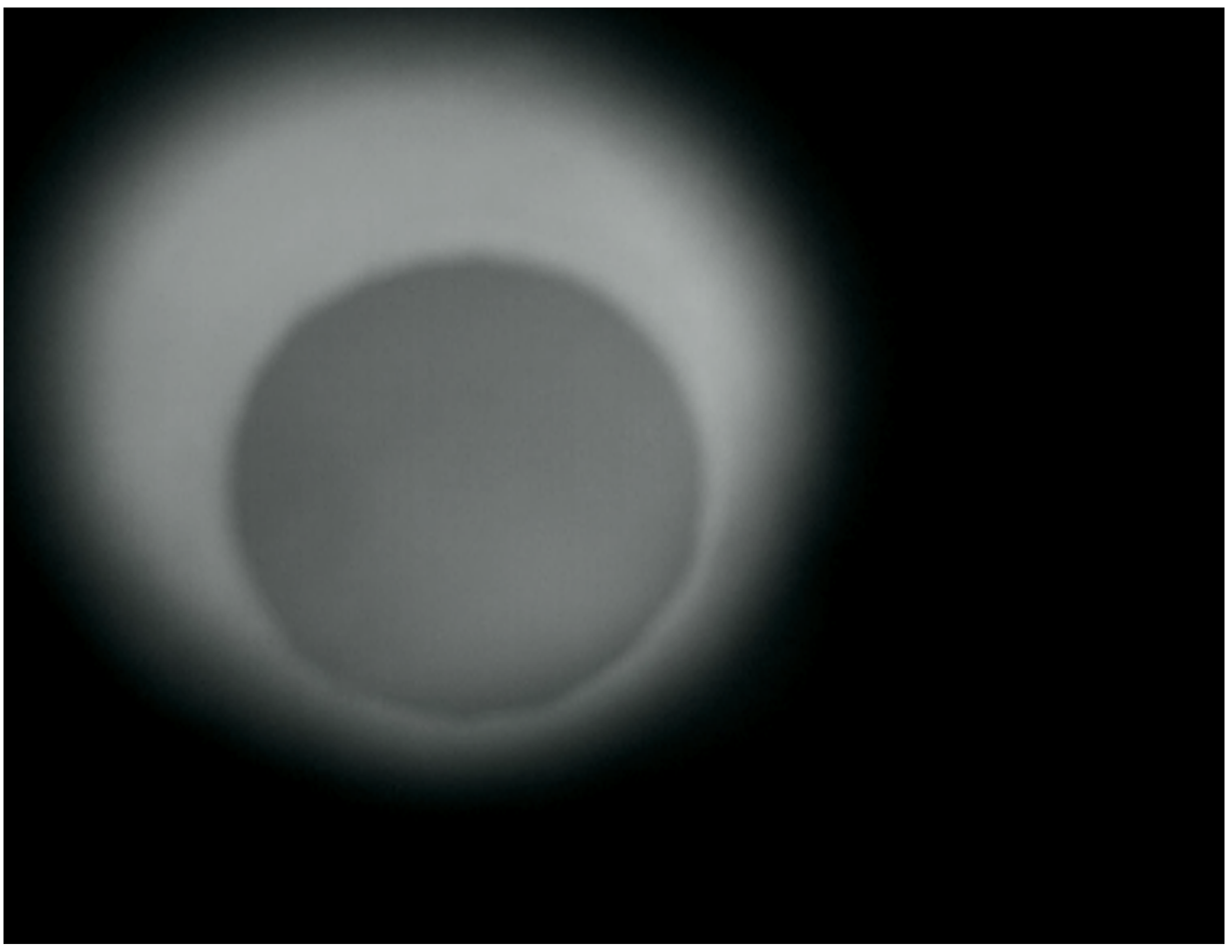

Figure 3.18 Port view using the fVC at the UW-M gas injection location

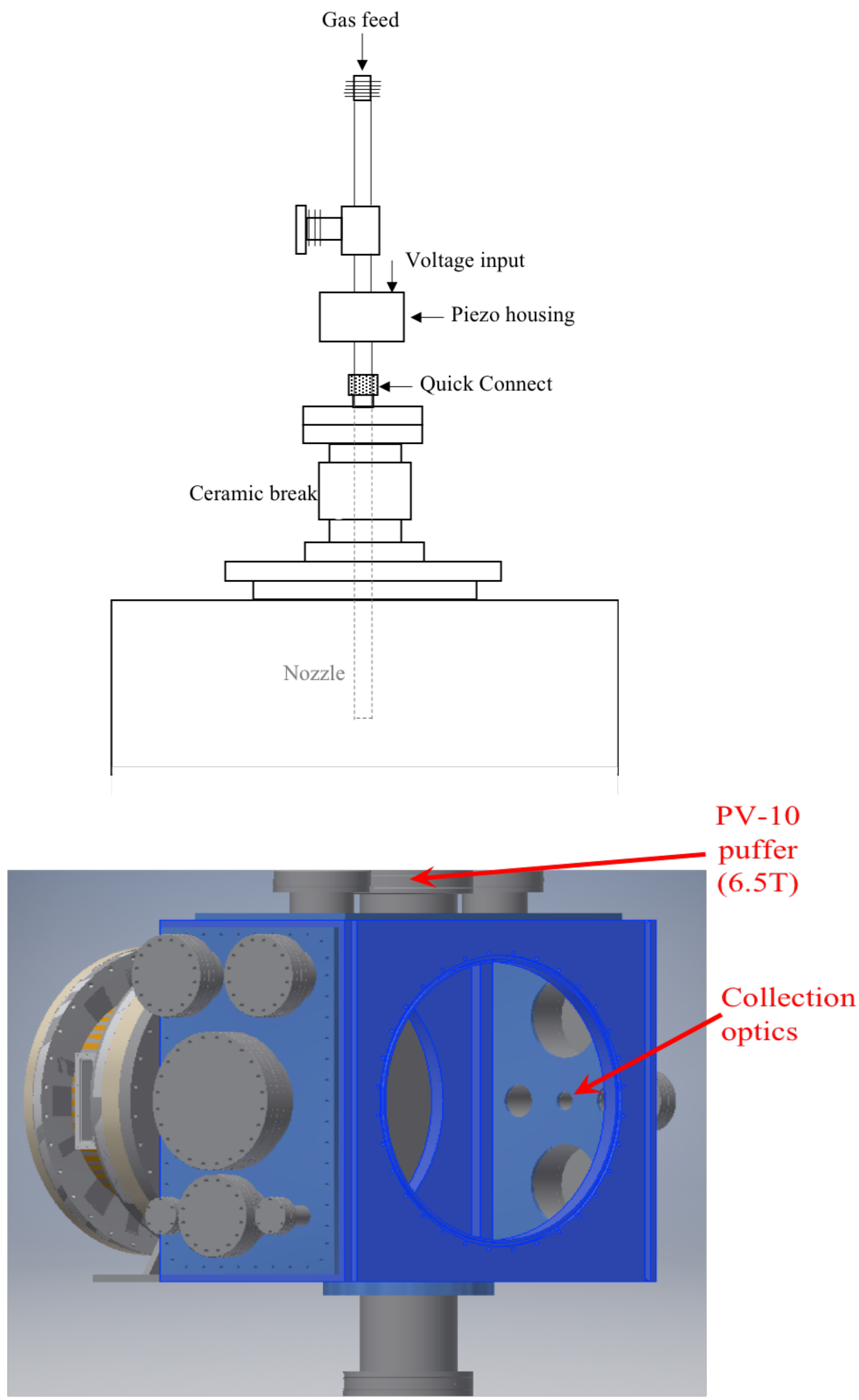

Figure 3.19. Scheamtic of PV-10 on top of the central chamber and the central chamber engineering drawing.

Chapter 4 The Measurement Systems

The helium line emission is collected by a compact OO collimating lens with a 4° collection cone that is normal to the gas puff in the plasma. The light is carried through a fiber optic to either a radiometer called the Filterscope or a Czerny Turner McPherson 2051 one-meter spectrometer. The Filterscope was developed by ORNL scientists[3] and is employed on several experimental plasma devices across the world, including TEXTOR, Proto-MPEX, DIII-D, the Tungsten Environment in Steady State Tokamak [WEST], the Korea Superconducting Tokamak Advanced Research [KSTAR], and Wendelstein 7-X [W7- X]. Spectrometers are commonly used for helium line ratio analysis due to their spectral resolution, so the McPherson spectrometer was used in tandem to the Filterscope for improved spectral resolution measurements. The fast Visible Cameras (fVC) are Sanstreak Corp. Edgertronic SC1.[65] Even though not used for T_e and n_e HELIOS measurements, the fVCs are valuable diagnostics to analyze and view the gas puff.

4.1 The Filterscope

The Filterscope consists of a series of photomultiplier tubes [PMTs] mounted in a compact and portable chassis with collimating lens and narrow bandpass filters. Figure 4.1 is an image of the Filterscope for Proto-MPEX at ORNL. The orange fibers, called patch fibers, connect the PMTs to the patch panel in the diagnostics room. On one side of the patch panel are all the transfer fibers, long fiber optics that connect the optics at Proto-MPEX to the diagnostic room. Patch fibers can be moved around on the patch panel to view emission from different locations on Proto-MPEX. There are twenty-four PMTs installed in the Filterscope, fifteen of these are used for axial D_α emission measurements, six are used for HELIOS measurements, and three are used for hydrogen Balmer series measurements. Beam splitters are visible in the right PMT module. These are three in-series cube-mounted pellicle beams splitters.[66] Emission from Proto-MPEX passes through the collimating lens attached to the beam splitters. For HELIOS the light passes through the $728.00 \pm 1\,nm$, $706.53 \pm 1\,nm$, and $667.9 \pm 3\,nm$, respectively. The Filterscope HELIOS setup is illustrated in Figure 4.2.

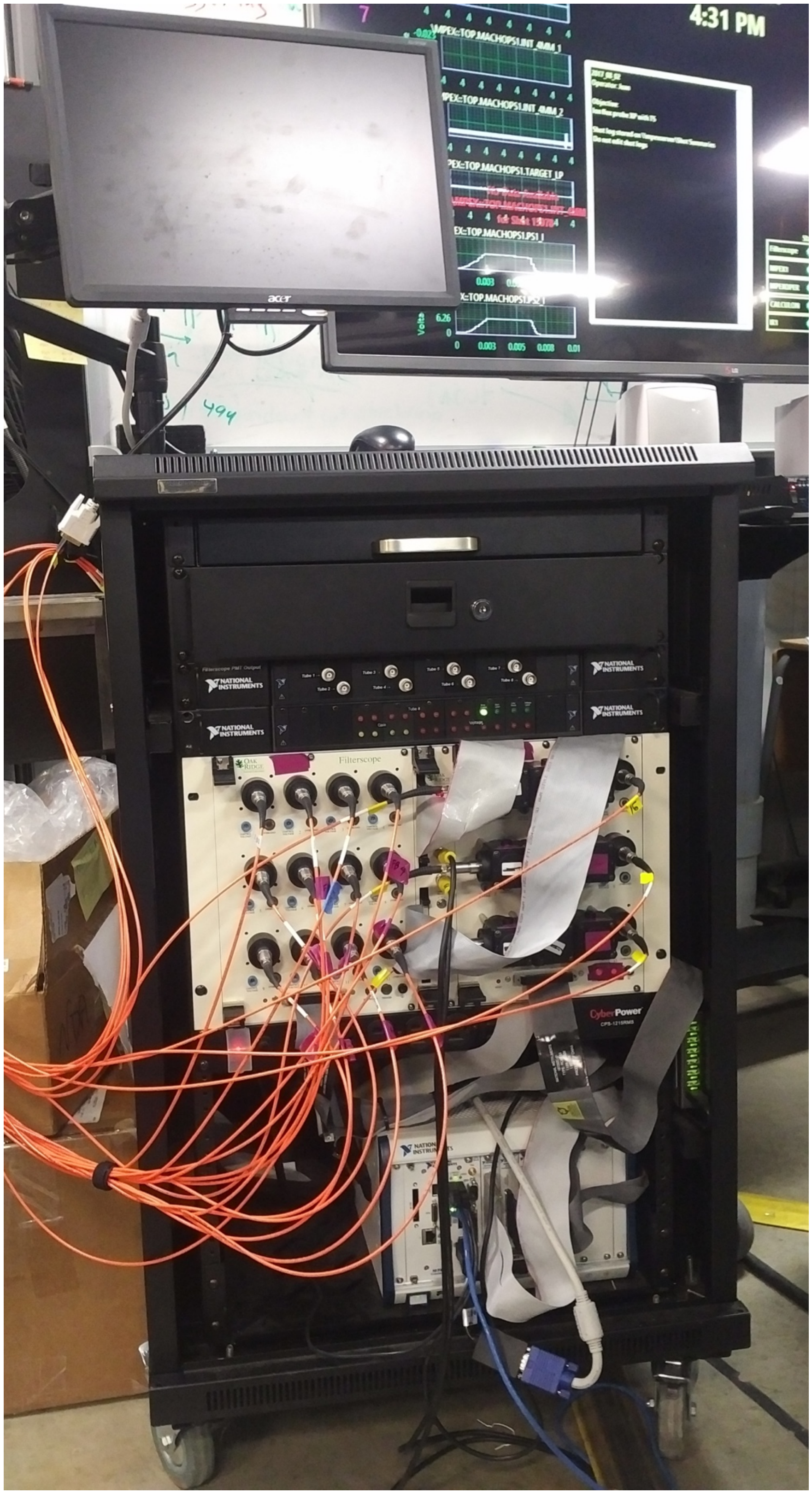

Figure 4.1. Proto-MPEX's Filterscope System

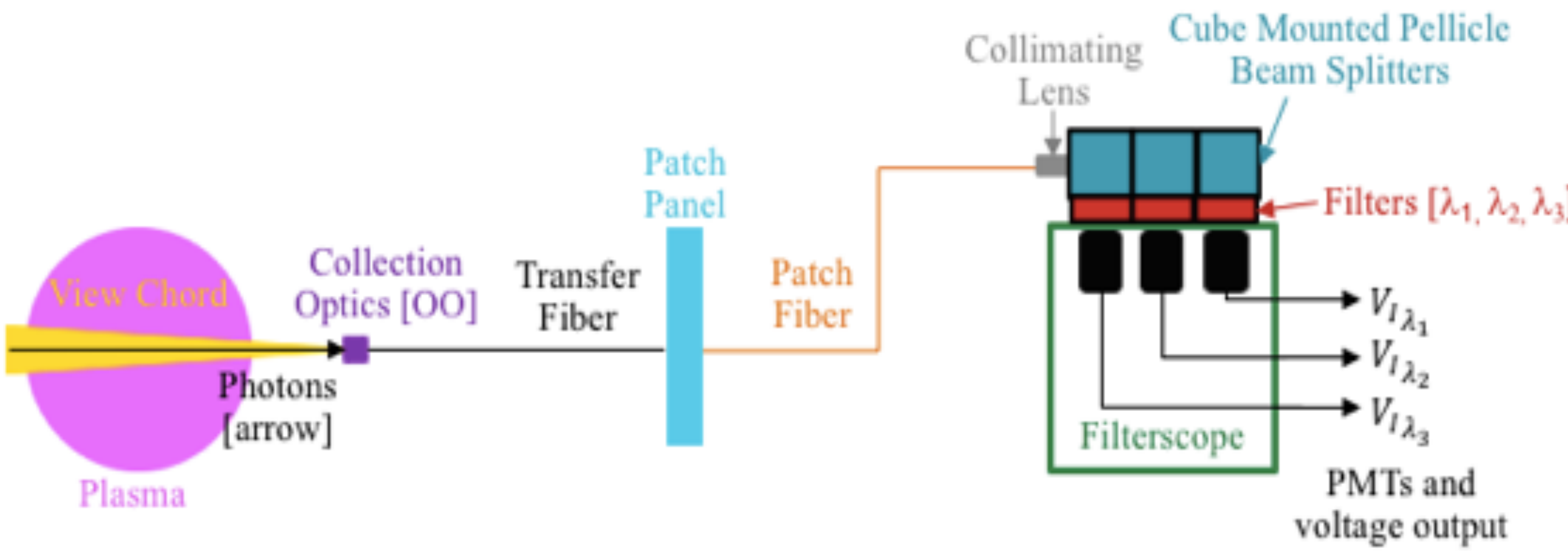

Figure 4.2. Optical emission spectroscopy for Proto-MPEX's HELIOS technique

Light carried from the experiment is directed through a collimating lens and a narrow-bandpass filter before passing into the PMT. A photocathode at the entrance of the PMT converts the incident light into a photoelectron. The photoelectron is multiplied by a series of dynodes or electron multipliers before terminating on an anode, outputting a current. A transimpedance integrated circuit converts this electrical current into a voltage before it is amplified by a control bias, V_{cont}, and saved to the local and facility computers. Figure 4.3 is an example of the raw Filterscope PMT signal for different control bias. The signals were taken during the same experimental day but for two different Proto-MPEX discharges.

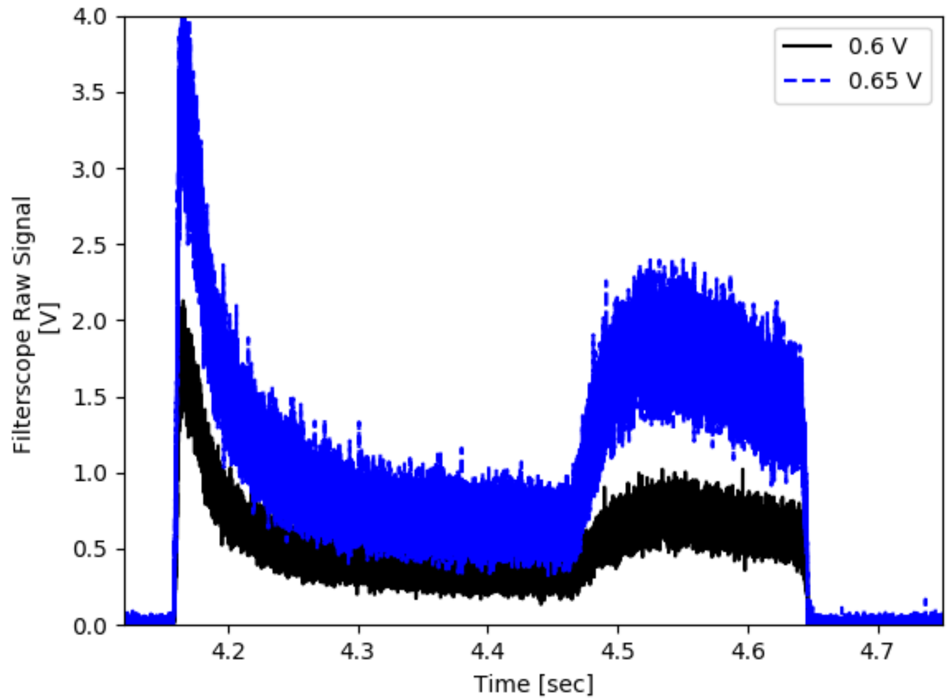

Figure 4.3. Example of the effect of the control bias for the Filterscope

High values of control bias allow for the Filterscope to measure lower levels of emission that are normally difficult to detect. Low values of control bias allow for the Filterscope to measure higher levels of emission without saturating the signal. Also, each PMT is slightly different and requires a different V_{cont} to effect high enough signals (> 1 V). Since multiple PMTs could have different values of V_{cont} a relative calibration needs to be performed in order to compare different PMTs. Figure 4.4, Figure 4.5, and Figure 4.6 are the fourth order polynomial fits for the relative gain calibration of the three PMTs (13: 728.00, 14: 706.53, and 15: 667.90) used for HELIOS measurements. The data for Figure 4.4. was collected using the Filterscope and a calibrated integrating sphere. A micrometer was used to open and close the shutter that separates the sphere from the light bulb, which allowed for the intensity in the sphere to be controlled (neutral density filters with a lamp are commonly used for this step). Table 4.1 contains the raw calibration data (V_{PMT}), intensity of the integrating sphere lamp, V_{cont} (tube voltage), and the processes performed on the raw calibration data to get the calibrated relative gain polynomial value, $k = A_4V_{cont}^4 + A_3V_{cont}^3 + A_2V_{cont}^2 + A_1V_{cont} + A_0$.[10]

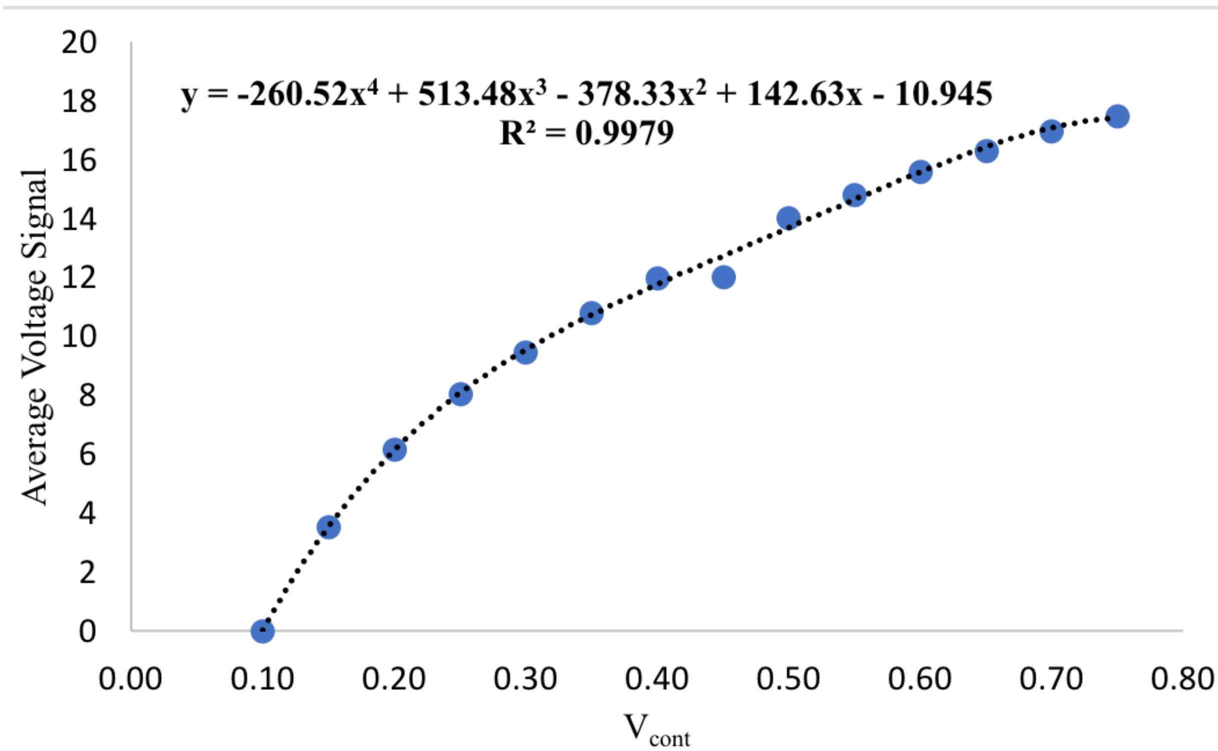

Figure 4.4. Relative Gain Calibration for PMT 13

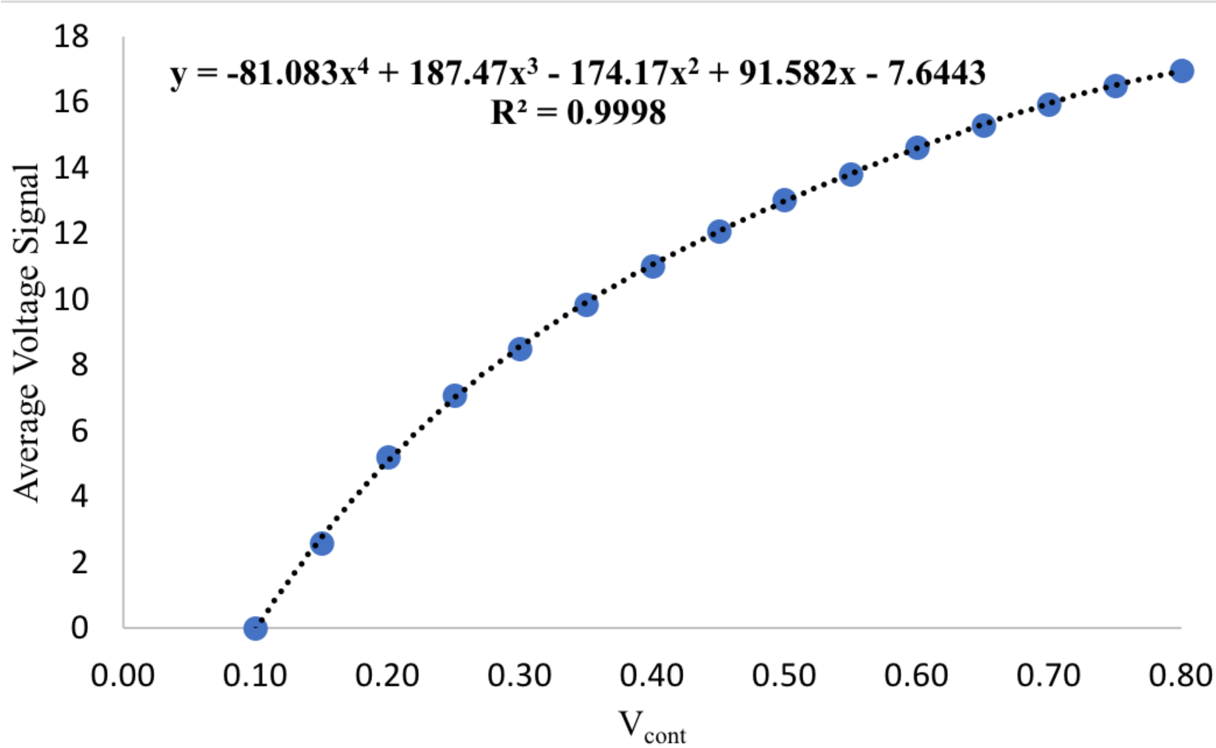

Figure 4.5. Relative Gain Calibration for PMT 14.

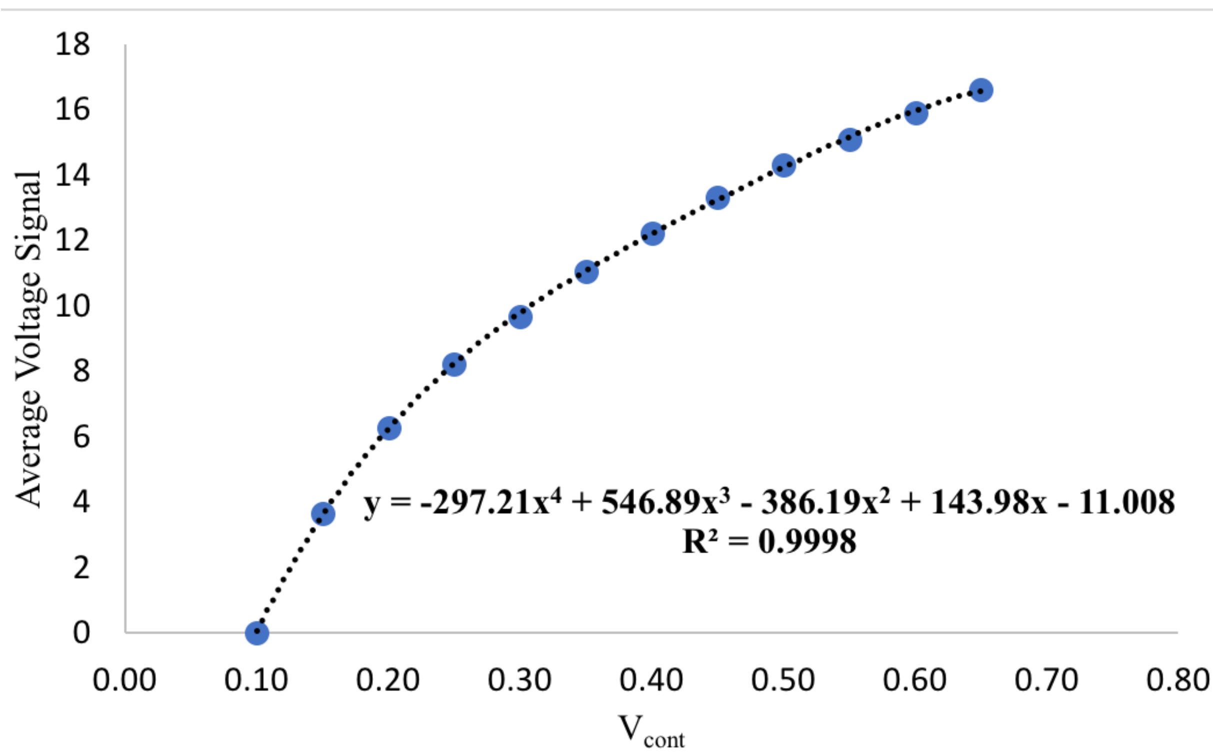

Figure 4.6. Relative Gain Calibration for PMT 15.

TABLE 4.1. RELATIVE GAIN CALIBRATION FOR TUBE 13.						
Tube Voltage	**Intensity [ft-L]**	**Tube Signal**	**Zero Subtract**	**Normalized Luminance**	**G_{PMT}**	**k**
0.00	8511	-1.11E-03	0.00E+00	0.00E+00	0.00E+00	0.00E+00
0.05	8511	5.26E-04	1.64E-03	1.92E-07	7.98E+01	4.38E+00
0.10	8511	-1.13E-03	2.05E-05	2.41E-09	1.00E+00	0.00E+00
0.15	8511	-3.90E-04	7.20E-04	8.46E-08	3.51E+01	3.56E+00
0.20	8511	8.72E-03	9.83E-03	1.15E-06	4.80E+02	6.17E+00
0.25	8511	6.37E-02	6.48E-02	7.61E-06	3.16E+03	8.06E+00
0.30	8511	2.69E-01	2.70E-01	3.18E-05	1.32E+04	9.49E+00
0.35	8511	1.04E+00	1.04E+00	1.22E-04	5.06E+04	1.08E+01
0.40	8511	3.32E+00	3.33E+00	3.91E-04	1.62E+05	1.20E+01
0.45	8511	3.44E+00	3.44E+00	4.04E-04	1.68E+05	1.20E+01
0.50	2143	6.48E+00	6.48E+00	3.02E-03	1.25E+06	1.40E+01
0.55	51	3.40E-01	3.41E-01	6.69E-03	2.78E+06	1.48E+01
0.60	51	7.47E-01	7.48E-01	1.47E-02	6.09E+06	1.56E+01
0.65	51	1.51E+00	1.51E+00	2.96E-02	1.23E+07	1.63E+01
0.70	51	2.87E+00	2.87E+00	5.63E-02	2.34E+07	1.70E+01
0.75	51	4.90E+00	4.90E+00	9.61E-02	3.99E+07	1.75E+01
0.80	--	--	--	--	--	--

First, the V_{PMT} at $V_{cont} = 0.0\ V$ was subtracted off of the V_{PMT} for non-zero V_{cont}. This is the background if no bias voltage was applied to the PMT. Since an integrating sphere with variable intensity was used to measure V_{PMT} the signals had to be normalized to the integrating sphere's luminance. This meant that each of the V_{PMT} values were divided by their respective intensity value (Normalized Luminance). For each PMT there is a minimum V_{cont} value that is a baseline, i.e. the point at which the bias on the PMT is just beginning to affect the output signal. For the calibration in Table 4.1 the baseline is $V_{cont} = 0.01\ V$. The baseline is used to normalize the signal into G_{PMT}. G_{PMT} is the current amplification in the PMT and is proportional to $\frac{V_{PMT}}{V_{PMT\ MIN}}$, meaning that for the baseline $G_{PMT} = 1.0$.[10] The relationship between G_{PMT} and k is given in equation 4.1.1 and is used to calculate the k values in Table 4.1.

$$G_{PMT} = e^{k} \qquad Equation\ 4.1.1$$

This value is special to the PMT and typically only needs to be performed once; however, due to aging of electronics performing gain calibrations every couple of years is recommended.

In order for the Filterscope signals to be used for HELIOS they must be absolutely calibrated, too. The Filterscope outputs a voltage signal that is proportional to the number of photons collected by the optics at the experiment. The absolute calibration, represented by equation 4.1.2, is necessary for the Filterscope and is known as the responsivity of the diagnostic, $\mathcal{R}$.

$$\mathcal{R} = \frac{1}{V_{cal}} I_{INH} \quad \left[\frac{Photons}{s * sr * cm^2 * V}\right] \qquad Equation\ 4.1.2$$

For the Filterscope this includes the transmission loss from the collection optic to the PMT (V_{cal}) and the transmission of the narrow bandpass filter for the chosen wavelength or the total radiance for a given filter transmission (I_{INH}). The absolute calibration involves the same integrating sphere used in the relative gain calibration. The integrating sphere is mounted at Proto-MPEX and the transmission fibers and optics are directed to view the emission from the sphere. For each PMT a signal is collected by the Filterscope that includes the calibration voltage, V_{cal}, and its respective calibration bias voltage, $V_{cont\ cal}$. The V_{cal} value is typically maintained between 2 – 5 V. I_{INH}, or the inherent number, is calculated by using the measured bandpass filter transmission fraction, multiplying it by the calibrated integrating sphere spectral radiance

($\frac{W}{sr*cm^2*nm}$), and integrating under the curve. For the calculation of I_{INH} in this document the spectral radiance units (integrating sphere curve (blue) in the top image of Figure 4.7) were converted to ($\frac{Photons}{sr*s*cm^2*nm}$). The top plot shows the one-inch filter's transmission fraction curve (red) and the spectral radiance curve from the integrating sphere (blue). The bottom plot (magenta) is the product of the spectral radiance (blue) and the filter's transmission fraction (red). This curve represents the amount of calibrated light that passes through the filter for each wavelength. The hatched shaded region means to integrate the under curve to get I_{INH}.

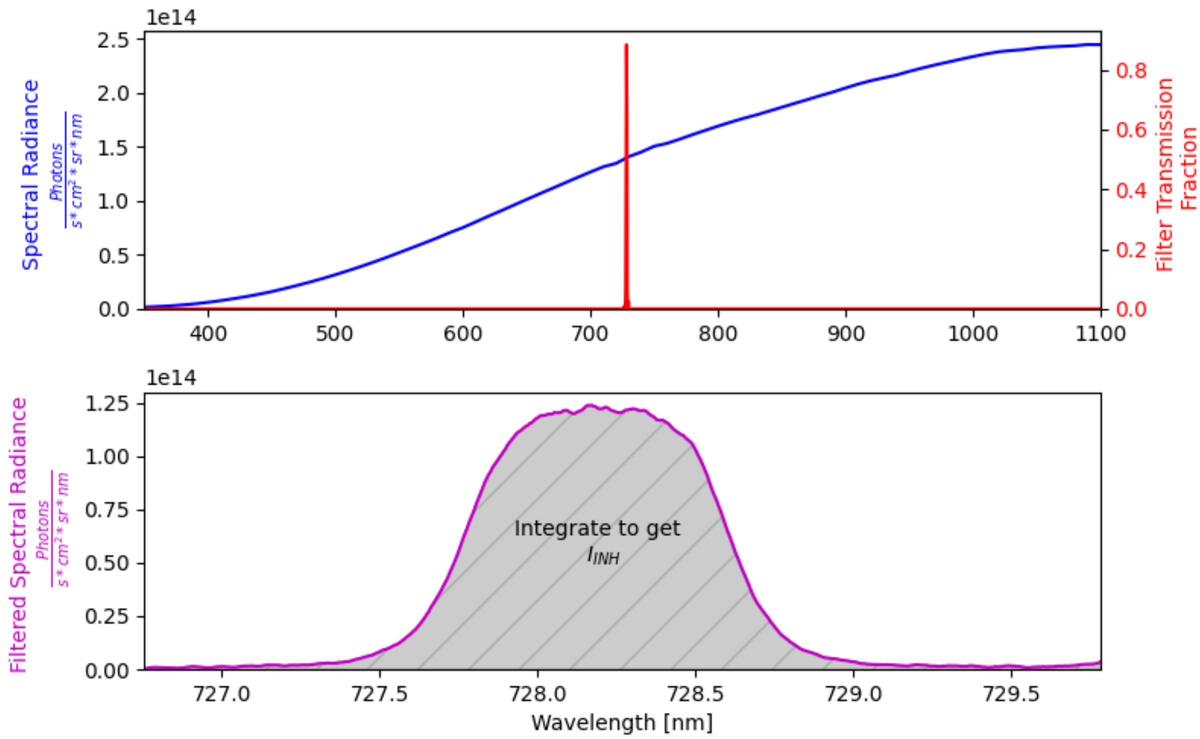

Figure 4.7. Process of Calculating the Inherent Number using the Calibrated Integrating Sphere.

$V_{cont\ cal}$ is used to calculate G_{Cal}, by calculating $k = A_4V_{cont\ cal}^4 + A_3V_{cont\ cal}^3 + A_2V_{cont\ cal}^2 + A_1V_{cont\ cal} + A_0$. This value divided by G_{Exp} is how the bias voltage per PMT is accounted for in the calibration. G_{Exp} is calculated the same way as G_{cal}, but instead of using $V_{cont\ cal}$ the bias voltage used for the experiment (the raw signal bias voltage), V_{Exp}, is used to calculate k. Ultimately, the Filterscope calibration returns two multipliers, $\mathcal{R}$ and $\frac{G_{cal}}{G_{Exp}}$, that convert the raw voltage signal, V_{PMT}, in to a photon flux (Φ_λ) of units $\frac{Photons}{s*sr*cm^2}$. Due to the fact that the ratios are being taken for HELIOS the Φ_λ as a function of the solid angle and area of the collection chord will suffice.

Equation 2.5.1 is the final calibration equation of the raw Filterscope data, V_{PMT}, for HELIOS. The intensity of the filtered light measured by the Filterscope, $I_\lambda = \Phi_\lambda A\Omega$, is determined from calculating the Φ_λ, using the relative gain calibration, $\frac{G_{Cal}}{G_{PMT}}$, and the absolute responsivity of the system, $\mathcal{R}$, as described previously. A is the area of the collection optics and Ω is the solid angle.

$$\Phi_\lambda = V_{PMT}\frac{G_{Cal}}{G_{Exp}}\mathcal{R} \quad \left[\frac{Photons}{s*cm^2*sr}\right] \qquad Equation\ 2.5.1$$

4.2 The McPherson

The Czerny Turner McPherson spectrometer (roughly two-meter by one-meter) sits on an optics table in the diagnostics room. It contains a pop-in grating for quick swaps for different spectrum widths (bandpass) and a mechanical gear drive that rotates the grating in order to measure different regions of the visible spectrum. A specially designed fiber interface was made so that the McPherson could view the emission from up to five locations, selected at the patch panel. The McPherson setup is similar to Figure 4.2 except that the image to the right of the patch panel is replaced with five fibers leading to the McPherson spectrometer. Light emission is directed from Proto-MPEX, through the five McPherson fibers, and onto mirrors that direct the light onto the grating. The light is then directed by mirrors into a Princeton Instruments charged coupled device (CCD) camera. Software known as WinSpec is used to control the CCD camera. For measurements made on Proto-MPEX for HELIOS the CCD camera measures 512 points along the spectrum for each of the five fibers at a digitization rate of 40 Hz and a 300 grooves/mm grating was chosen. The McPherson grating is programed to be centered at 682 nm for the 667.9 nm line and 721 nm for the 706.53 and 728 nm lines. A slit width of 20 μm is set. Figure 4.9 is an image of the McPherson spectrometer in the diagnostics lab.

The calibration of the McPherson requires measuring the wavelength dispersion between the 512 pixels in the spectrum and having the absolute intensity calibration. In order to measure the

wavelength dispersion, a calibration lamp (preferably neon because it has serval known wavelengths in a single spectrum), is setup so that a single fiber can collect light from the lamp. A single spectrum is collected that has several peaks shown with known wavelengths. Each of these known wavelengths corresponds to a pixel; therefore, the known wavelengths can be plotted as a function of the pixels and fit with a polynomial. Using the polynomial fit one can determine the wavelength space between each pixel, $\Delta\lambda$. If the center wavelength is known, then $\Delta\lambda$ can be used to determine the wavelength of any spectrum measured by the McPherson.
The absolute calibration was performed with the same integrating sphere from the previous section. For the HELIOS calibrations the integrating sphere was mounted on the optics table in the diagnostics room and a single spectrum was collected for each of the five fibers at each of the center wavelength grating settings (682 nm and 721 nm). Figure 4.8 has two images; the top image is the raw counts from the McPherson during the integrating sphere calibration and the bottom plot is the integrating sphere calibration curve divided by the counts in the top plot. The periodic structure in the signals is an aged characteristic of the CCD camera used.

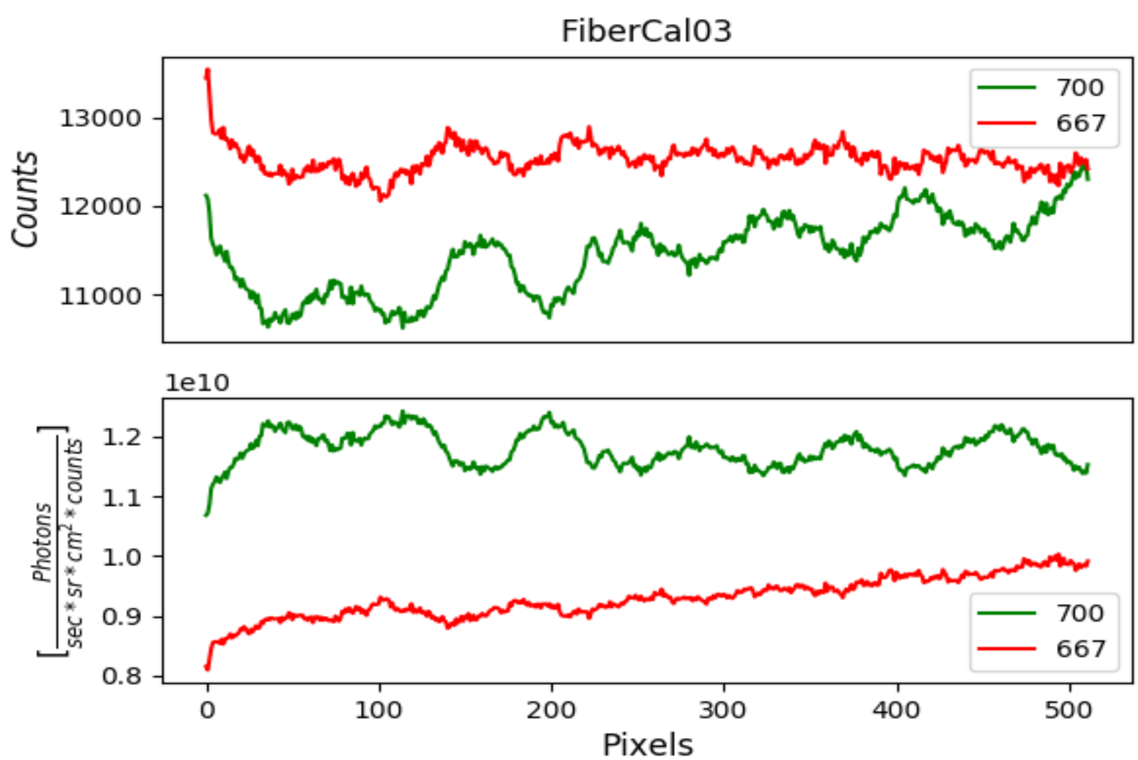

Figure 4.8. Calibration Spectrum for HELIOS tuned at 721 nm (700) and 682 nm (667).

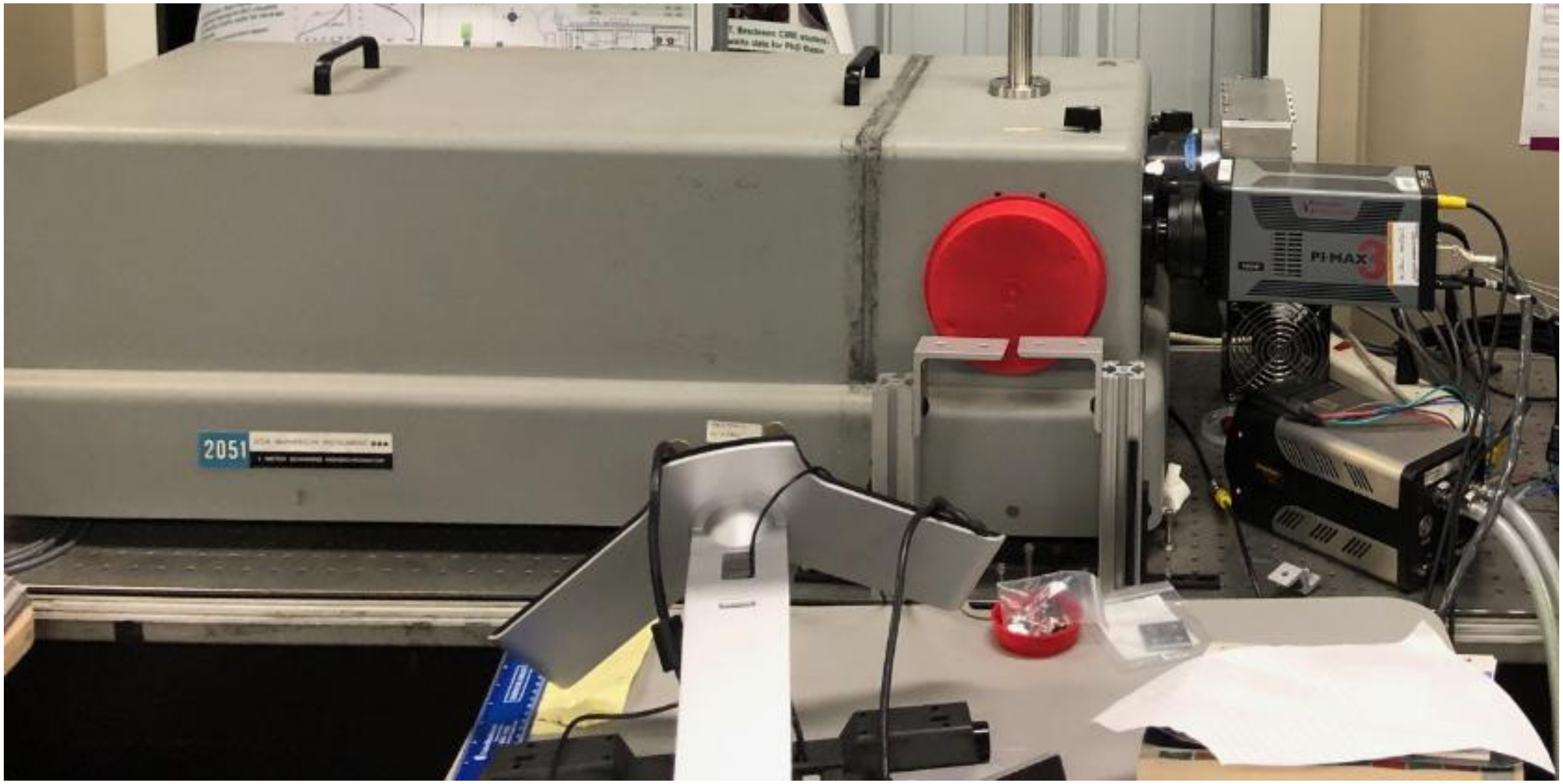

Figure 4.9. The McPherson Spectrometer.

Figure 4.8 is the calibration for a single fiber (labelled fiber 03). Both images show the calibration for the 721 nm center wavelength setting (700) and the 682 nm center wavelength setting. The raw signals (top image in Figure 4.10) are multiplied by their respective calibration curves (bottom image in Figure 4.8) to return the calibrated spectra for the 667.90, 706.53, and 728.00 nm emission lines (bottom image in Figure 4.10). Since the ratios of the lines are being taken for a single fiber the transmission loss calibration from the machine to the McPherson will be divided out; therefore, it was not necessary to calibrate the transmission from Proto-MPEX for HELIOS.

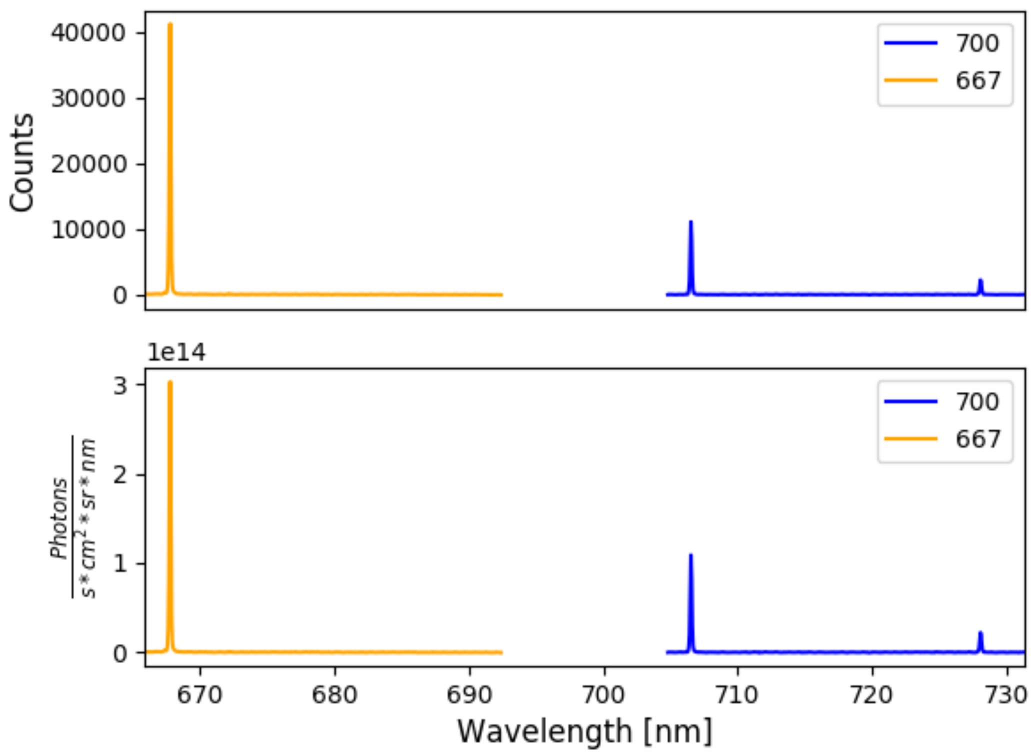

Figure 4.10. Raw and calibrated spectrum of the three HELIOS lines.

4.3 The fast Visible Cameras

Proto-MPEX has one polychrome and two monochrome fast visible cameras (fVC). They are Sanstreak Edgertronic SC1s, and have 8 GB memory. Each camera can operate at up to 18 kHz frame rate with a resolution of 192x96. A maximum resolution of 1280x1024 can be obtained with a frame rate of 500 Hz. The tradeoff between resolution and frame rate is extremely important because it allows for the cameras to be utilized for separate purposes. With a higher frame rate, the cameras can resolve more images within the span of a plasma pulse. But the higher resolution allows the camera to view a larger area of the plasma column or chamber. The cameras are easily mounted to the windows on Proto-MPEX and are great diagnostics for 2D emission image analysis. Using two-inch filter adapters, two-inch filters can be attached to the front of the lens, allowing for the cameras to observe specific wavelength emission from Proto-MPEX Figure 4.11 is an image of one of the SC1 fVCs[65].

Figure 4.11. SC1 fast Visible Sanstreak Edgertronic Camera.[65]

The fVCs require pixel calibration, filter calibration, and an absolute calibration. Pixel calibration involves checking the relative intensity of each pixel. The relative intensity calibration can be done by taking an image of the emission from a white light source with the maximum resolution (1280x1024) setting. Normalizing the image to the highest pixel intensity results in a multiplier, M_{Rel}, that should be applied to all pixels for pixel-to-pixel comparisons. A simple way to determine spatial calibration is to use the same maximum resolution and take an image of a ruler both in the width and length direction. Using the ruler in the image one can determine the physical size scale of the image (7.00x5.57 cm). Since the pixels are small squares that make up the image either the length or the width can be divided by its respective resolution length or width. A single pixel scales to the length of $5.40 \times 10^{-3}\ cm$. The filter calibration is similar to that in section 4.1 with the exception that the two-inch filters tend to have a larger bandpass around, ± 10 to $\pm 20\ nm$. The camera will also have a 2D matrix, M_{INH}, consisting of I_{INH} values for a specific two-inch filter. M is used to represent a matrix of data. Figure 4.12 is an image of the I_{INH} calibration with a $710 \pm 20\ nm$ two-inch filter. The bandpass is clearly larger than the bandpass in Figure 4.7.

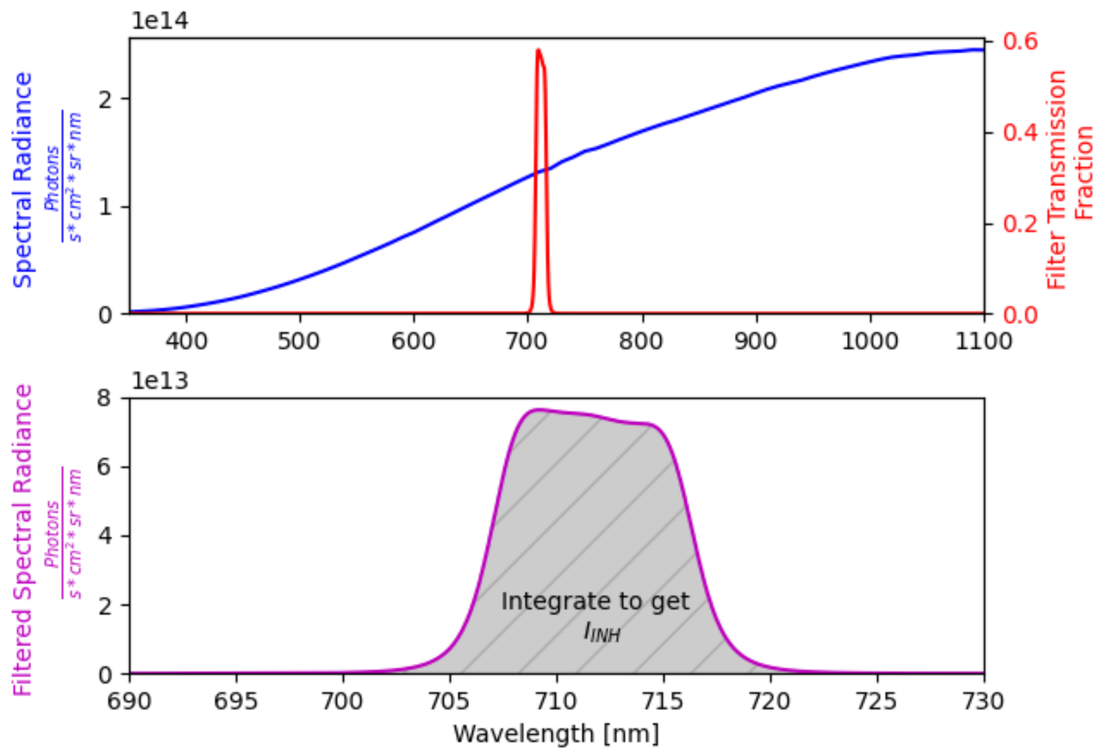

Figure 4.12. Process of Calculating the Inherent Number using the Calibrated Integrating Sphere.

Once again, the integrating sphere is used to absolutely calibrate the cameras. Since the cameras are mounted directly to the windows on Proto-MPEX the cameras are placed directly in front of the integrating sphere. A single frame at maximum resolution is taken with each camera,

M_{cal}. Equation 4.3.1 is used to measure the calibration multiplier, M_{Multi}, which is used to convert raw data, M_{Exp}, from an experiment into Φ_{λ}.

$$M_{Multi} = \frac{M_{INH}}{M_{Cal}} M_{Rel} \qquad Equation\ 4.3.1$$

$$M_{\Phi_{\lambda}} = M_{Exp} * M_{Multi} \qquad Equation\ 4.3.2$$

4.4 Summary of Measurement Systems

This chapter has detailed the different measurement systems (Filterscope, McPherson, and fast Visible Cameras (fVC)) used in HELIOS measurements of T_e and n_e and gas puff analysis. For each system the respective calibration processed is described. The following chapter will go into the HELIOS validation experiment, using the Filterscope for measurements of T_e and n_e and the fVC for gas puff analysis. Chapter 6 will describe the McPherson analysis process used for the gas puff experiment.

Chapter 5 Validation Analysis

Once the HELIOS hardware had been installed it was necessary to test and validate the diagnostic. Testing the technique ensures that all components are working as expected. Important factors of the diagnostic to test include bandpass impurities and calibrations. Testing for bandpass impurities ensures that there are no polluting lines in the one-inch filters on the Filterscope. This includes measuring the bandpass of the one-inch filters and then measuring, during a helium puff, the McPherson spectra from the plasma. Testing the calibrations ensures that the intensity data measured and used for HELIOS analysis is correct. The best way to test the calibrations is by validating the HELIOS diagnostic measurements against measurements made by double Langmuir probes (DLP) and Thomson Scattering (TS). Validating against other measurements is necessary for confidence in HELIOS. In the following sub-sections, the one-inch bandpass filters on the filterscope are checked for any polluting lines, the data analysis process of the measured HELIOS data is outlined, the HELIOS data from the central chamber is compared to TS and DLP measurements, and the results from the gas penetration experiment (GPE) are detailed and discussed.

Figure 5.1 is a modified version of Figure 3.1 that includes the path of the TS laser as a solid green line with an arrow to demonstrate direction. TS on Proto-MPEX has multi-pass capability as shown by the green line passing through the target region plasma prior to passing through the central chamber plasma where HELIOS measurements are made. The PV-10 gas puffer, TS collection optics, DLP location, and helicon antenna are pointed out using colored arrows and names. HELIOS measurements are made using separate collection optics at the central chamber and later with the TS optics for the GPE. The central chamber PV-10 puffer is the main puffer in this analysis due to the complications that arise when measuring T_e and n_e with a DLP at the location of the UW-M gas puffer. There is also no available TS at that location and the results from Chapter 3 detailed that the PV-10 piezo was the best choice for the Proto-MPEX HELIOS. The analysis presented in this section is aimed at measuring helium emission within an established CRM regime to assess that HELIOS can be used to measure T_e and n_e in Proto-MPEX. Further experimental results are discussed in section 5.5, following the results found for the validation comparison between the DLP and TS from Section 5.3.

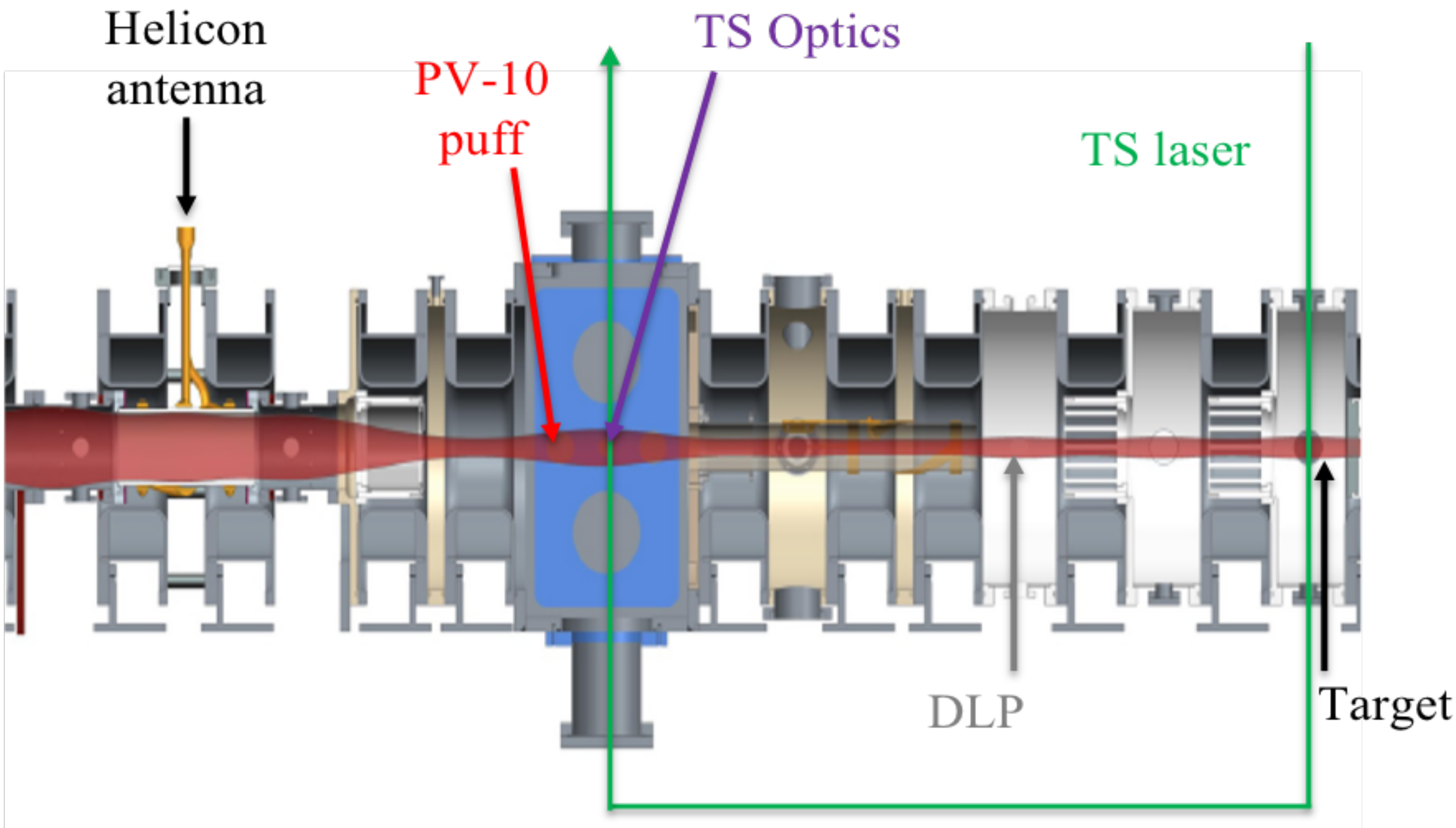

Figure 5.1. Axial cross-section of Proto-MPEX from when preliminary HELIOS data was taken

5.1 Impurities Emission Lines in the One-Inch Filters

As discussed in the previous chapter the signal returned by the Filterscope is not spectrally resolved. If there are emission lines that fall within the bandpass of the one-inch filters used, then the HELIOS measurement will be polluted and not reliable. The presence of peaks in the one-inch filter's bandpass increases the signal by including intensity of the other polluting lines. In order to check if there are any emission lines within the one-inch filters: the bandpass of the one-inch filters was measured, and a scan of the plasma during a gas puff was performed. The scan showed what emission lines are present in the plasma other than the He I transitions: $3^1D \rightarrow 2^1P$ (667 nm), $3^3S \rightarrow 2^3P$ (706 nm), and $2^1P \rightarrow 3^1S$ (728 nm).

The McPherson 2051 one-meter spectrometer, described in the previous chapter, was used to measure the normalized shape of the bandpass of each of the one-inch He I filters, $\zeta_{McPherson}$. Emission from a white halogen lamp was directed through the filter and into the McPherson, B_{filter}. Measurements were also made with the filter without light (B_{filter_back}), without the filter with light ($B_{McPherson}$), and without the filter without light (B_{filter_back}). The McPherson measures a 3 nm range (1800 grooves/mm diffraction grating) so the 667.9 $\pm$ 3 nm filter needed three stitched McPherson acquisitions before capturing the full bandpass. The fractional filter transmission, $T_{\frac{1}{100}}$, is calculated using equation 5.1.1 and the normalized shape of the one-inch bandpass filters, $\zeta_{McPherson}$, is calculated using equation 5.1.2. The normalized shape of the one-inch bandpass filters is displayed in Figure 5.2, Figure 5.3, and Figure 5.4 as the red-dotted trace for each of the three He I lines.

$$T_{\frac{1}{100}} = \left(\frac{B_{filter} - B_{filter\_back}}{B_{McPherson} - B_{McP\_back}}\right) \qquad Equation\ 5.1.1$$

$$\zeta_{McPherson} = \frac{T_{\frac{1}{100}}}{Max\left(T_{\frac{1}{100}}\right)} \qquad Equation\ 5.1.2$$

For the plasma scan, the McPherson was tuned to each of the He I lines and used to measure the emission spectrum from Proto-MPEX during a helium gas puff. The McPherson line of sight was placed in the same location that the HELIOS line of sight would be collecting data. Three plasma shots were required for the 667.9 nm line in order to capture the full spectrum under the bandpass curve. The normalized emission spectrum from the plasma scan during a gas puff is represented by the blue curves in Figure 5.2, Figure 5.3, and Figure 5.4. The McPherson data confirms that there are no impurity lines in the bandpass of the one-inch filters used in the Filterscope and also shows that the 3 nm bandpass of the 667.9 nm filter is small enough to avoid the very bright D_α line, which is absent from Figure 5.2.

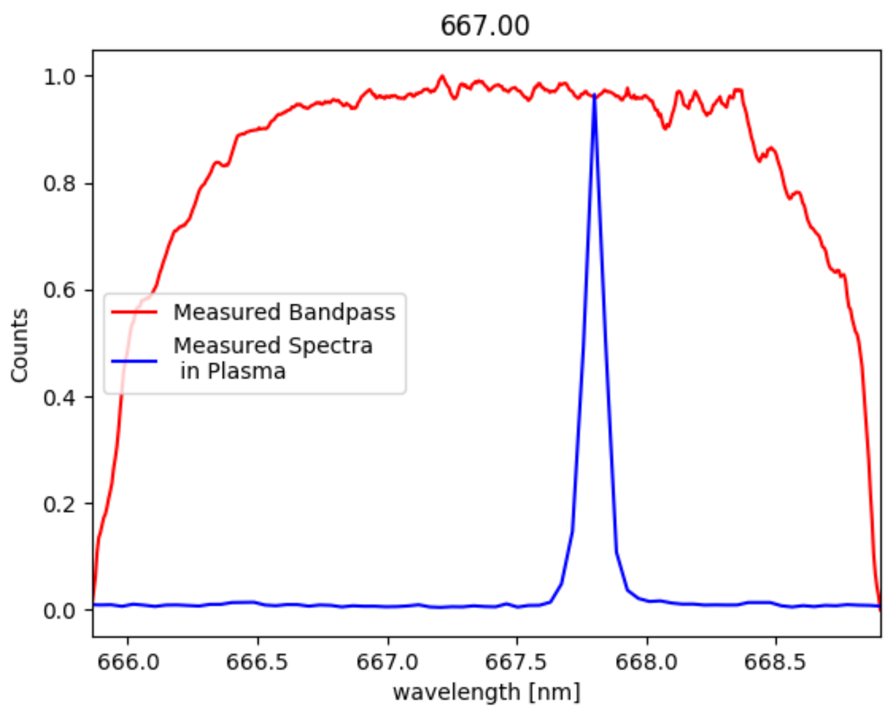

Figure 5.2. Impurity check of the 667.90 ± 3 nm narrow bandpass filters.

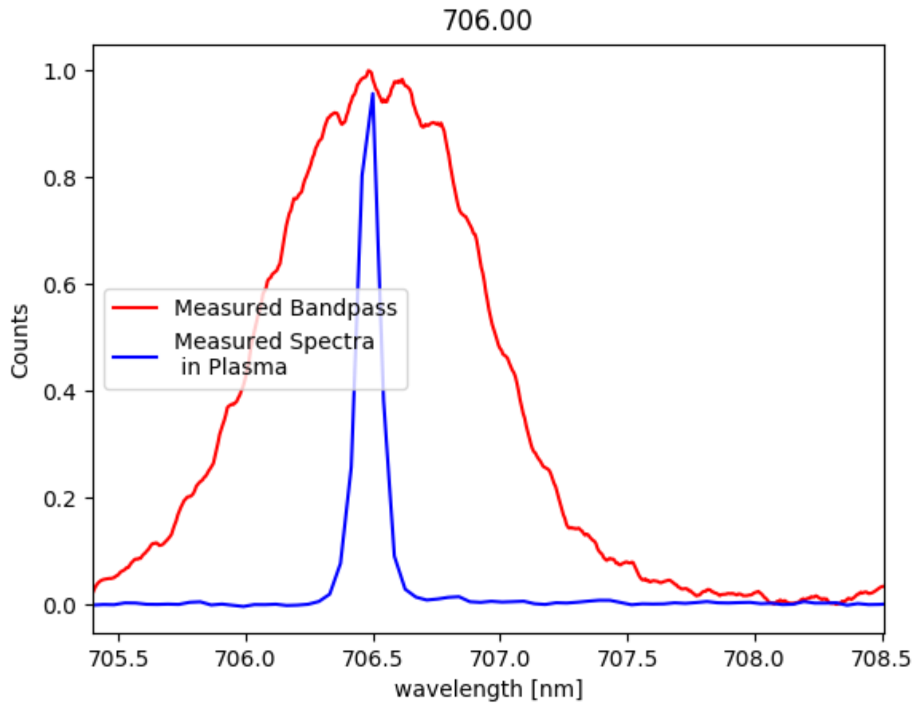

Figure 5.3. Impurity check of the 706.53 ± 1 nm narrow bandpass filters.

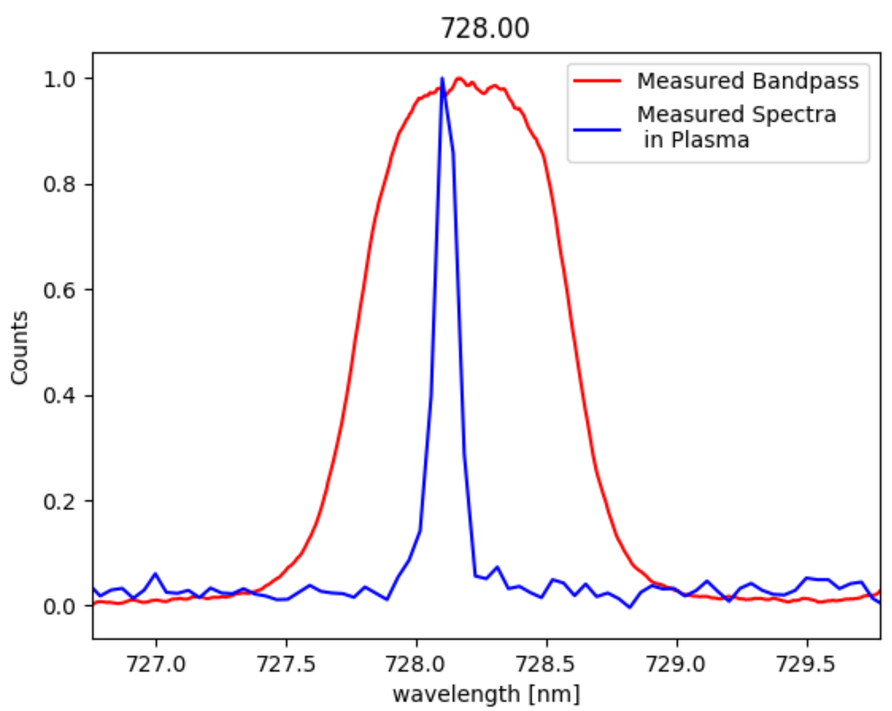

Figure 5.4. Impurity check of the 728.00 ± 1 nm narrow bandpass filters.

5.2 Analysis Process

The calibrated Filterscope data discussed in the previous Chapter for the three different He I lines (728.0 nm, 706.53 nm, and 667.9 nm) is displayed in the top figure of Figure 5.6 and the T_e dependent ratio, $R_{T_e} = \frac{I_{706.53}}{I_{728.0}}$, and n_e dependent ratio, $R_{n_e} = \frac{I_{667.9}}{I_{728.0}}$, calculated from the calibrated measured intensities are displayed in the bottom plot. The Filterscope's high digitization rate (100 kHz) allows for the HELIOS derived T_e and n_e to be temporally resolved in the plasma pulse. The data in Figure 5.6 are 10 ms averaged windows (1000 data points) of the original data. Figure 5.6 shows the ratios calculated from the measured helium intensities for the plasma parameters found in Proto-MPEX. The CRM is used to calculate spectral line intensities for specified values of electron temperature and density. These are used to calculate the model ratios, which are displayed in the contour plot in Figure 5.5. The red solid trace is R_{T_e} and the blue dashed lines are R_{n_e}. T_e and n_e are derived from the abscissa and ordinate of the contour plot at the point which the ratios, determined by the experiment, intersect.

Figure 5.7 are the inferred values of T_e and n_e for the ratios shown in Figure 5.6. The figure showing the HELIOS measured values of T_e and n_e demonstrates an interesting trend. Over the time of the gas puff the ratios appear to be fairly constant with little to no fluctuations; however, the T_e and n_e plot show a clear trend in the measured values. If this trend matches the temporal trend in another diagnostic it will support the time response of the Filterscope HELIOS diagnostic. Figure 5.8 suppress the error bars in the data so that one can clearly see the time response of both diagnostics. The HELIOS measurement trends follow similar trends in the DLP data. This indicates that the HELIOS diagnostic using the 100 kHz filterscope can resolve temporal changes in the plasma parameters. Lowering the sample size would increase the number of points over time allowing the Filterscope HELIOS to resolve more temporal information. The plots also show how sensitive the diagnostic is to the helium puff. Over the time of the gas puff the ratios increase slightly, which is barely visible in Figure 5.6. A pulsed gas puff, shown in Chapter 3, have several square pulse signals within the longer pulse time width and allows for better background subtraction for any helium build up. The longer gas puff of helium allows for a better temporal resolution of the plasma and is used in this thesis. This thesis shows that the gas puffing scenario is a preference for Proto-MPEX plasmas.

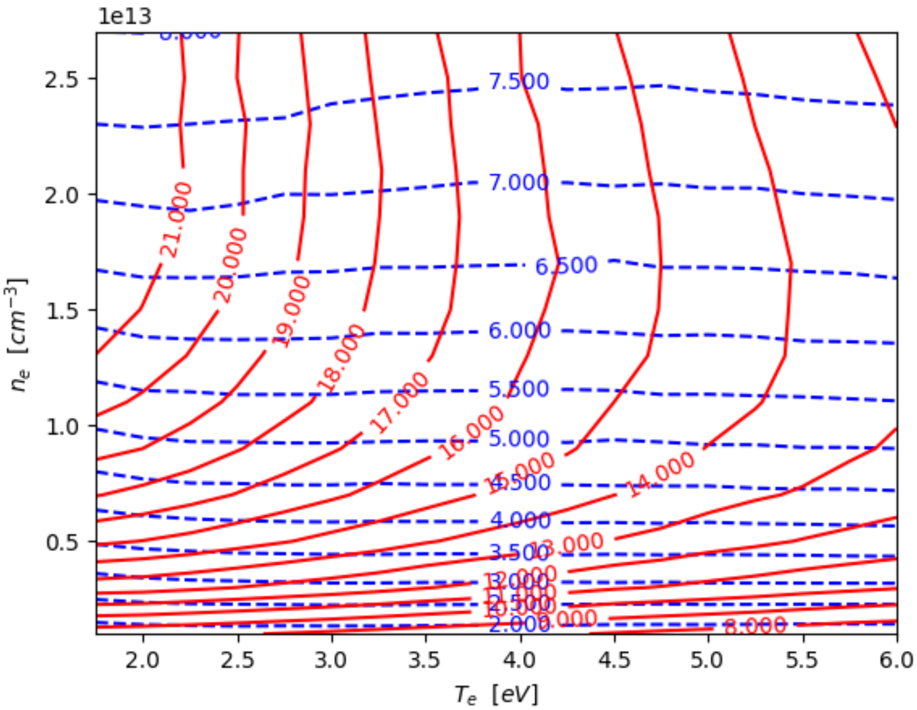

Figure 5.5. Contour plot of Te and ne dependent ratios from the ORNL CRM

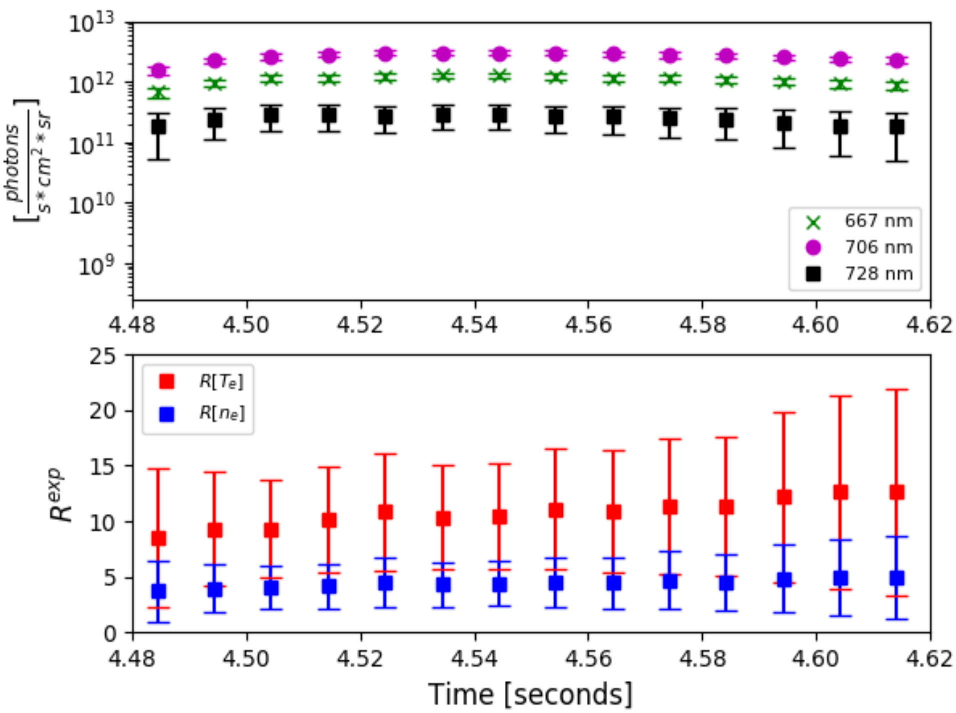

Figure 5.6. Calibrated He I line intensities measured by the Filterscope and T_e and n_e dependent ratios.

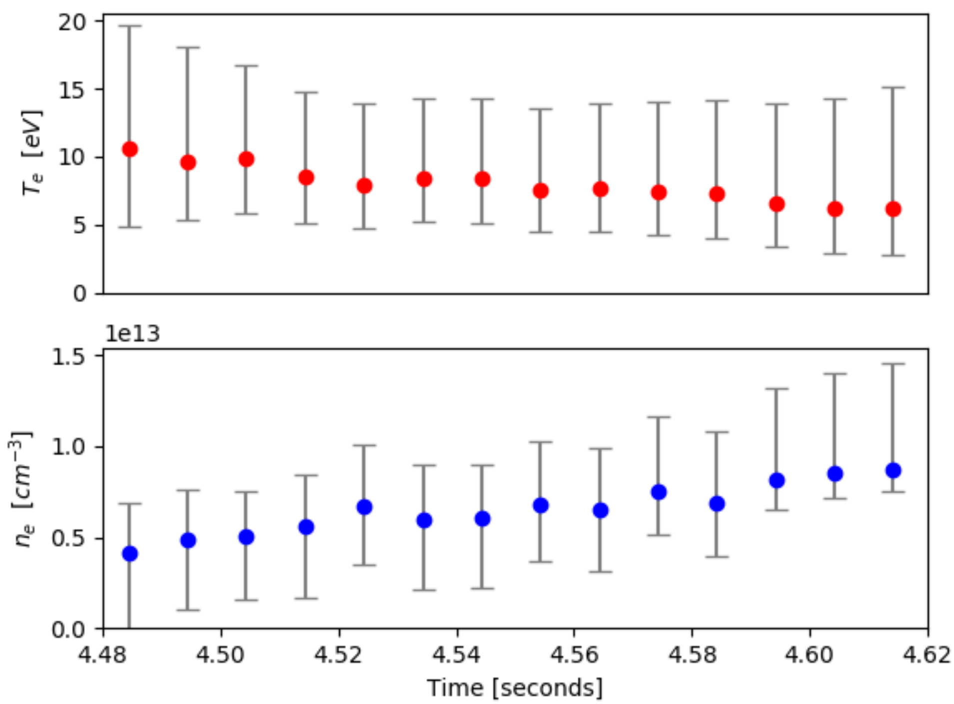

Figure 5.7. HELIOS Measured T_e and n_e.

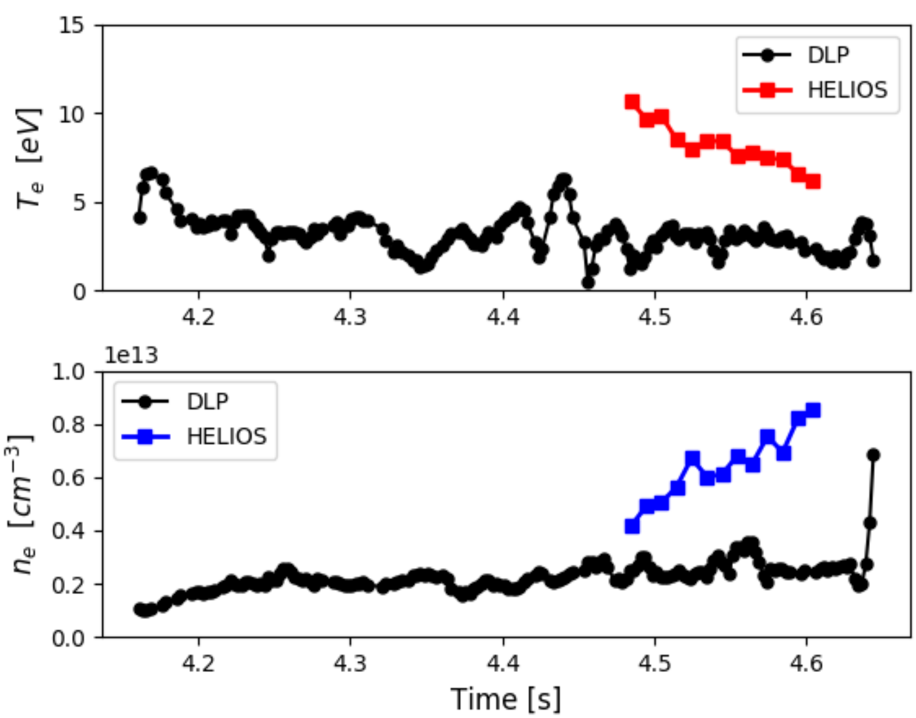

Figure 5.8 HELIOS Te and ne compared to DLP Te and ne exposing the temporal comparison

5.3 HELIOS compared to TS and DLP

To properly validate HELIOS as a capable diagnostic on Proto-MPEX the T_e and n_e inferred values need to be compared to another diagnostic's measurement of T_e and n_e. Therefore, during HELIOS operations TS and DLP measurements were taken. At the time of this experiment there was no capability to use a DLP at the central chamber to make comparisons with; however, there was a DLP downstream, indicated by a grey arrow in Figure 5.1, of the HELIOS location that will be used for edge measurement analysis. Data was taken during a deuterium discharge.

TS measured values of T_e and n_e at the central chamber are show in Figure 5.9 along with the HELIOS measurements of T_e and n_e. HELIOS measurements are displayed as a single solid bar across all radii due to line integration. The black dotted vertical line represents the radial location of the LFS. TS values to the right of this line, speculated to be due to low plasma density past the LFS, have poor gaussian fits at the radial locations 2.97 cm, 2.31 cm, and 1.98 cm and are excluded from Figure 5.9.

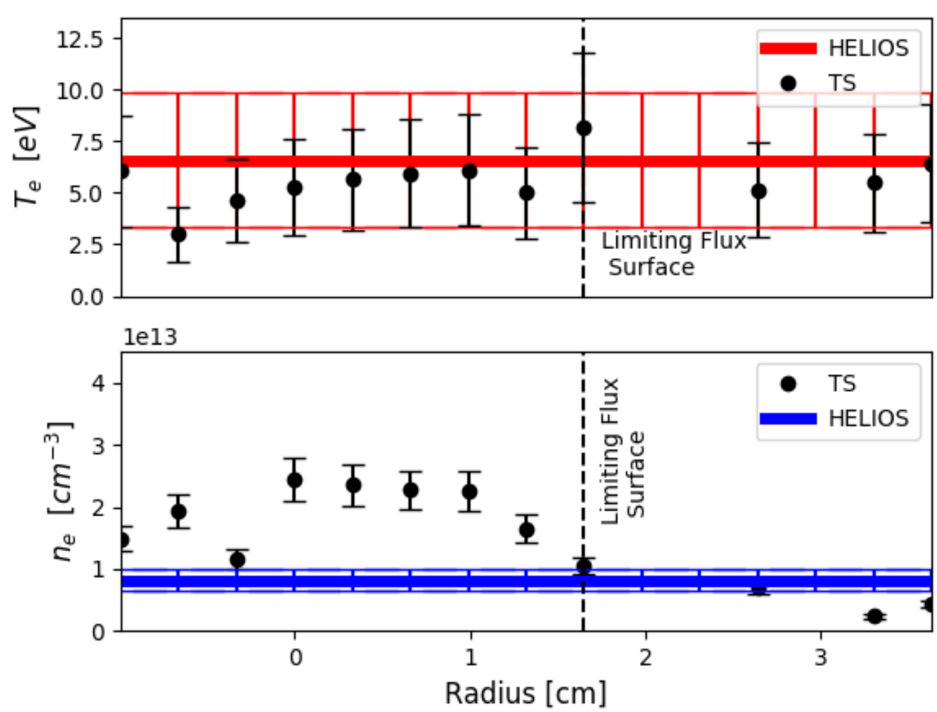

Figure 5.9. HELIOS derived T_e and n_e values compared to TS measured T_e and n_e values at the central chamber.

TS at the central chamber of Proto-MPEX reports T_e values from 3 eV to 8 eV and are displayed in the top graph of Figure 5.9. T_e measurements in Proto-MPEX tend to stay fairly uniform radially across the plasma column, showing that the inferred temperature measurements from HELIOS are consistent with the T_e from TS. This is confirmed by the consistency of the HELIOS T_e measurements with the TS T_e measurements. The density values across the plasma radius show a gradient between the plasma edge and the plasma core. This makes it difficult to resolve measurements from line-integrated HELIOS. The bottom graph in Figure 5.9 compares the HELIOS n_e measurements, blue bar that spans all radii, and the TS n_e measurement, black circular markers. There is a clear agreement between the edge TS measurement (r = 2.64 cm, 3.3 cm, and 3.63 cm) and the line-integrated HELIOS, implying that the light emission is localized to the plasma edge.

This observation prompted a DLP experiment where the tip was pulled back to the edge of the plasma column, $r_p = 2.25\ cm$. The DLP used in this experiment is located at the spool directly prior to the target location (Figure 5.1). The standard deviation of the average edge TS and DLP T_e and n_e measurements are calculated ($\sigma_{T_e} = 2.6\ eV$ and $\sigma_{n_e} = 2.10e12\ cm^{-3}$) and used as a variance margin between the DLP location and the HELIOS location. The DLP is measuring a point location in the plasma and HELIOS, due to its line integrated signal, is measuring over all radii. The DLP is inserted into the plasma column from the bottom of Proto-MPEX, whereas, the collection optics view the plasma horizontally. This will lead to discrepancies between the two measurements that cannot be accounted for in previously described variance.

Figure 5.10 shows the results for the DLP edge experiment with HELIOS. The top graph is the T_e measurements and the bottom graph is the n_e measurements. The plasma parameters, T_e and n_e, downstream of the HELIOS location for a helicon only plasma have been shown to be lower than the central chamber.[67] Figure 5.10 demonstrates this trend and shows that HELIOS measured T_e and n_e fall within a reasonable margin of the variances. The comparison between HELIOS measured T_e and n_e and DLP edge measured T_e and n_e supports the conclusion that HELIOS is measuring the edge plasma parameters.

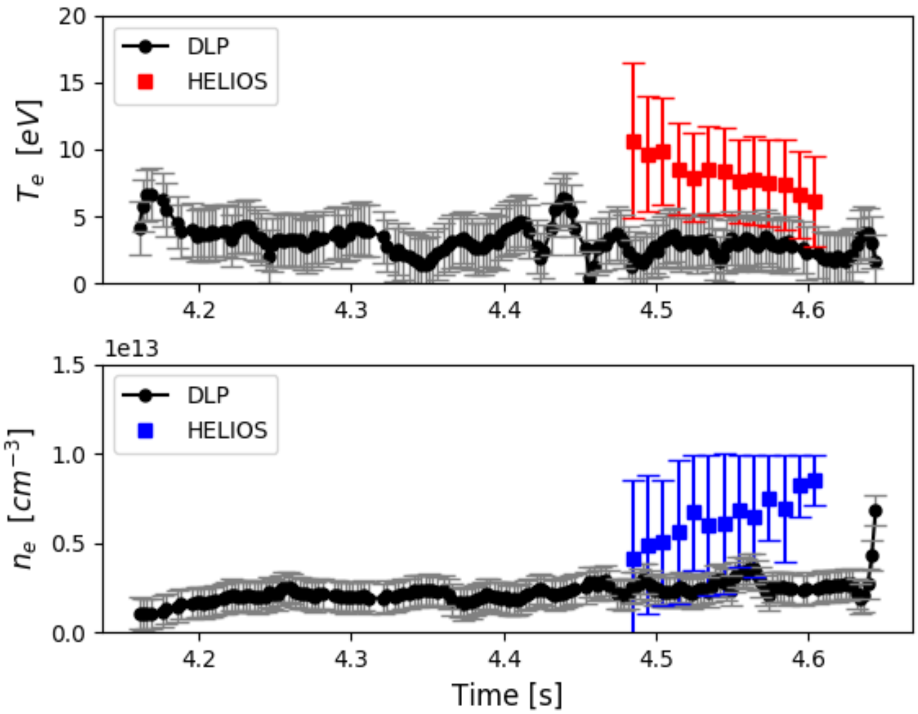

Figure 5.10. HELIOS derived T_e and n_e values as a function of time compared to DLP edge measurements as a function of time.

The data shown thus far in this chapter has been from the gas injection system installed at the central chamber in Proto-MPEX (Figure 5.1). The HELIOS system with the UW-M gas injection system adjacent to the helicon antenna has also been used to make measurements. HELIOS was installed here with the goal of making non-perturbative measurements of T_e and n_e along the radius of the plasma at the source. The measurements made at the central chamber were partially motivated by inconsistent measurements of T_e and n_e with the DLP measurements at the helicon location. After analyzing the data at the central chamber and understanding that the measurements were edge localized the data collected adjacent to the helicon antenna was revisited. The black markers in Figure 5.11 is a DLP radial scan from the location adjacent to the helicon antenna (Figure 5.12) and the red and blue bars are the HELIOS measurements made at the same location. Similar to Figure 5.9 the line integrated HELIOS n_e measurements show a strong comparison to the edge measured DLP data at $r_P > 5\ cm$. An important trend shown in Figure 5.11 is the edge relationship between the T_e measured values, which was not previously clear in Figure 5.9. This further supports the conclusion that the HELIOS measurements are edge localized.

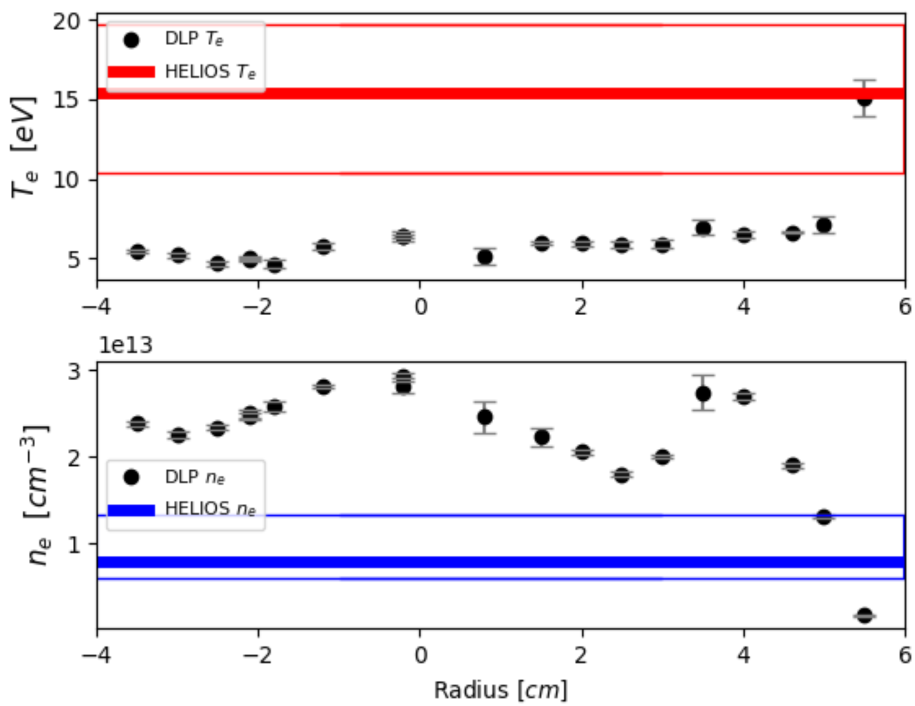

Figure 5.11. DLP Measurements of T_e and n_e compared to HELIOS Measurements Adjacent to the Helicon Antenna

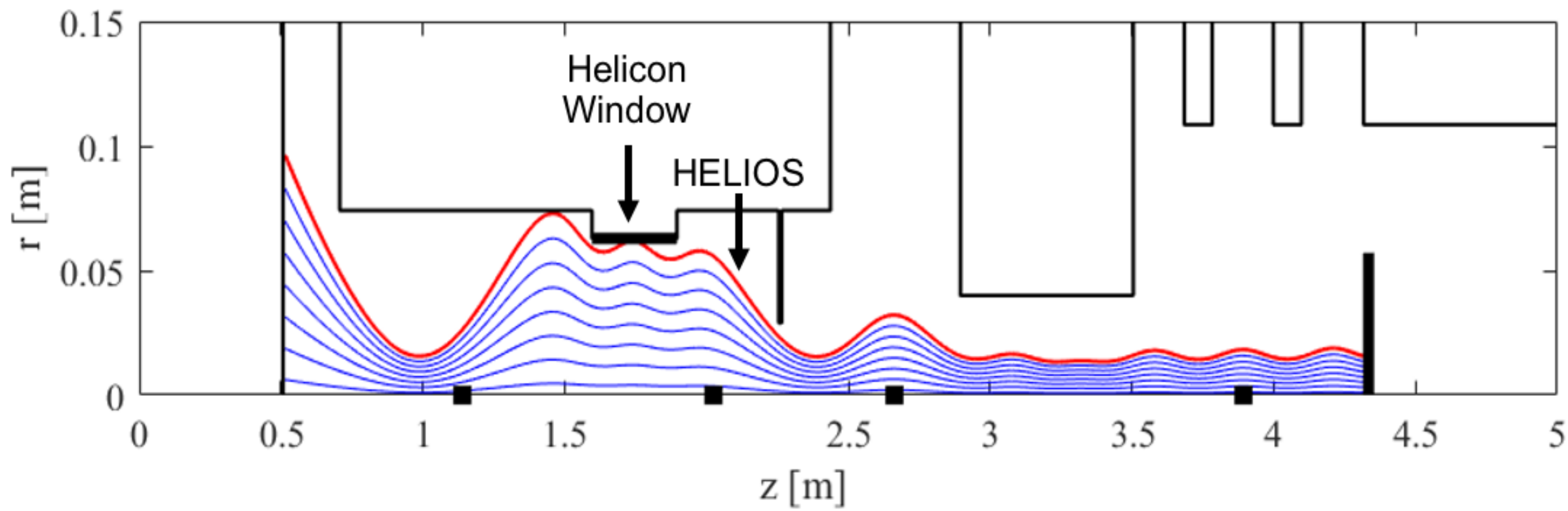

Figure 5.12 Plasma radius mapping (red line is the LFS).

This section of the chapter has shown data analysis from the DLP, TS, and central chamber HELIOS that supports the hypothesis that the measurements made by HELIOS were from the plasma edge rather than the plasma core. Revisiting data from the UW-M puffer, adjacent to the helicon antenna, further supports this conclusion. The data from the UW-M gas puffer as compared to DLP data not only showed consistency between the edge n_e measurements but also the edge consistency between the T_e measurements. This data supports that HELIOS is measuring edge values of T_e and n_e. The following section will explore the implication of edge localization by viewing and analyzing videos collected by the fVC.

5.4 Visual Analysis of Gas Puff and Discussion

From section 5.1 in this chapter it is clear that there are no impurities in the He I lines considered (I_{667}, I_{706}, and I_{728}) in this study, making them viable options for HELIOS on Proto-MPEX. Moreover, the results presented in section 5.3 of this chapter make a strong case that the HELIOS diagnostic on Proto-MPEX is measuring the edge plasma parameters, supporting that the gas is not penetrating past the plasm edge to the high-density core. Measuring T_e and n_e at the plasma core ($n_e > 2e13\ cm^{-3}$ and $T_e < 10\ eV$) in a linear deuterium plasma with the gas injection HELIOS diagnostic would be a novel accomplishment. HELIOS, to date, has been employed on the large toroidal devices and linear devices with a helium discharge, but by making HELIOS applicable for linear devices with a deuterium discharge an alternative option to DLPs and TS can be realized. In this section of Chapter 5 a discussion of the visual inspection of the plasma column during a gas puff will be made followed by a conclusion on HELIOS emission measurement location. Discussion of important design modifications made to the PV-10 gas injection system and collection optics is had, and the penetration physics of the gas puff is explained.

In order to view the gas puff a polychrome fVC was mounted normal to the gas puff on an external window viewing into the central chamber. The fVC was directed so that it could view the center of the plasma column and capture the gas injection and the penetration into the plasma. Figure 5.13 has two images from the video recorded by the fVC with a two inch, $710 \pm 10\ nm$, bandpass filter attached. The images are from before (bottom) and during (top) the gas puff at the central chamber in a helicon only plasma on Proto-MPEX. The backing pressure in the HELIOS gas plenum was 1117 mbar. Unfortunately, the gas puff is not distinctly visible, nor does it appear to penetrate into the plasma core. This observation is informative in two ways: 1.) the gas puff is not collimated and is dispersed in the vacuum chamber either due to low outlet velocity or plasma flow, and 2.) the lack of penetration into the plasma core further supports that the results shown in the previous section were from the plasma edge.

The first point is consistent with the calculations made in Chapter 2 that determined the flow regime to be viscous, having a high gas divergence of 120° at the outlet of the nozzle. The images show the brightness from the puff spread out across the plasma column as opposed to collimated across the radius. The gas puff nozzle outlet is not captured in the images due to the distance from the plasma edge; however, it is located at the bottom outside of the images and puffs into the lower portion of the plasma column.

For the second point, when the brightness of the images is analyzed one notices finer details not immediately attainable from visually inspecting the images. The purple line drawn through the left hand fVC images is plotted in the second column on the right of Figure 5.13 as brightness traces, respectively. The brightness traces show that there is a small increase between 200 pixels and 400 pixels (visual plasma core) during the gas puff. This small increase could be due to the helium penetrating to the core of the plasma column or it could be due to the helium 'migrating' in the edge of the plasma to the camera view location. An Abel inversion was performed on the bottom half of the data shown in the top and bottom right figures of Figure 5.13 to obtain emissivity profiles.

The top figure in Figure 5.14 is the brightness profile discussed previously and the bottom plot is the emissivity profile. The emissivity profiles calculated show that the majority of radiation measured by the camera is coming from the edge of the plasma column. The no-puff shot emissivity (blue dotted trace) is either background bremsstrahlung or impurities in the plasma, so this emissivity trace was subtracted from the gas puff emissivity trace (solid blue trace) to get an absolute emissivity (solid black trace). After the subtraction, the absolute emissivity shows that the majority of the radiation is coming from the edge of the plasma column, further confirming that the HELIOS is measuring the edge plasma parameters. This result furthers the understanding of how the HELIOS diagnostic is operating on the linear device with a deuterium discharge, Proto-MPEX, and prompted a campaign to improve the diagnostic in an attempt to measure the core parameters.

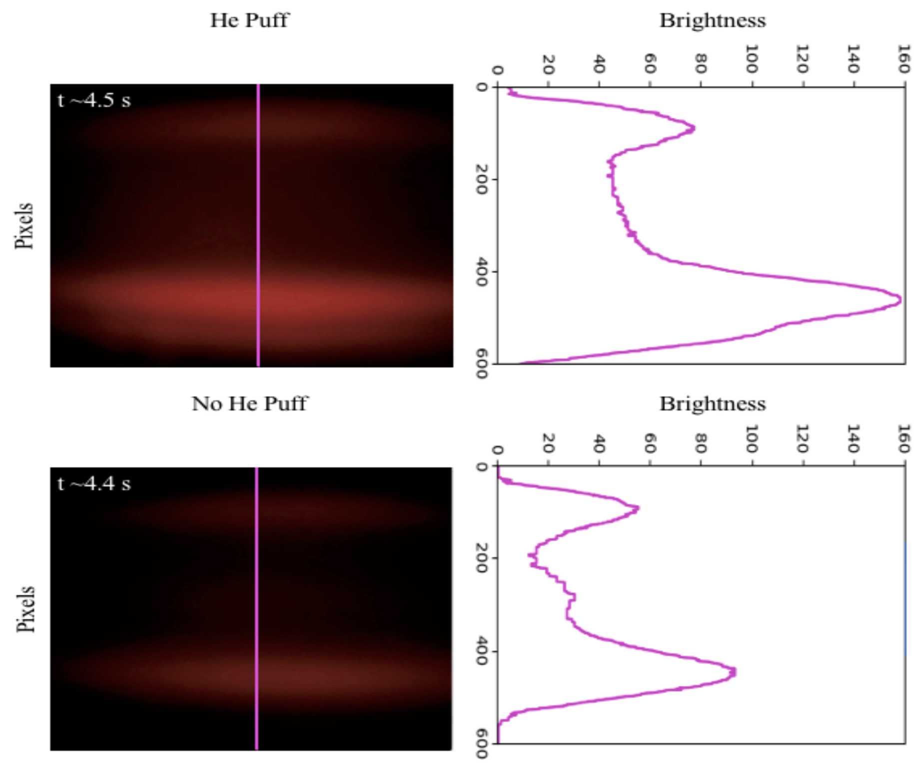

Figure 5.13. Two frames from the fVC video that is before and during the gas puff.

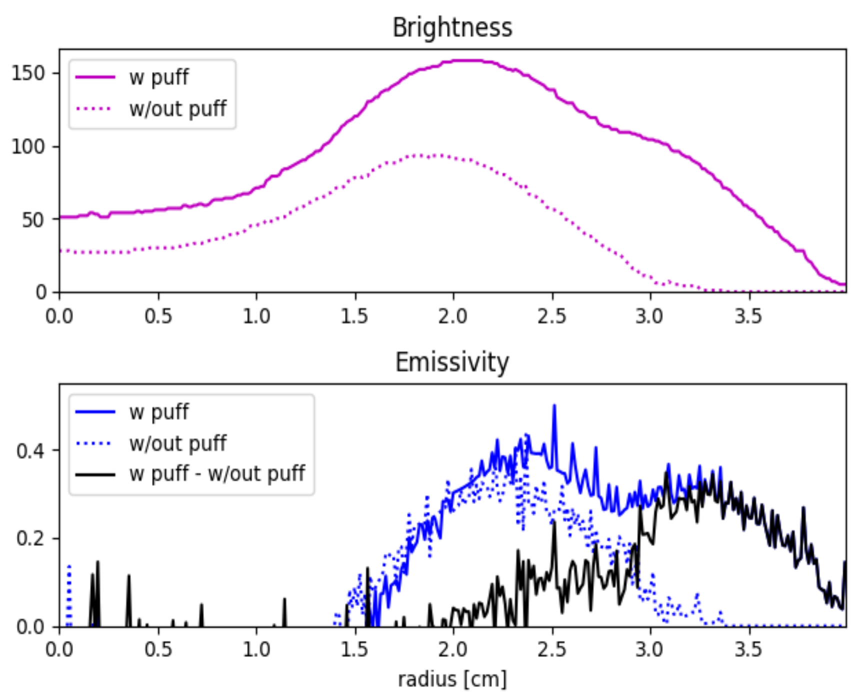

Figure 5.14. Brightness profile and Abel inversion of the bottom half of the plasma.

During a three-month maintenance period the TS system was removed from the central chamber location, allowing for the PV-10 gas injection system to be installed vertically. A long nozzle fed through a quick connect fitting gave the PV-10 system the capacity to puff gas directly adjacent to the plasma column and normal to the TS 24-chord collection optics. Figure 5.15 shows a schematic of the PV-10 (top) and the tip of the PV-10 nozzle (bottom) at the central chamber with the collection optics back lit for alignment. A transparent image, from the same monochrome fVC, of the plasma passing through the region of interest is overlaid onto the image for perspective. This is a single plasma pulse and does not represent all the plasma diameters achievable in Proto-MPEX. In the bottom of the image in Figure 5.15 is the old gas puff used for the preliminary analysis shown earlier in this chapter. By using a multi-chord optical setup, at the location of the HELIOS gas puff, measurements of T_e and n_e as a function of radius could be determined. For the filterscope setup the machine conditions will need to be maintained over a series of shots as the patch fiber is moved between each of the twenty-four locations. For the McPherson spectrometer, which has a five-fiber array, a similar process will need to be performed but with 1/5 fewer shots.

With the gas outlet now periphery to the plasma column, increasing the gas penetration can be further explored. The penetration depth of the gas (mean free path) into the plasma is governed by Equation 5.5.1, where v_{th} is the thermal velocity and S_i is the ionization rate coefficient, which is described in Chapter 4.

$$d_{gas} = \frac{v_{th}}{n_e S_i} \qquad \text{Equation } 5.5.1$$

This equation clearly shows why the gas puff is not penetrating past the plasma edge. The penetration depth of the gas puff is inversely proportional to the electron density of the plasma. The dependence on the ionization rate coefficient led to the hypothesis that if the gas density is consistently increased over a series of shots then the gas will eventually reach the plasma core. By increasing the gas puff density, the particles of the gas puff have a higher probability of penetrating to the core of the plasma column. The final sections of this chapter will detail a gas density experiment performed on Proto-MPEX to improve gas penetration and resolve the core density and temperature values. Equation 5.5.1 will be further discussed in Chapter 7.

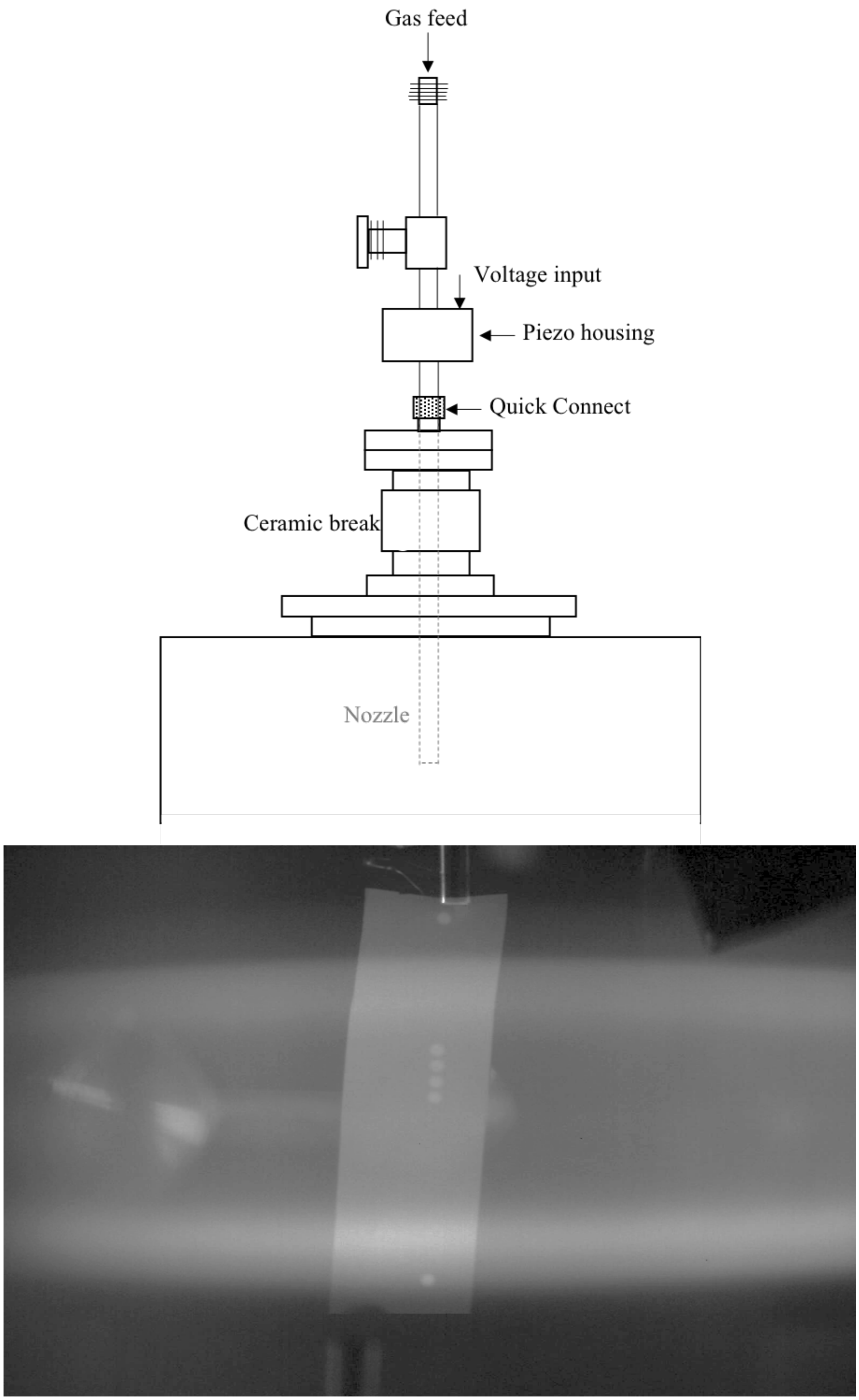

Figure 5.15. New PV-10 Gas Injection System Installed at the Central Chamber.

5.5 HELIOS Gas Penetration Experiment and Results

In order to attempt measurements of the core electron density and temperature of the Proto-MPEX plasma using HELIOS, an experiment was planned to increase the gas puff throughput until the gas puff penetrated to the plasma core. Since the focus of the experiment is to resolve the core density and temperature there was no concern on how perturbative the gas puff was to the edge of the plasma column. Figure 5.16 is a cartoon mockup of the GPE broken into two steps. The first portion of the experiment (left top block) was focused on getting the helium gas to the core plasma and having some diagnostic confirmation that the gas had reached the core flux tubes. In the upper block cartoon of Figure 5.16 the red dashed ovals indicate the gas puff for a specific voltage applied to the piezoelectric valve. The voltage is gradually increased on the piezoelectric crystal until the DLP (blue dot) inserted to the core flux tube shows perturbation in its signal. A fVC image is shown in the top right of Figure 5.16 with the core DLP visible on the right-hand side and the gas puff nozzle, periphery to the plasma column, at the top. The injected helium is indicated by the brightened signal near the nozzle outlet. For step one, once the gas penetrates to the plasma core and perturbs the DLP signal the voltage setting prior to the DLP perturbed signal (92.5 V) is recorded. Figure 5.17 is the DLP n_e and T_e measured values as a function of time. The green plot in the top row is the DLP measurements during the gas puff with voltage of 92.5 V applied to the piezoelectric crystal in the PV-10 gas injection system. The bottom row are voltages $>$ 92.5 V. They clearly show the perturbation in the DLP signal due to the gas puff in the range $4.41\ seconds\ \lesssim time\ \lesssim 4.54\ seconds$.

In step two of the gas penetration experiment the voltage applied to the piezoelectric valve, corresponding to the green trace in Figure 5.17 (92.5 V), is used to collect HELIOS data as a function of radius. The McPherson spectrometer was used as the main light collecting diagnostic for step two with the filterscope radiometer and fVC as supporting diagnostics. Even though the Filterscope is a powerful tool for resolving temporal information in the plasma, the decision to utilize the McPherson was due to its spectral resolution.

Figure 5.18 compares the McPherson temperature and density dependent ratios (x) with the Filterscope ratios (dots). The temperature dependent ratios show consistency near the edge of the plasma but the filterscope density dependent ratios fall a little below that of the spectrally resolved McPherson ratios.

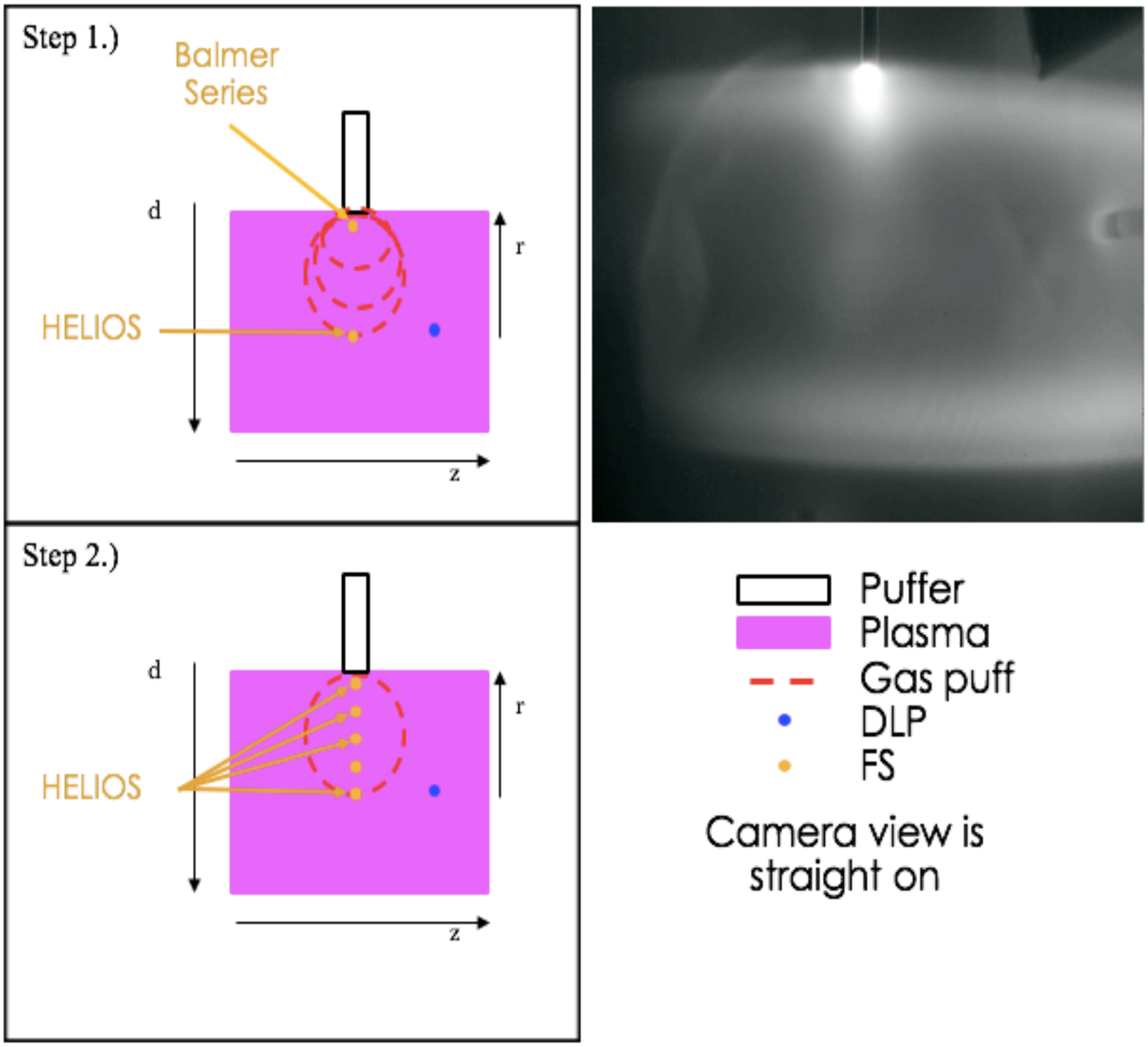

Figure 5.16. Cartoon of the Gas Puff Depth Experiment and Image from the fVC during a Gas Puff, showing the puffer and the on-axis DLP.

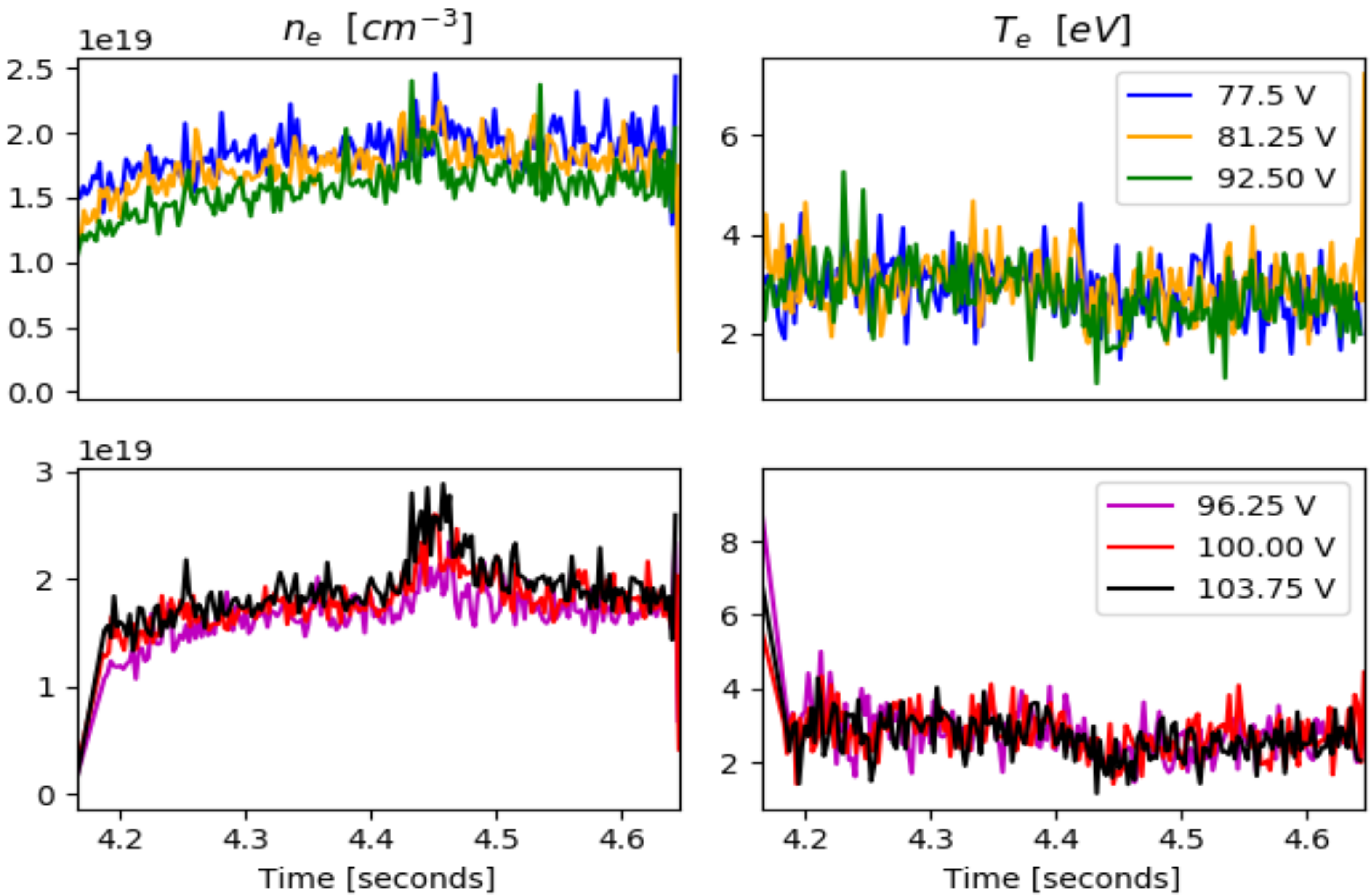

Figure 5.17. DLP n_e (left column) and T_e (right column) for the Non-Perturbing Gas Puffs (top row) and the Perturbing Gas Puffs (bottom row).

Figure 5.18 also shows a very important radial trend between the two diagnostics. From the core of the plasma outward the ratios demonstrate the same trends. For the T_e measurements this trend is a flat profile that slightly decreases near the edge of the plasma. For the n_e measurements this is a flat profile that begins to increase at the edge of the plasma. Such a trend supports that the calibrations performed to yield photon flux are good. The Filterscope is somewhat handicapped by the bandpass of the filter used to collect specific helium line data. If there are any impurities within the bandpass of the filter then the data is not as reliable; consequently, due to their possibly being an increased number of impurities after Proto-MPEX was brought back online in the Fall of 2018 it was decided that the McPherson would produce more reliable data for HELIOS.

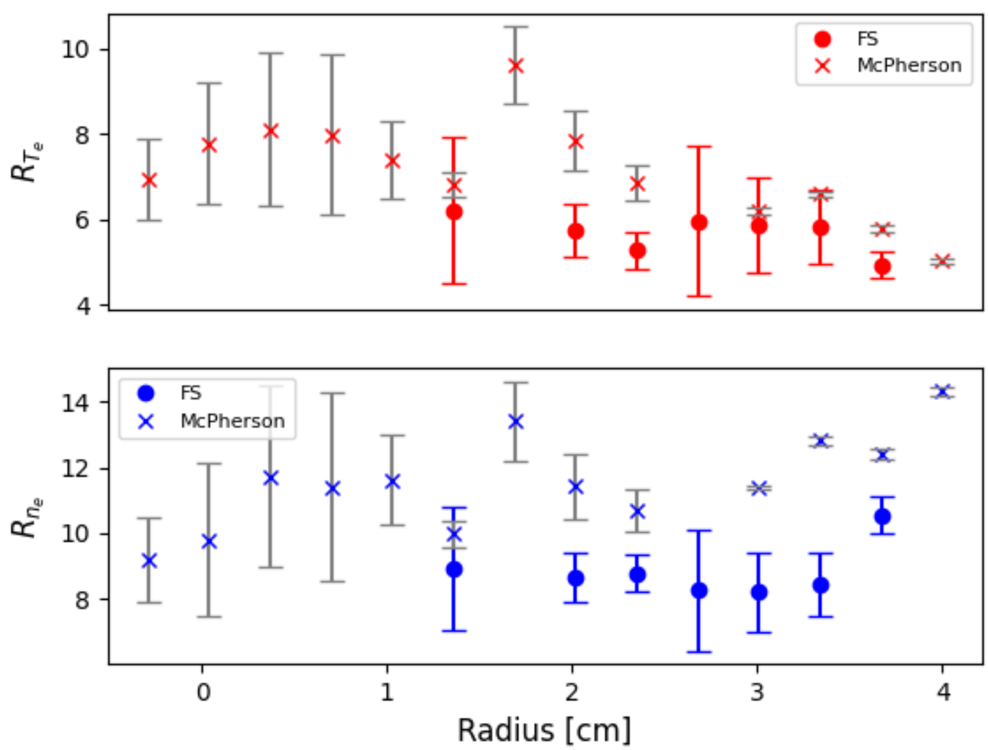

Figure 5.18. Helium line ratios from the McPherson Spectrometer and Filterscope.

In an attempt to observe the gas puff penetrating to the plasma core, the fVC camera was used to record video of the plasma during gas puffing with three separate He I two-inch filters (670±10 nm, 710±10 nm, and 720±10 nm). Due to the cameras dynamic range it was difficult to obtain a single video showing the gas puff movement through the plasma. Figure 5.19 is an image obtained from the monochrome camera with a 710±10 nm two-inch bandpass filter and looking normal to the gas puff at a shutter speed of 1 ms, (the shutter is open for 1 ms). The camera collected light from the plasma column during gas injection.

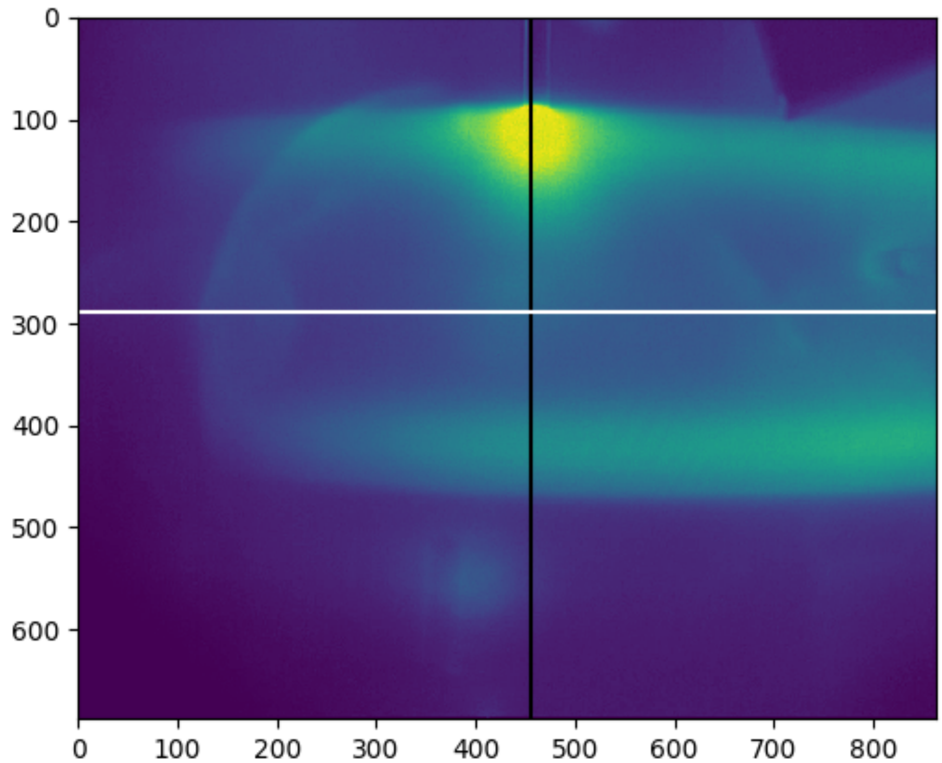

Figure 5.19. fVC Image of the Gas Puff at 92.5 V with a 710±10 nm.

The bold yellow region near the outlet of the nozzle and in the plasma edge is a saturated location of the gas puff. A vertical black line is drawn through the image to show the gas puff axis and the DLP is just visible in the right-hand side of the image directly above the horizontal white line. The high shutter speed allows for the camera to resolve the lower intensity light the further into the plasma column. However, the high shutter speed causes the light near the edge of the plasma (highest concentration of helium) to saturate, meaning that multiple plasma shots are necessary to stitch together a full profile along the radius of the plasma column. This fact along with the large bandpass of the two-inch filters are a reason that the camera HELIOS will not be further analyzed.

Analysis of the data collected in step two of the GPE (Figure 5.16) is shown in Figure 5.20. The DLP radial scan data is from a radial scan performed prior to the experimental day with the same machine configurations. The discharge was deuterium with a magnetic field of ~0.6 T at the helicon antenna and ~0.4 T near the target. The fueling gas was injected into the chamber at 4.8 V for 0.30 seconds and then 4.7 V for 0.48 seconds before turning off, resulting in a total of $6.52 \times 10^{19}\ particles$ injected into the vacuum vessel. He is injected at $4.82 \times 10^{19}\ particles$. During the operations for the gas penetration experiment the plasma radius was slightly smaller in size and lower in density than the DLP radial scan plasma. Figure 5.21 is a map of the B-field and the radius of the LFS for the day of the experiment (solid black line) and the DLP radial scan day (blue dotted line). Furthermore, the DLP radial scan data is along the horizontal axis of the plasma radius whereas the HELIOS data is from the vertical axis. Plasma parameters are not expected to vary azimuthally. With that being said, the most important point for comparison is at the DLP data location of $r_p = 0.0\ cm$ due to it being the core of the plasma and furthest away from the perturbative gas puff at the edge of the plasma column.

The DLP data shows $n_e \approx 2.00 \times 10^{13}\ cm^{-3}$ and $T_e \approx 2.75\ eV$. HELIOS measurements of n_e are twice the value of the DLP data at $r_P = 0.0\ cm$ and show that at $r_P = 0.37\ cm$ the plasma electron density is over $1 \times 10^{14}\ cm^{-3}$. Since the high-density value is so close to the center of the plasma, meaning that it is the furthest away from any perturbative helium gas puff, the density value is believed to be too high. A higher number of particles of helium are being puffed into the plasma edge than the fueling gas. Therefore, the region nearest the gas puffer will be perturbed by the He gas puff. In other words, the more gas introduced to the plasma the higher the electron density will be, making it plausible that the electron density would increase to over $1 \times 10^{14}\ cm^{-3}$ near the edge of the plasma column, but not likely near the core where the DLP signal shows little to no perturbation by the gas puff. Hence, a conclusion on whether the density values are high is difficult due to the fact that the radial scan was not performed during the increased gas puff at the edge of the plasma.

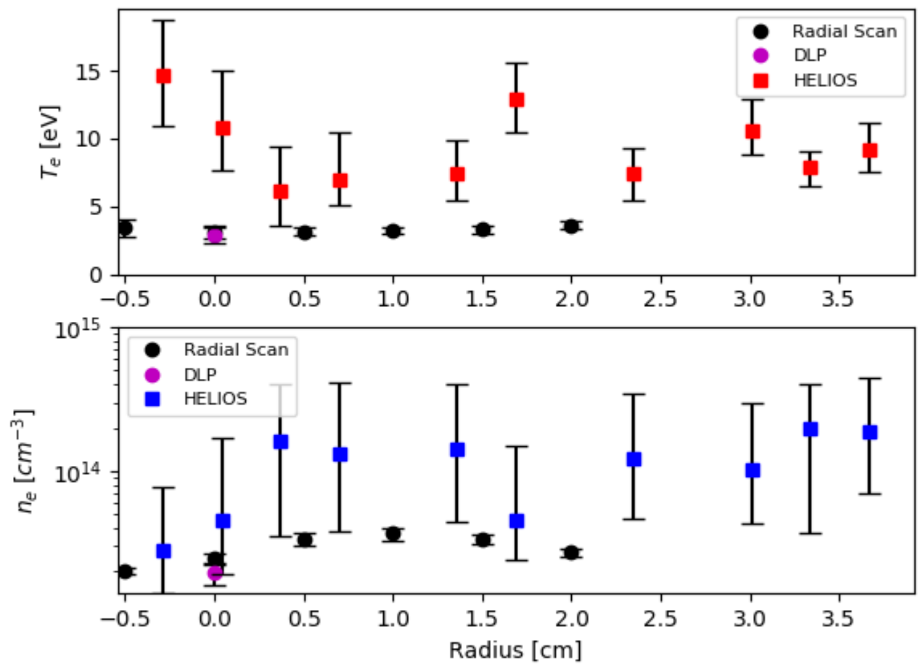

Figure 5.20. HELIOS derived T_e and n_e values for the Penetration Experiment compared to DLP measured T_e and n_e on the center axis (purple) during HELIOS measurements, and DLP radially measured T_e and n_e from an experiment performed on a separate day.

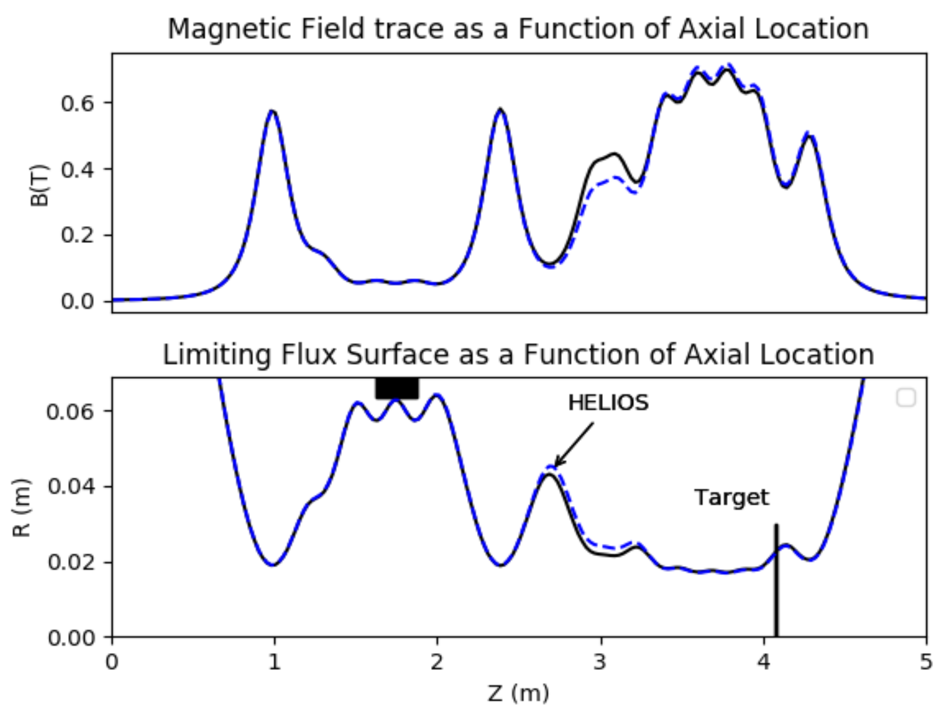

Figure 5.21. B-field and LFS radius along the axis of Proto-MPEX during the DLP radial scan and the day of experiment.

For the T_e values, a clear conclusion can be made. For starters the HELIOS inferred electron temperature are two to six times higher than the DLP measured electron temperature values. From this comparison alone the HELIOS T_e measurements are an overestimation of what the plasma parameters are. One might be concerned about the perturbation of the gas puff effecting the measured T_e value, but the bottom right figure in Figure 5.17 shows that if the electron temperature was being perturbed by the increased gas puff then the values would decrease not increase. This result led to the suspicion that the HELIOS CRM used to derive the T_e and n_e values could potentially be missing important physics relevant to the experiment.

5.6 HELIOS Measurement Summary

Data from the PV-10 HELIOS at the central chamber was compared to TS and a downstream edge DLP. From the comparison it was shown that the HELIOS density data showed consistency to the edge values measured by the TS and that T_e, n_e HELIOS was in agreement to the downstream edge DLP data. Further comparison was made using the UW-M gas injection system adjacent to the helicon antenna to a DLP. The UW-M HELIOS data once again showed consistency to edge DLP values, supporting that the HELIOS measurements are edge localized. A fVC was used to record an image prior to the gas puff and during the gas, so that the data could be inverted, and an absolute radial profile of the helium line emission could be examined. The measured helium emission concluded that the helium signal is localized to the edge of the plasma column.

The validation experiment to confirm that HELIOS is working on Proto-MPEX concluded that the helium line emission is localized to the plasma edge. Proto-MPEX has a relatively high core n_e, meaning that the helium gas puff has a hard time penetrating past the plasma edge. This is due to the fact that the depth of the gas puff is inversely proportional to the n_e and the ionization rate coefficient. Therefore, a GPE was planned that increased the gas throughput until a DLP attached to the core flux tube perturbed, supporting that the gas puff had reached the plasma core. The analyzed HELIOS data was compared to a DLP Radial Scan from a prior day and the core DLP measurements during the experiment. The comparison concluded that the T_e and n_e values from HELIOS were an overestimation of the actual plasma parameters and that the increased gas puff was causing an atomic physics phenomenon that the ORNL CRM was not interpreting correctly.

Chapter 6 will go deeper into the modelling portion of the HELIOS diagnostic and explore the missing atomic physics. The CRM will be modified to include this new physics and the data presented in this section will be re-analyzed using the newly modified CRM.

Chapter 6 Modelling

The CRM is a key tool for the experimental HELIOS and required for understanding the physics behind the technique. The results so far have shown that there is a discrepancy between the data or model for the high gas puff case. The data collected can be considered as an accurate representation of the physics in the plasma; therefore, the model may not be accurately representing the proper physics that is occurring in the system. For the purpose of this document, the system will be defined as the deuterium plasma, the vacuum chamber, and the neutral helium gas puff. As mentioned in Chapter 1 the CRM utilizes rate coefficients to calculate the photon flux of a specific line of helium. For the preliminary results and the perturbation experiment the model only included the population and de-population contributions to the line intensity by electron excitation/de-excitation ($F_{ij/}$ F_{ji}) and ionization by electron impact (S_i).

Since the HELIOS T_e values from the GPE, 11 eV- 15 eV, are clearly an overestimation of the plasma parameters (2 eV – 4 eV) the investigation was focused heavily on the 706.53 nm line intensity or the $3^3S \rightarrow 2^3P$ transition. The 706.53 nm emission line is the numerator in the temperature dependent ratio. This conclusion was further supported by the data shown in Figure 6.1. The top figure is the calculated ratios from the CRM as a function of T_e at $n_e = 2.00 \times 10^{13}\ cm^{-3}$ (the density of the plasma during the GPE) and the bottom figure are the ratios measured with the McPherson from the GPE. In the top figure there is a clear trend for T_e values below 14 eV, the temperature dependent ratio gradually increases above the density dependent ratio as T_e decreases. In the bottom figure the temperature dependent experimentally measured ratios do not demonstrate this trend. In fact, the temperature dependent ratios from the ORNL CRM are roughly three times lower than expected for the plasma T_e and n_e parameters measured by the DLP. Due to the discrepancy between the calculated and measured temperature dependent ratios and the overestimation of the T_e values in Figure 5.20, an investigation into why the 706.53 nm line is too low was explored.

It was found that in a linear helium plasma the 706.53 nm line is prone to re-absorption depending on the population of the lower state transition.[9] Due to the lower state population being a metastable its relaxation time is long, increasing the probability of re-absorption (photon is emitted by an atom and absorbed by separate atom) of the 706.53 nm line in opaque helium plasmas. Since the plasma in Proto-MPEX is a deuterium plasma and the gas puff is helium the re-absorption of the 706.53 nm line is not very likely. However, a similar phenomenon occurs for the singlet state transitions that terminate on the ground state when the neutral density between the gas puff and the collection optics is significant.[11,12,43]

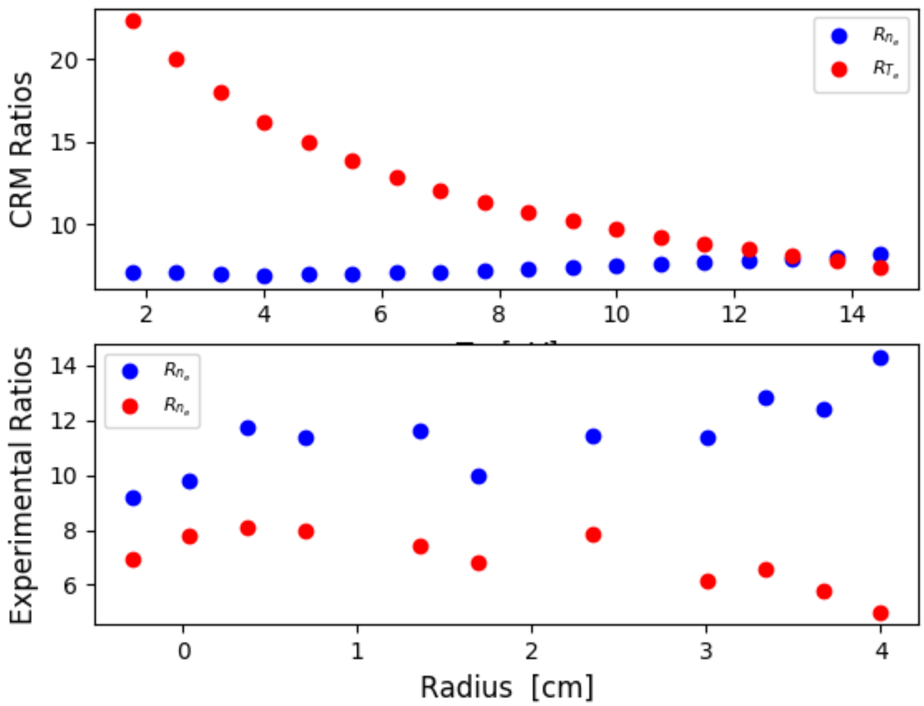

Figure 6.1. CRM calculated ratios as a function of T_e and experimental measured ratios as a function of radius.

As the gas puff throughput increased, so did the pressure in the vacuum vessel. Figure 6.2 is an image of the pressure change recorded by a Baratron at the vacuum vessel wall over a range of voltages applied to the piezoelectric crystal in the PV-10 gas puffer. The peak dark blue trace (92.5 V on the piezo) is the voltage used for step two of the GPE discussed in the previous chapter. The pressure increases by almost a factor of six. The neutral density of helium at the wall can be approximated using the ideal gas law (equation 6.1.1) with the gas temperature, $T_g \cong$ 400 Kelvin.

$$\frac{PV_{Proto}}{RT_g}N_A = n_{He\,Wall} \qquad Equation\ 6.1.1$$

Here, P is the pressure recorded by the Baratron, V_{Proto} is the volume of Proto-MPEX (calculated in Chapter 3), $\boldsymbol{R}$ is the ideal gas constant, and N_A is Avogadro's number. The neutral density at the wall is approximated to be $n_{He\,Wall} = 1.47 \times 10^{14} cm^{-3}$. This neutral density value is much higher than normal operating conditions; therefore, it is hypothesized that the increase of pressure (neutral density of helium) in the chamber between the plasma and the collection optics at the wall is causing re-absorption of some or all of the light associated with the $3^3S \rightarrow 2^3P$, $3^1S \rightarrow 2^1P$, or $3^1D \rightarrow 2^1P$ transition. This is causing the HELIOS derived values of T_e and n_e from the CRM to be in disagreement with the DLP data at the same location. This physics needs to be included in the CRM to accurately infer T_e, n_e.

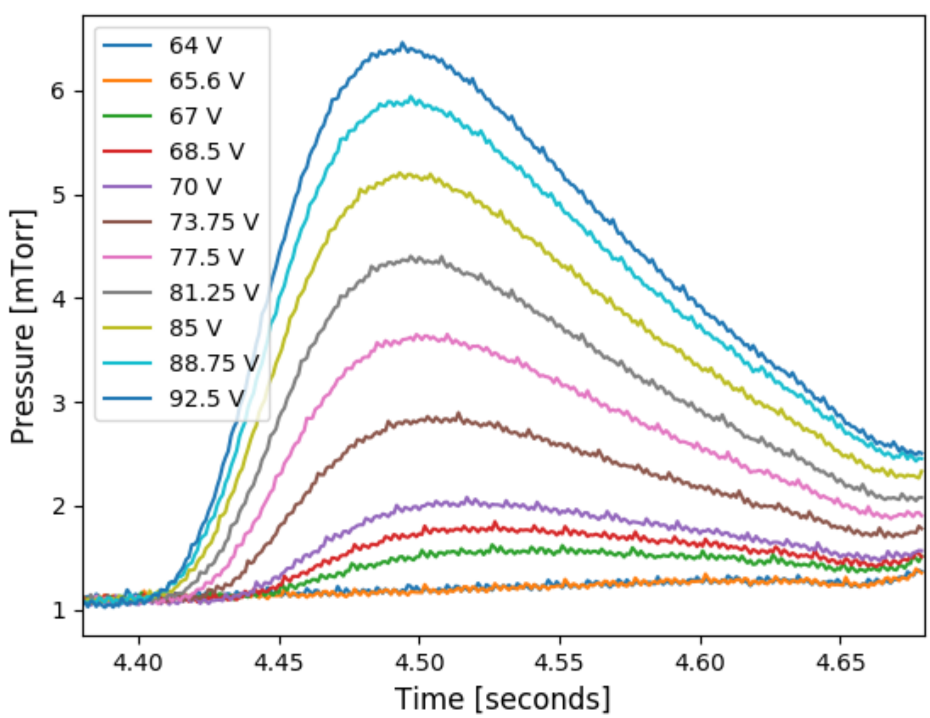

Figure 6.2. Pressure Change as the Gas Puff is Increased.

Two models are available for use for HELIOS on Proto-MPEX. A model known as the ORNL CRM, which is accessible for modification and thereby understood, and the Hybrid Time Dependent/Independent (HTD/I) CRM, which has been worked on over the years to create a universal CRM for the use of this technique. The ORNL CRM is available to be edited and will be the main focus of this study; however, any edits can be added to the HTD/I CRM should this be considered as a contribution to the field of atomic physics. In section 6.1 radiation trapping will be explained as well as accounted for in the ORNL CRM, using the optical escape factor (OEF) method. Section 6.2 details important information about the ORNL CRM and how the OEF method is implemented. In section 6.3 the process and results of testing the hypothesis through modelling will be discussed.

6.1 Radiation Trapping of He I Lines by Excess Neutral Density

It has been shown that for a helium plasma the electron density plays a large role in the opacity of the plasma to certain HELIOS line transitions.[9] High density helium plasmas ($> 1 \times 10^{13}\ cm^{-3}$) absorb lines to a certain degree, decreasing the emission observed through optical emission spectroscopy (OES). This phenomenon is due to the emission measured and the plasma being the same, so as the electron density increases the plasma becomes opaque to certain lines. In a deuterium plasma, where helium must be injected through a nozzle of some sort, absorption should not contribute significantly to line emission due to the separate species and the controlled gas puff. Whereas this may be the case for large volume devices that have a lower neutral population, Proto-MPEX has a considerably smaller volume and higher core electron densities ($> 1 \times 10^{13}\ cm^{-3}$). The electron density of the deuterium plasma plays a role in the penetration of the gas puff, as described in Chapter 5, which has required that there be an increase in helium gas injection. This initial gas density, $n_{He\ Injected} = 6.12 \times 10^{14}\ cm^{-3}$, is only partially ionized by the plasma column, leaving neutral helium to fill the system. Because the plasma is a “sink” to He, the plasma He population only increases.

The light must travel from the plasma to the collection optics, located at the wall of Proto-MPEX, and if there is a significant amount of neutrals in the system then *radiation trapping* can occur. Radiation trapping is when an excited (*j*-state) atom of helium, in a gas medium made up of *i*-state (ground state) and *j*-state atoms, emits a photon of some energy and frequency. This photon is later re-absorbed by an atom in the *i*-state, which will emit a photon of the same energy

and frequency. This photon is once again re-absorbed by an atom in the ground state. A chain reaction of the photon being emitted and re-absorbed in the gas medium can occur, 'trapping' the photon. This process is termed radiation trapping and can be represented in the CRM by adjusting the Einstein coefficient of spontaneous transition, A_{ji}, with an approximated *optical escape factor* (OEF), g_0, meaning that $A_{OEF} = g_0 A_{ji}$.
A cylindrical approximation for g_0 is given in equation 6.1.1.[11,12,43]

$$g_0 = \frac{\left(1.92 - \left(\frac{1.3}{1 + (k_0 R)^{\frac{6}{5}}}\right)\right)}{(k_0 R + 0.62)(\pi \ln(1.375 + k_0 R))^{\frac{1}{2}}} \qquad \textit{Equation } 6.1.1$$

where *R* is the characteristic radius of the system and the *absorption coefficient*, k_0, is given by equation 6.1.2.

$$k_0 = \frac{e^2}{4 m_e c \epsilon_0 \Delta\nu \sqrt{\pi}} n_j f_{j,i} \qquad \textit{Equation } 6.1.2$$

where n_j is the population of the lower state for a specific transition and $\Delta\nu = \frac{\nu}{c}\sqrt{\frac{2 k_b T_g}{m_{He}}}$ is the width of the spectrum (FWHM) with central frequency ν_0. The lower state population is determined by the transition of interest. For example, if the transition of interest were $1^1S \rightarrow 2^1P$ then the population that would determine k_0 would be $n(1^1 S)$. The *absorption oscillator strength*, $f_{j,i}$, is given by equation 6.1.3.[43]

$$f_{j,i} = A_{j,i} \left(\frac{g_j}{g_i}\right) \left(\frac{c}{\nu_0}\right)^2 \left[\frac{\epsilon_0 c m_e}{2\pi e^2}\right] \qquad \textit{Equation } 6.1.3$$

A simplified equation for model calculation in terms of frequency (Equation 6.1.4) or wavelength (Equation 6.1.5) can be determined if equation 6.1.3 is inserted into equation 6.1.2.

$$k_0 = \left(\frac{c^3}{\nu_0^3}\right) \left(\frac{j}{g_i}\right) \left(\frac{1}{8\pi\sqrt{\pi}\nu_{He}}\right) n_j A_{ji} \qquad \textit{Equation } 6.1.4$$

$$k_0 = \lambda^3 \left(\frac{g_j}{g_i}\right) \left(\frac{1}{8\pi\sqrt{\pi}\nu_{He}}\right) n_j A_{ji} \qquad \textit{Equation } 6.1.5$$

A very important thing to note about the calculation of k_0 is its dependence on the lower state population. This means that the amount of neutral gas still existing in the system can potentially alter the physics of the 2^1P population due to the significant number of atoms in the ground state. This would have an impact on the intensity of the 667.9 nm ($3^1S \rightarrow 2^1P$) and 728.0 nm ($3^1D \rightarrow 2^1P$) lines.

He gas ($6.12 \times 10^{14} cm^{-3}$) is injected into the vacuum vessel. Due to the small volume of Proto-MPEX and the large gas puff from the helium puffer, the pressure in the chamber increases by a factor of six. This means that there is a significant amount of neutral helium in the chamber. The emission of helium at the plasma must traverse the neutral density in the system to reach the collection optics at the wall. If radiation trapping occurs prior to the photons reaching the collections optics then the measured light intensity of each line will be less than the actual value emitted by radiative and collisional processes, hence, the proper inclusion of radiation trapping effects in the CRM is necessary to test the hypothesis.

Figure 6.3 shows in the left-hand plot the magnetic field and LFS as a function of the machine axis. In the bottom left-hand figure, a black rectangle is drawn to represent the helicon antenna location, a solid black line is drawn to represent the target, and an arrow is drawn to indicate where HELIOS measurements were made. The right-hand figure in Figure 6.3 is a to-scale version of the Proto-MPEX and plasma cross-sections. The radius of the plasma in the right-hand figure is determined by the LFS.

In the right-hand figure at the edge of the vacuum vessel a Baratron gauge was used to approximate the neutral density of helium near the wall, $1.47 \times 10^{14}\ cm^{-3}$, using the ideal gas law. Determining the neutral density of He at the plasma is more complex due to the fact that there are no pressure measurements at this location. A basic calculation can be performed called the Saha Equation of fractional ionization, equation 6.1.6, to estimate the neutral density of helium at the plasma.[43,68] The Saha Equation of fractional ionization assumes local thermodynamic equilibrium (LTE) and solves for the fraction of atoms in an ionized state (n^+) to the atoms in a neutral state (n_0).

$$\frac{n^+}{n_0} = 2\frac{U(T)}{U^+(T)n_e}(C * T_e)^{\frac{3}{2}} e^{-\frac{C2}{T_e}} \qquad Equation\ 6.1.6$$

$U(T)$ and $U^+(T)$ are the partition functions of the ground and ionized state respectively, $C = \frac{(2\pi m_e k_B)}{h^2}$, and $C2 = -\frac{\chi}{k_B}$, where χ is the ionization potential for the ground state to the z+1 level (24 eV) in units of energy [J]. For He injected into the Proto-MPEX plasma ($n_e \approx 2.00 \times 10^{13}\ cm^{-3}, T_e \approx 2.75\ eV$), $\frac{n^+}{n_0} = 4.47 \times 10^5$. The positive fractional ionization value indicates that there are significantly more ionized helium atoms than neutral atoms at the plasma. If one were to assume that $n^+ = n_e$, due to the perturbative nature of the experiment, then the number density of neutral helium at the plasma would be $n_0 = n_{He\ Plasma} = 5.38 \times 10^7\ cm^{-3}$. The neutral density at the wall as compared to the approximated neutral density at the plasma is several orders of magnitude higher. Since the profile of neutral density between the plasma and the wall is not available, a flat profile assumption is made by averaging the neutral helium density at the wall and at the plasma, $n_{He} = 7.33 \times 10^{13}\ cm^{-3}$. This neutral helium density is used for the OEF application. To fully understand how this assumption effects the analysis of the OEF value; g_0 for the 1^1S → 2^1P transition is shown in Figure 6.4 as a function of neutral density. The low-end neutral density is the no-OEF case ($g_0 = 1$) and the high-end value is the gas puff density injected into the plasma. The temperature and density dependent ratios for the high-end and low-end case of neutral density are also shown in Figure 6.4 to help determine how the flat profile assumption will affect the derived values of T_e and n_e from HELIOS.

Ratios are determined by generating contour plots using each neutral density to calculate g_0 and then using the T_e and n_e values from Proto-MPEX. The OEF drops by almost of factor of three from the no-OEF case to the high-end neutral density case. This means as the neutral density increases the probability of spontaneous emission decreases by almost a factor of three. The corresponding temperature and density dependent ratios vary by almost a factor of two between the no-OEF case and the neutral density measured at the wall in Proto-MPEX, showing that the choice of neutral density does play a large role in measured T_e and n_e from HELIOS. This information is important for the choice of neutral density to be used in the OEF method of radiation trapping in the ORNL CRM and lends to the hypothesis that accounting for radiation trapping due to the neutral density in Proto-MPEX is necessary for the HELIOS diagnostic to yield accurate $T_e,\ n_e$ measurements.

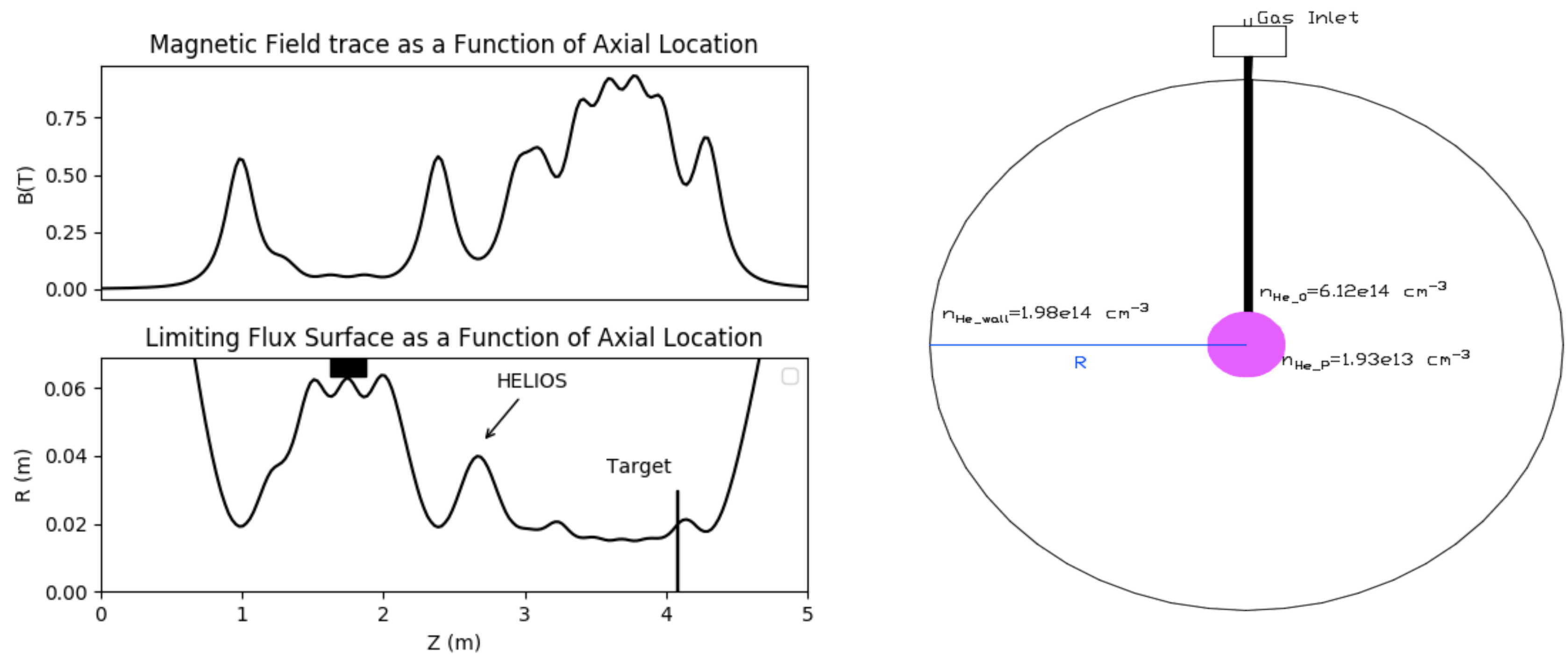

Figure 6.3 Magnetic Field and Radius of Limiting Flux Surface as a Function of Proto-MPEX's axis along with a Cross-Section of Proto-MPEX with Calculated Neutral Density from Plasma Core to Wall.

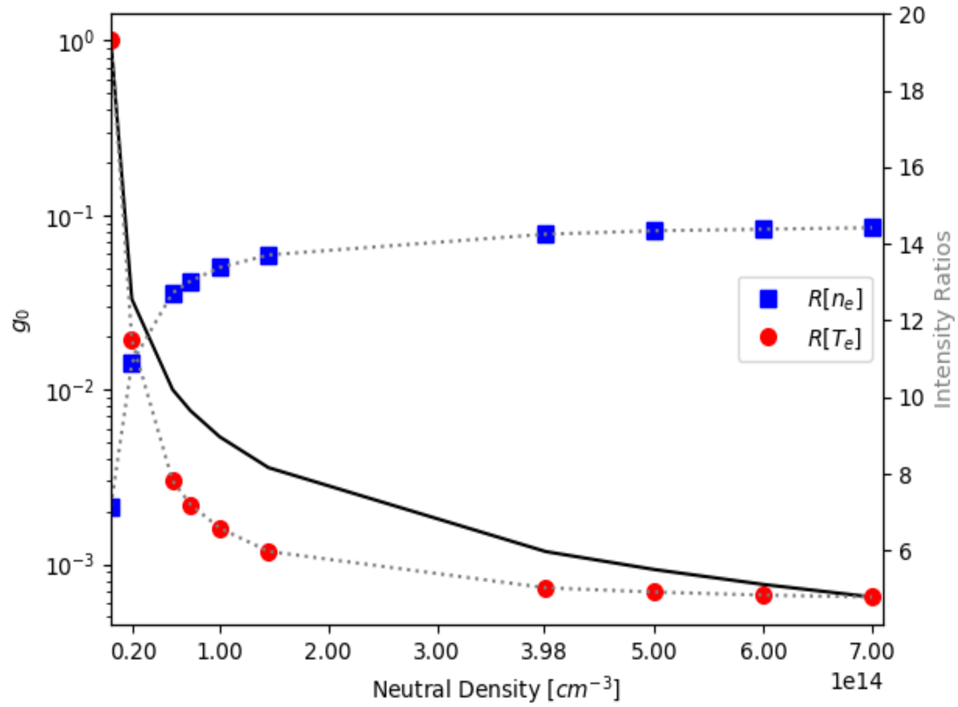

Figure 6.4. OEF and He Line Ratios Plotted as a Function of Neutral Density

A significant trend that is illuminated in Figure 6.4 is that as the neutral density increases the intensity of the 667.9 nm line intensity ($I_{667.9}$) is greater than 706.5 nm line intensity ($I_{706.5}$). This trend, $I_{667.9} \geq I_{706.5}$, matches the trend that is seen in the penetration experiment of Chapter 3. Seeing this trend in Figure 6.4 is a good indicator that for the Proto-MPEX increased gas puff experiment, in which the helium gas throughput was high, the OEF modification to the CRM is needed. Due to the neutral density profile from the core to the wall of Proto-MPEX being unavailable a flat profile assumption will be used ($7.33 \times 10^{13}\ cm^{-3}$). This assumption is due to the fact that the photons spend the least amount of time at the plasma (minimum) and at the wall (maximum) and most of its time traversing the distance between the two. Therefore, the best approximation for the OEF application is the average between these two values.

Furthermore, the absorption coefficient is also inversely proportional to the gas velocity, v_{He}. Since $v_{He} \propto \sqrt{T_g}$ Figure 6.5 shows the effect T_g has on g_0. The OEF and intensity ratios as a function of neutral gas temperature are shown in Figure 6.5. The low-end case is for room temperature and the high-end or extreme case suggests that the neutral gas has the same temperature as the ions in the plasma, $\sim 3\ eV$. The $I_{706.5}$ is greater than or equal to $I_{667.9}$ as the gas temperature increase past 10,000 K and the neutral density is maintained, $7.33 \times 10^{13}\ cm^{-3}$. As the gas temperature increases there is less of an effect from radiation trapping on I_{667} and I_{728}. The lowered effect is most likely due to the increase in the gas velocity, which increases the kinetic energy of the gas particles. Since the gas injected into the plasma from the gas injection system is at room temperature, the plasma is expected to only marginally heat the gas neutrals. For the range between 300 K and 500 K, g_0 increases by a factor of ~1.29, but the ratios demonstrate little to no change. A slightly elevated room temperature assumption for the gas will be made, $T_g = 400\ K$. This T_g will be used for OEF ORNL CRM implementation. The following section will give a detailed description of how the ORNL CRM is used to calculate the photon flux of the helium lines and how the ORNL CRM is modified to include the OEF.

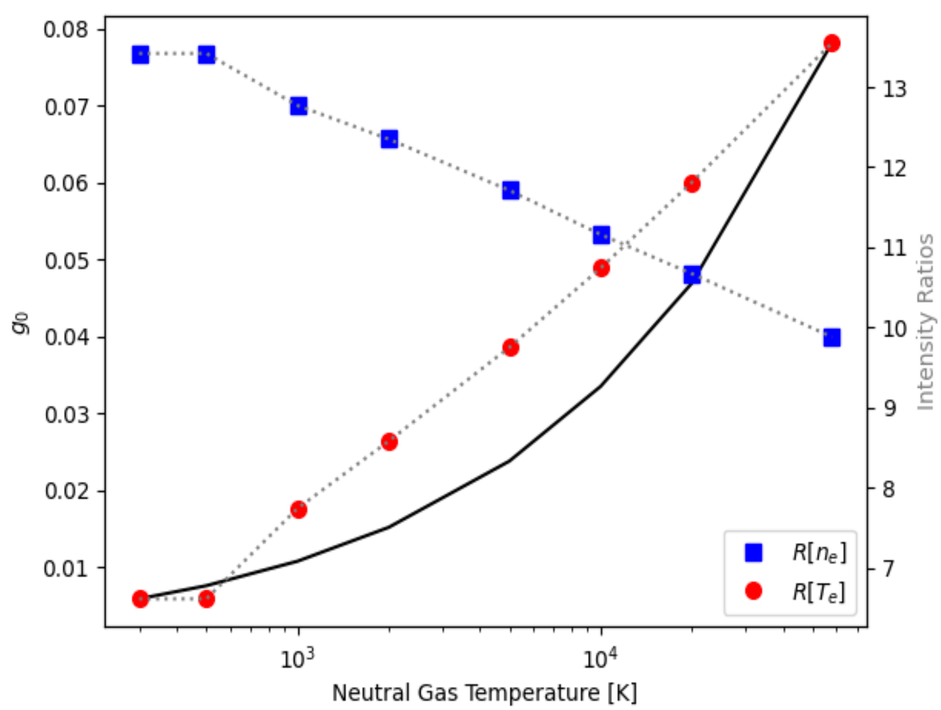

Figure 6.5. OEF and He Line Ratios Plotted as a Function of the Neutral Gas Temperature.

6.2 Modifying the ORNL CRM to Account for Radiation Trapping

The ORNL CRM calculates the upper state population by generating rate coefficients for q_{ji}/q_{ij}, equation 6.2.1.a and equation 6.2.1.b, and S_i, equation 6.2.2. S_i is the approximation made by Lotz.[69]

$$q_{j,i} = 8.63x10^{-6} g_i * \sqrt{T} * e^{-\frac{\Delta E}{T}} * \Upsilon_{j,i} \qquad Equation\ 4.2.1.a$$

$$q_{i,j} = q_{j,i} * \left(\frac{g_k}{g_i}\right) * e^{\frac{\Delta E}{T}} \qquad Equation\ 6.2.1.b$$

$$S_i = 3.0x10^{-6}\left(\frac{z}{\chi_i}\right) * \left(\frac{1}{\sqrt{T}}\right) * Ei(-x) \qquad Equation\ 6.2.2$$

Where $\frac{g_i}{g_k}$ is the ratio of statistical weights, z is ionization state, χ_i is the ionization potential of state i, $Ei(-x)$ is the exponential integral, and $\Upsilon_{i,j}$ is the effective collisional strength. The effective collisional strength is the collisional strength, $\Omega_{i,j}$,[70] averaged over the Maxwellian. The rate coefficients are used to calculate the upper state population through a generalized collisional radiative matrix, $\boldsymbol{C}$, which is a combination of the loss terms and the populating terms from equation 1.2.2. The loss terms and the contribution terms populate $\boldsymbol{C}$ by equation 6.2.3 and 6.2.4, respectively. The loss terms include all contributions from excitation, de-excitation, spontaneous transition, and ionization that cause state i to lose an electron. Similarly, the populating terms include all contributions from the same transitions that add an electron to the state i. With the knowledge of Chapter 1 and equations 6.2.3 and 6.2.4 the population density equation to be solved can be written in matrix, equation 6.2.5, and vector notation, equation 6.2.6.[32]

$$\boldsymbol{C}_{i,i} = n_e * S_i + \sum\left(n_e q_{i\to j} + A_{i\to j}\right) \qquad Equation\ 6.2.3$$

$$\boldsymbol{C}_{i,j} = n_e * q_{j\to i} + A_{j\to i} \qquad Equation\ 6.2.4$$

$$\begin{bmatrix} \frac{dn_1}{dt} \\ \vdots \\ \frac{dn_N}{dt} \end{bmatrix} = \begin{bmatrix} \boldsymbol{C}_{1,1} & \dots & \boldsymbol{C}_{1,M} \\ \vdots & \ddots & \vdots \\ \boldsymbol{C}_{N,1} & \dots & \boldsymbol{C}_{N,M} \end{bmatrix} \cdot \begin{bmatrix} n_1 \\ \vdots \\ n_N \end{bmatrix} \qquad Equation\ 6.2.5$$

$$\frac{d\boldsymbol{n}}{dt} = \boldsymbol{C} \cdot \boldsymbol{n} \qquad \textit{Equation } 6.2.6$$

Where $\boldsymbol{n}$ is the population of state i. Equation 6.2.5 is written out to i=4 in Appendix B. In the quasi-steady state case, the time derivative of the excited level population is approximated to zero, simplifying the solving of the population density. The ORNL CRM was used to calculate initial intensities prior to the OEF modifications of the HELIOS lines and the temperature and density dependent ratios are plotted as function of T_e, and n_e in Figure 6.6. Figure 6.7 is a flow chart describing each step taken in the Fortran CRM code to calculate the intensity of a specific He I line, I. The flow chart includes the steps taken for the no-OEF (Figure 6.6) and the OEF (Figure 6.9) calculations of the intensity for each of the three He I lines (667.90, 706.53, and 728.00 nm).

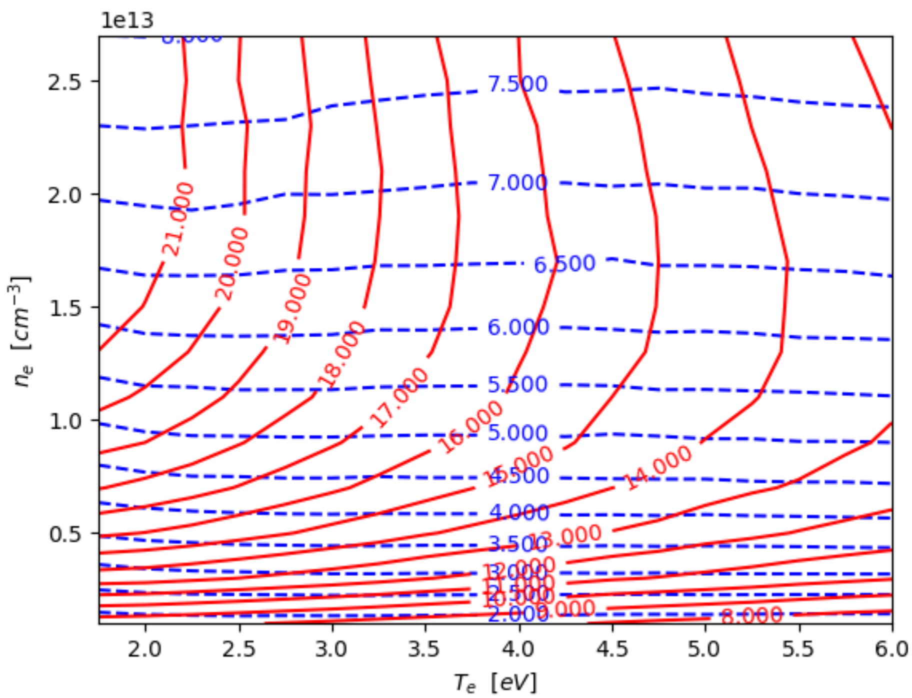

Figure 6.6. ORNL CRM Contour of the Intensity Ratios Prior to OEF Modification

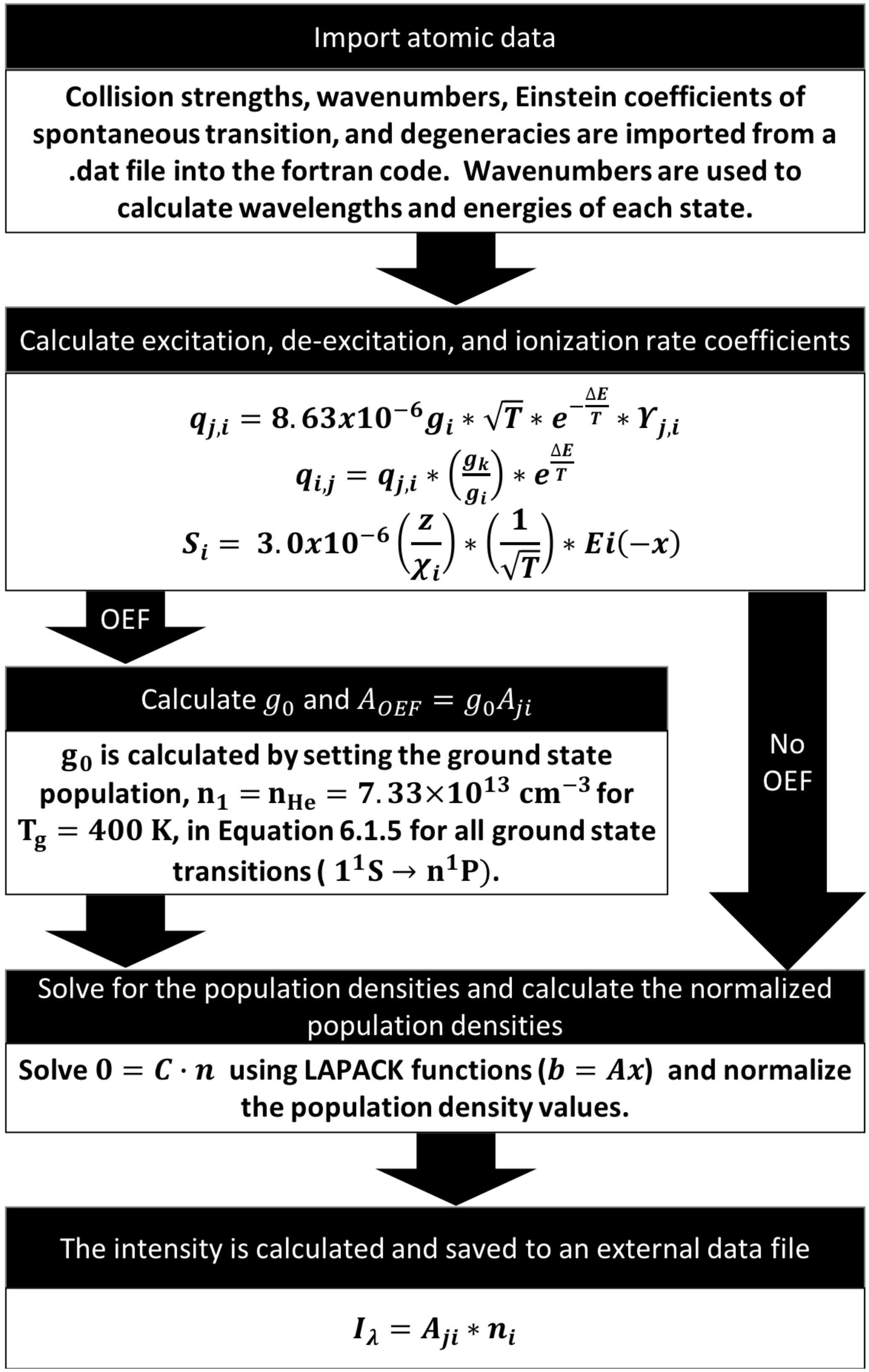

Figure 6.7. Flow charte describing the CRM fortran code process with and without OEF.

The radiation trapping physics is accounted for in the collisional radiative model by setting n_j equal to a non-zero value that represents the ground state population. This step is displayed in the flow chart as an alternative path after calculating the rate coefficients. The non-zero n_j is used to calculate g_0 and adjust the Einstein coefficient of spontaneous transition, $A_{OEF} = A_{ji}g_0$. For the GPE experiment the ground state population is equal to the average neutral density between the plasma and the wall, $n_j = n_1 = 7.33 \times 10^{13}\ cm^{-3}$. For the case where radiation trapping is not necessary, $n_j = n_1 = 0$, $g_0 = 1$ and the Fortran code exits the OEF loop, moving on to solving for the population densities. This step essentially skips the OEF step in the flow chart displayed in Figure 6.7. The OEF is applied to the 1^1S→n^{1}P states (n= 2, 3, …, n) or any state that terminates on the ground state. Table C1 in Appendix C is a detailed breakdown of each state configuration from the ground state and the respective wavelengths.

Figure 6.8 is the OEF and no-OEF calculated line emission, ε_λ, of the three He I lines (667.9, 706.5, 728.0 nm) at a plasma $T_e \sim 3.00\ eV$ as a function of the electron density. The line emission is related to the line intensity by $\varepsilon_\lambda = I_\lambda n_e$. This figure directly illustrates the effects of the helium neutral density found in Proto-MPEX, for the gas penetration experiment, on the calculated intensities. The inclusion of radiation trapping increases the emissivity and hence the intensity of $667.90\ nm$ and $728.00\ nm$ lines This is due to the fact that both lines lower state population is the 2^1P, which directly terminates on the ground state. Due to the decrease in the 2^1P state's Einstein coefficient by the OEF, an increase in the population of the 2^1P state occurs, resulting in an increase in the calculated I_{667} and I_{728}.

I_{706} is not as affected by the radiation trapping because it is a triplet state transition. The *Pauli's exclusion principle* states that two electrons in the same state cannot have the same spin, so the ground state electrons have opposite or anti-parallel spins. The triplet states involve promoting the excited electron's spin parallel to the ground state's electron's spin; therefore, the triplet state excitation level is no longer paired to the ground state. Swapping spins during a transition is considered 'forbidden', decreasing the probability that a triplet transition will occur when radiation is absorbed. 'Forbidden' transitions are not likely to occur between the singlet and triplet states.

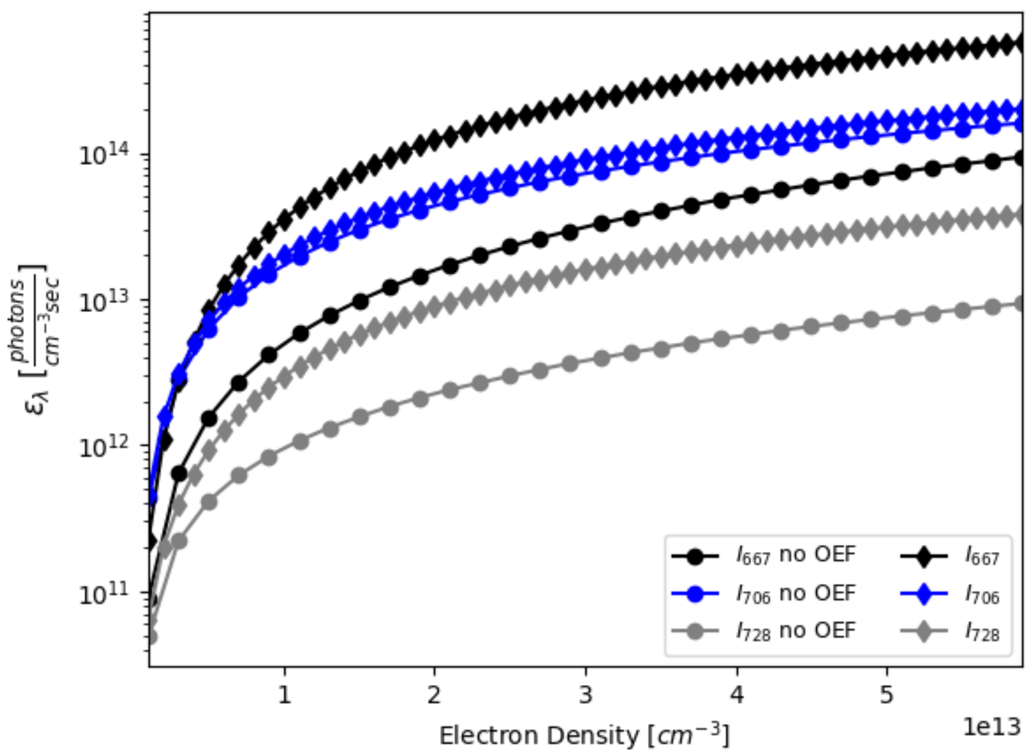

Figure 6.8. Calculated Intensities from the OEF-CRM and no-OEF CRM.

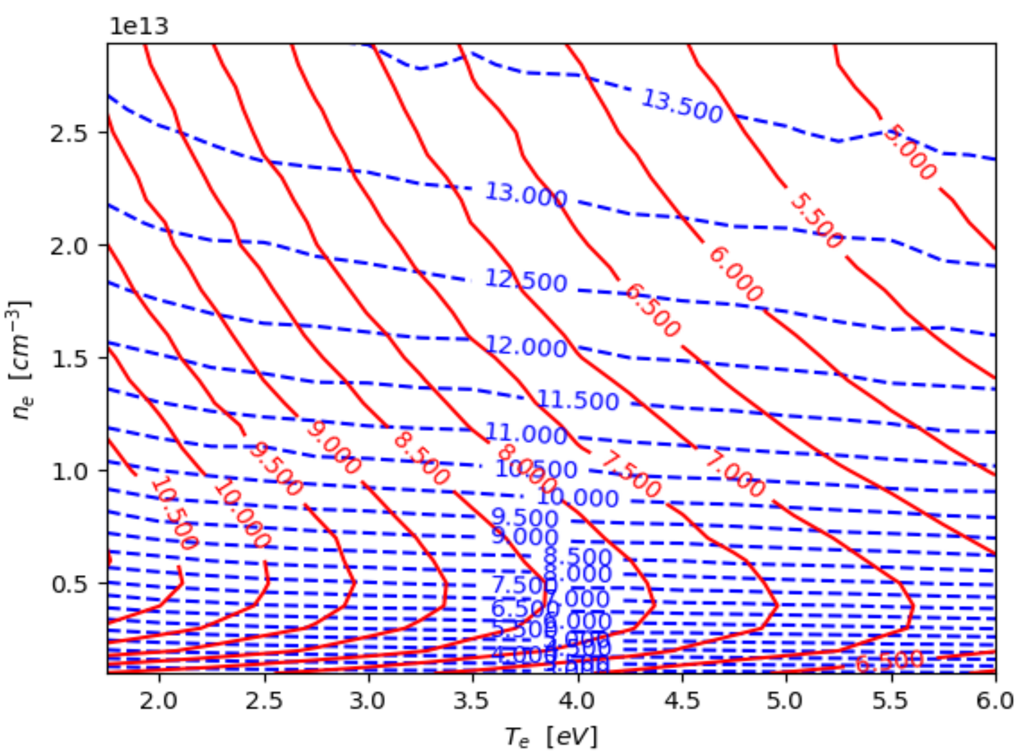

Figure 6.9. OEF Modified CRM Contour of Intensity Ratios

Referring back to Figure 6.6 with the information in Figure 6.8 one can see clearly the effects on the density and temperature dependent ratios that the radiation trapping has. Due to the increase in I_{667} and I_{728} the new contours of temperature and density dependent ratios, Figure 6.9, are the inverse of Figure 6.6. This change in calculated values can have a significant impact on the derived T_e and n_e values from the HELIOS diagnostic. If the spectrometer is measuring light intensity that is altered by the neutral helium density in the system, i.e. altered due to radiation trapping, then this needs to be accounted for in the calculated intensities. As can be seen in Figure 6.9, the calculated temperature dependent ratios, for the lower temperature plasmas and $2.00 \times 10^{13}\ cm^{-3}$ densities, are over 2.5 times less than in the no-OEF case, and the density dependent ratios are over 2.0 times higher than in the no-OEF case.

A good indicator that the radiation trapping has been applied correctly is to compare it to literature. D. Nishijima has used the OEF method to account for radiation trapping in a collisional radiative model. In the study performed, the experiment was on a helium plasma in Pisces-A and Dr. M. Goto's collisional radiative code was used. The experimental applications of the OEF is not an ideal comparison due to Proto-MPEX generating a deuterium plasma and the helium is injected through a nozzle; however, the model modification, therefore the calculated ratios, should have a similar trend if the OEF method is being applied correctly. Table 6.1 displays the temperature and density dependent ratios for D. Nishijima and the CRM in this study (H. B. Ray) for both radiation trapping and without radiation trapping. D. Nishijima's literature applications do not extend to the densities found in Proto-MPEX, so the comparison are done at a lower density, $3.00 \times 10^{12}\ cm^{-3}$, at a similar temperature found in Proto-MPEX, $3\ eV$.

The bottom two rows in Table 6.1 is the "no radiation trapping" comparison, which is done to set a standard for the radiation trapping comparison. The density dependent ratios are very similar, whereas, the temperature dependent ratios differ by about 2.5 for the chosen density and temperature. To further assess the two models together the ratios for D. Nishijima were used to derive T_e and n_e values from the ORNL CRM in this study. For the ratios shown in the bottom two rows for D. Nishijima the ORNL CRM returns $T_e = 2.43\ eV$ and $n_e = 1.49 \times 10^{12}\ cm^{-3}$. These values are not far off from the $T_e = 3.00\ eV$ and $n_e = 3.00 \times 10^{12}\ cm^{-3}$. The discrepancy could be caused by several differences between the two models, but the purpose of the comparison was to set a standard between the two models so that the radiation trapping modification could be properly assessed.

The middle two rows in Table 6.1 are the radiation trapping ratios. The temperature dependent ratio is ~ 0.5, and the density dependent ratio is > 5 different than the D. Nishijima ratios. This difference in the density dependent ratios are higher than expected from what is known by the original model comparison. The values returned for these ratios by the ORNL OEF CRM are $T_e = 6.41\ eV$ and $2.53 \times 10^{12}\ cm^{-3}$. Whereas the density values are once again not far off, the temperature values have too much of a discrepancy to disregard. This result raised questions whether the OEF method modification was being implemented correctly in the ORNL OEF CRM. Further investigation was done by comparing the g_0 values for the $1^1S \rightarrow 2^1P$ transition directly for different k_0R (absorption coefficient times the characteristic length of the system) in Figure 6.10. Values of g_0 are extracted from figure 8.12 in Takashi Fujimoto's Plasma Spectroscopy, and figure 4 from D. Nishijima's *Determination of the optical escape factor in the He I intensity ratio technique applied for weakly ionized plasmas* for comparison to the values generated in the ORNL OEF CRM. As can be seen in Figure 6.10 the g_0 values generated by the ORNL OEF CRM are consistent with the values extracted from Fujimoto's Plasma Spectroscopy, and the D. Nishijima g_0 values range between a factor of 1.67 to 4.22 lower. Since the desired radiation trapping modification is the OEF method described in Fujimoto's Plasma Spectroscopy this is a reassuring result that the ORNL OEF CRM is properly applying the OEF method for radiation trapping. The following section will use the ORNL OEF CRM described to re-assess the data from Proto-MPEX.

TABLE 6.1. COMPARISON BETWEEN D NISHIJIMA OEF AND H. B. RAY APPLICATION FOR $N_E = 3.00 \times 10^{12} cm^{-3}$ AT T_E=3 EV.		
Author	**H. B. Ray**	**D. Nishijima**
Ratios with Radiation Trapping		
R_{T_e}	5.75	~6.25
R_{n_e}	11.00	~5.60
Ratios without Radiation Trapping		
R_{T_e}	12.56	~10.00
R_{n_e}	2.92	~2.10

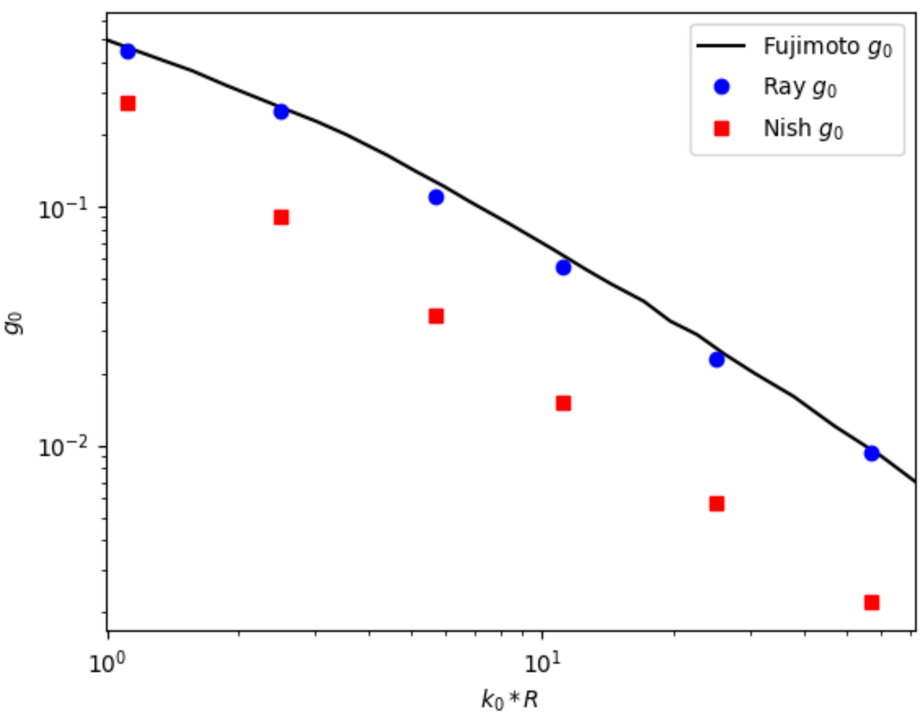

Figure 6.10. Optical Emission Factor (g_0) as a function of absorption coefficient times the characteristic length (k_0R) from Fujimoto book D. Nishijima paper, and this study (Ray).

6.3 Testing Radiation Trapping Hypothesis with Proto-MPEX Gas Penetration Experimental Data

The gas penetration experimental data covered in Chapter 5 was re-analyzed using the new OEF ORNL CRM. Figure 6.11 displays the HELIOS measured electron temperature and density using the OEF ORNL CRM. Also, shown is the on-axis and separate day radial scan DLP measured electron temperature and density. The DLP was inserted horizontally into Proto-MPEX, whereas, the gas puff for HELIOS enters vertically. The on-axis DLP measured data is denoted by the magenta circle, the radial scan DLP data is denoted by black circles, and the HELIOS data is denoted by the square markers.

Comparison between the DLP electron temperature and HELIOS electron temperature using the OEF ORNL CRM is in far better agreement than when using the standard ORNL CRM. Temperatures inferred from HELIOS have decreased by a factor of ~3.00, bringing the HELIOS measured T_e values within the range of the DLP value. This change in HELIOS measured T_e suggests that the neutral density in the Proto-MPEX system was causing radiation trapping of the

$1^1S \rightarrow 2^1P$ transition, which directly alters the population of the 667.90 nm ($3^1D \rightarrow 2^1P$) and the 728.00 nm ($3^1S \rightarrow 2^1P$). Similarly, the HELIOS measured n_e values were decreased roughly by a factor of ~6.00, bringing the HELIOS electron density values down from their previous perceived over-estimation. Error bars on the HELIOS measured T_e and n_e further supports that accounting for radiation trapping in the CRM using the OEF method for the high neutral density case is important physics to be included in the model.

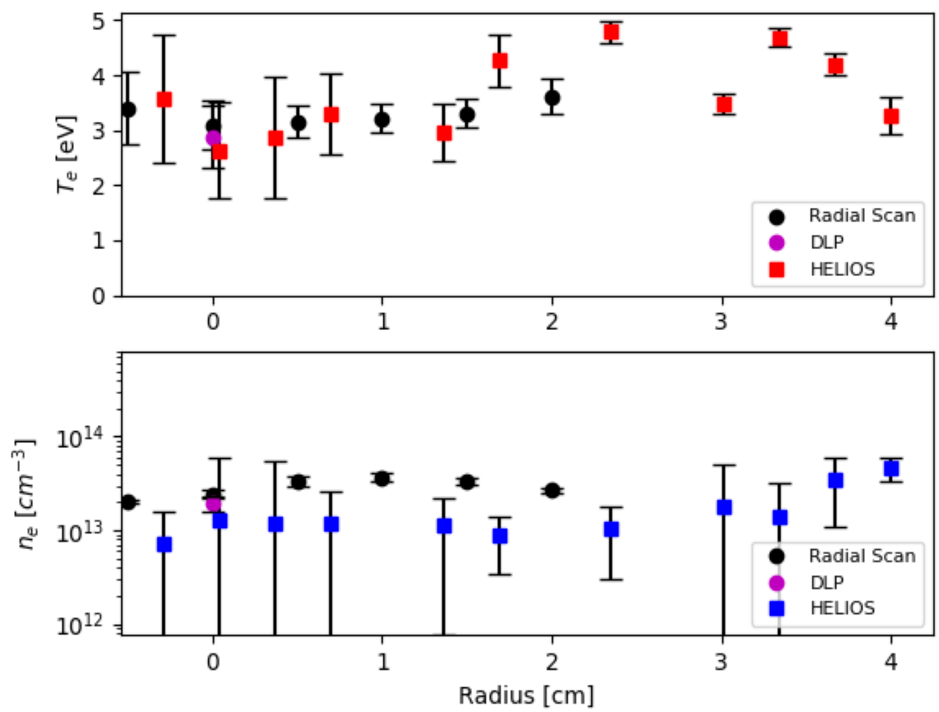

Figure 6.11. HELIOS Measured T_e and n_e as Compared to on-Axis DLP measured T_e and n_e.

6.4 Uncertainty Analysis for HELIOS

The uncertainty in the HELIOS values is a complex propagation of the error through the measured and modeled ratios. Equation 6.3.1,[32] equation 6.3.2,[32] and equation 6.3.3 are the model calculated, experimentally measured, and final uncertainty in the line intensity ratios, respectively.

$$\sigma_R^{mod} = \pm R^{mod} \sqrt{\left(\frac{\sigma_{A_{ji}}}{A_{ji}}\right)^2 + \left(\frac{\sigma_{A_{ki}}}{A_{ki}}\right)^2 + 2 * (0.05)^2(1 - 0.95)} \qquad Equation\ 6.3.1$$

$$\sigma_R^{exp} = \pm R^{exp} \sqrt{\left(\frac{\sigma_a}{I^a}\right)^2 + \left(\frac{\sigma_b}{I^b}\right)^2} \qquad Equation\ 6.3.2$$

$$\sigma_R = \pm \sqrt{\left(\sigma_R^{exp}\right)^2 + \left(\sigma_R^{mod}\right)^2} \qquad Equation\ 6.3.3$$

In the above equations, A_{ji} and A_{ki}, are the Einstein coefficients of spontaneous emission for the numerator and denominator of the respective ratios and $\sigma_{A_{ji}}$ and $\sigma_{A_{ki}}$ are their uncertainties. R^{exp} and R^{mod} are the experimentally and model determined ratios. I^a and I^b are the experimentally measured intensities of the respective ratio and σ_a and σ_b are their uncertainties. The CRM ratios and experimental ratios are used to determine the HELIOS measured T_e and n_e. In order to determined σ_{T_e} and σ_{n_e} the set of ratios corresponding to the T_e and n_e are plotted as a function of their dependence as shown in Figure 6.12, i.e. R_{n_e} is plotted as function of n_e for the corresponding T_e.

The R_{n_e} of interest (from my dataset) is then added to the plot with the respective uncertainty, $R_{n_e} \pm \sigma_{R_{n_e}}$. The uncertainty in the measured values is the difference between where the caps of the error bars intersect the ratio curve and the original value as shown by the dotted lines in Figure 6.12. The complexity of the uncertainty is represented strongly by the electron density. The majority of their error bars are not symmetric. For example, the electron density value third from the left in Figure 6.11 has a larger negative error bar than positive. This is due to the ratio curves and is demonstrated in Figure 6.12.

6.5 Modeling Summary

This chapter concluded that the CRM being used must have the proper atomic physics accounted for in order to accurately infer the T_e and n_e values of the plasma column. Due to the increased neutral helium density in the Proto-MPEX system (plasma and chamber) radiation trapping of the 667.90 and 728.00 nm emission lines ($3^1S \rightarrow 2^1P$ and $3^1D \rightarrow 2^1P$ singlet transitions, respectively) was occurring between the plasma and the collection optics at the wall. The ORNL CRM was modified to account for radiation trapping, using the OEF method. This new CRM, denoted the ORNL OEF CRM, was used to re-analyze the GPE experimental data. The inferred T_e values from the ORNL OEF CRM are very consistent with the DLP data supporting the conclusion that radiation trapping needed to be accounted for in the CRM. Furthermore, the density values were significantly decreased from their overestimation ($> 1 \times 10^{14}\ cm^{-3}$) using the ORNL CRM and the core value is consistent with the DLP data from the scan and the day of the GPE.

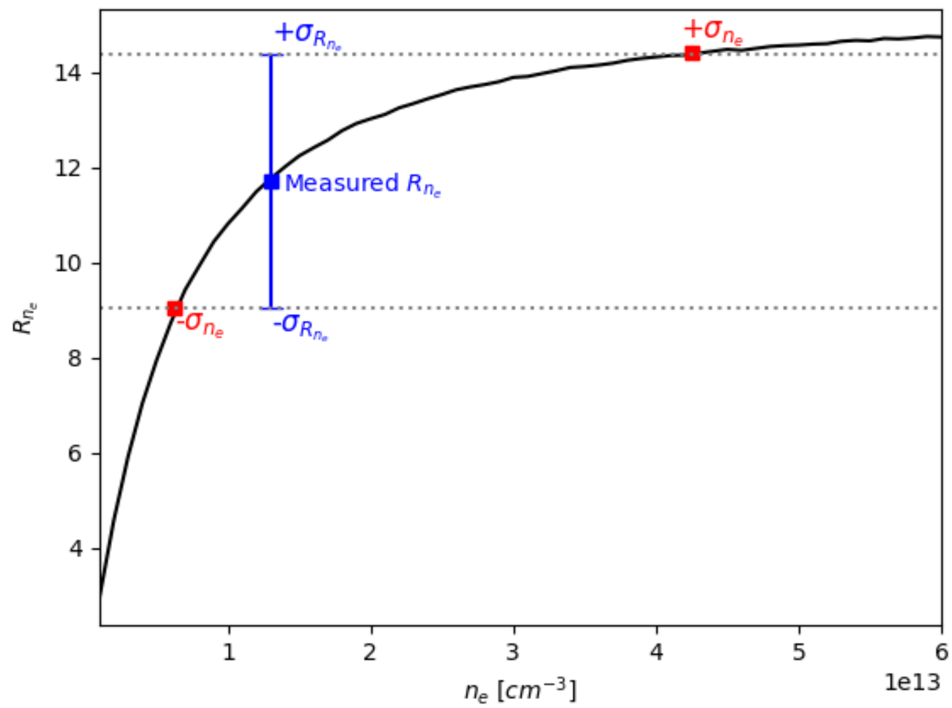

Figure 6.12. Uncertainty Analysis for the HELIOS Measured $n_e = 1.3e13\ cm^{-3}$ at $T_e = 2.65$ eV

Chapter 7 Future Work and Conclusion

7.1 Hardware Future Work

The penetration of the gas puff into the plasma column turned out to be an exceptionally limiting parameter for the gas puffed HELIOS diagnostic. Due to the high densities ($>$ $2 \times 10^{13}\ cm^{-3}$) of the Proto-MPEX core, the gas puff and hence HELIOS measurements of T_e and n_e were localized to the edge of the plasma column. This constraint on the diagnostic would not allow for the necessary measurement at the source region or T_e and n_e profiles of the plasma as the TS and DLPs offer.

Puffed HELIOS could potentially be modified to allow for radial scans of the plasma column in similar machines to Proto-MPEX. Equation 5.5.1 describes the penetration depth of the gas puff as a function of the plasma density, ionization rate coefficient, and the gas velocity. The gas velocity is dependent on the gas temperature and if one were to increase the velocity of the gas then the gas would theoretically penetrate further into the plasma column. The TS n_e profile shown in Chapter 5 is used to generate a contour plot of the d_g as a function of the gas temperature (T_g) and the radius of the plasma. For the calculation of d_g the ionization rate coefficient for the n=3 level was used due to the 667.9 nm and 728.0 nm singlet states having upper levels of 3^1S and 3^1D.

Figure 7.1 includes the contour of the gas depths in the top image and the densities that correspond to each depth in the smaller subplot at the bottom. A spline fit is performed on the n_e data (shown in Figure 7.1 as a red trace). The x-axis of both images in Figure 7.1 starts at the plasma edge on the right-hand-side and ends slightly past the core of the plasma on the left-hand-side. For room temperature (400 K), which is the temperature assumed for the gas in this thesis, even at the edge of the plasma column the value of d_g equals ~1.0 cm for the lowest density value. This value quickly falls off to less than 0.3 cm as the density increases an order of magnitude. The increase in T_g clearly affects the d_g in the edge of the plasma, but as the density increases moving further into the plasma column d_g remains less than 1.0 cm. This information may be deterring, but there are factors not included in this modeling of d_g that could potentially make puffed HELIOS a competitive diagnostic for machines like Proto-MPEX. For example, the emissivity profile shown in Figure 5.14 has the gas puff reaching 2 cm into the plasma column which is twice the value determined by the model. This discrepancy could be due to the amount of gas puffed into the system. The amount of gas puffed into the system for the preliminary data in Chapter 5 could have been enough to avoid perturbation but penetrate just that much more into the plasma column.

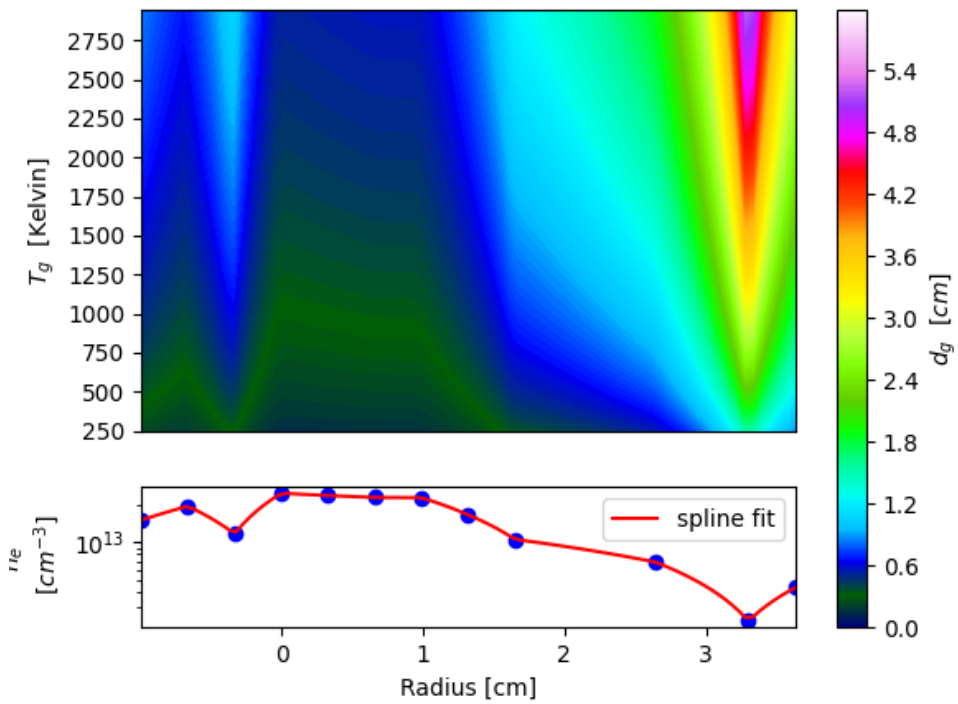

Figure 7.1. Contour of the gas depth as a Function of T_g and r(ne).

Dedicated experiments would need to be performed to test the increased gas temperature hypothesis in a device similar to Proto-MPEX. Increasing T_g would increase the pressure in the plenum and this would need to be properly regulated and maintained. Figure 7.2 shows how the pressure would change in the UW-M plenum used in this thesis if all values except for T_g were maintained. The increase in gas temperature that is shown in Figure 7.1 would bring the pressure in the chamber greater than 1 million Pascal, which is higher than a compressed air cylinder (rated at 125 psi – 150 psi). Along with the pressure in the gas plenum is the gas dynamics of the system after increasing T_g. When the temperature of the gas is increased so is the velocity and this affects more than the depth of the gas puff. The Reynolds number (Re) is proportional to the gas velocity and as Re increases the chances that the gas is turbulent increases especially if the gas velocity is increased by three orders of magnitude. Careful experimentation should be performed to test the possibility of using higher temperature gas puffed HELIOS on a linear device with high core densities.

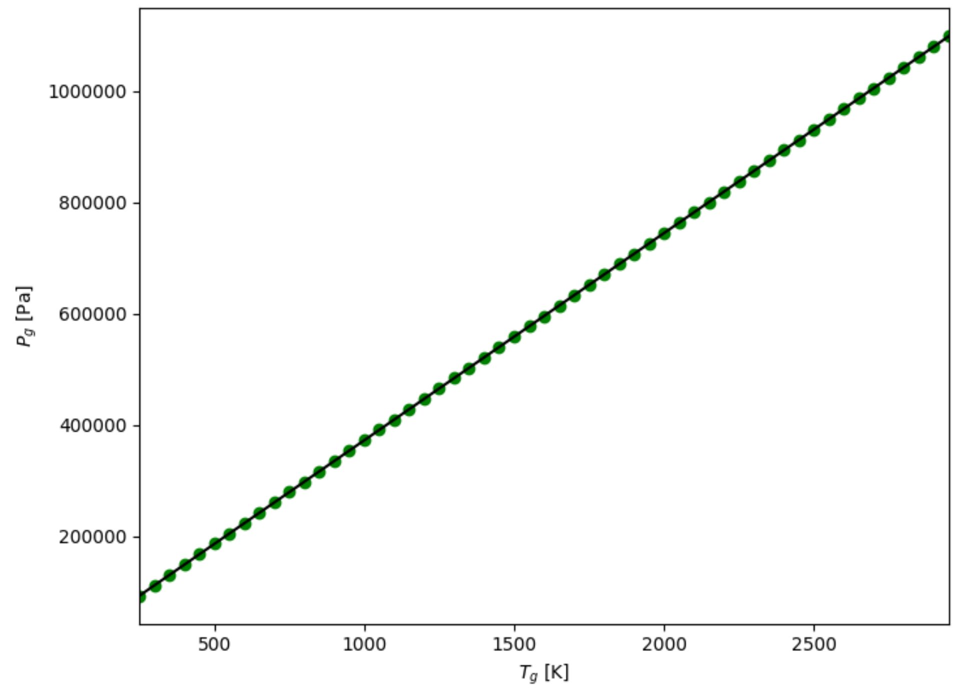

Figure 7.2. Pressure increase in the UW-M plenum as T_g is increased.

The UW-M gas injection system, if port allocation is available, would be the best system to perform future work experiments on a device like Proto-MPEX. Chapter 3 calculations and data show that the UW-M gas injection system has an improved conductance to the PV-10. This means that the gas exits the UW-M nozzle within $0.42\ ms$, allowing for quick, consecutive gas puffs in the plasma column. The UW-M gas injection system can also be place within the vacuum vessel as long as the TZM nozzle is properly protected from the radiofrequency waves. Furthermore, the UW-M gas injection system can be operated at pressures $< 35\ mbar \approx 0.51\ psia$ to improve the gas divergence from 120º to 20 º. This means that the gas puff has the potential to be a thin localized beam across the plasma radius.

7.2 Plasma and Atomic Physics Future Work

HELIOS could potentially be used for future plasma physics analysis on machines like MPEX. Important physics to machines like MPEX would be source adjacent measurements of T_e and n_e. This would allow for two-point modelling between the source and the target,[20] power accountability at the source,[54] and $\frac{S}{XB}$ impurity and transport analysis.[17,71]

Two-point modelling in a linear device allows scientists to make a connection between the source T_e values and the target T_e values. This connection between the target and source values would allow models to predict what happens at the target when the source parameters are altered. Power accountability near the source can help operators understand how the source power is being injected in the machine. If there is power loss near the source location, measurements of T_e and n_e at the source location are valuable to understanding this power loss. Finally, $\frac{S}{XB}$ impurity and transport analysis would allow scientists to understand the radiative loss due to impurities at the source and if impurities from the source region are being deposited at the target.

Having consistent measurements of T_e at the source in MPEX or future devices would contribute to understanding machine operating conditions and allow for scientists to adjust for specific parameters at the target. DLPs have been shown to perturb the plasma too much when inserted adjacent to the helicon, making HELIOS a viable alternative to measuring T_e and n_e at the source.

An atomic physics experiment could potentially be performed with HELIOS as well. If a source (helicon, ECH/EBW, and/or ICH) is producing hot electrons in the plasma then the electron energy distribution function (EEDF) is no longer Maxwellian.[8] This would make any diagnostic that assumes a Maxwellian EEDF inaccurate. The atomic data in HELIOS could be adjusted, using hot electron assumption of the EEDF,[8] to test and understand source adjacent measurements of T_e and n_e.

7.3 Conclusion

The underlying theme of the presented doctoral work was motivated by the advantage's MCF poses to the environment and society as compared to large MW light water and boiling water fission reactors. One of the hurdles of MCF is the turbulence and ELMS, which cause confinement instabilities that endanger the PFCs. This is both a materials problem and a plasma physics question. The electron temperature and density profiles can relay important information to physicists about these instabilities in the plasma, making diagnostics that measure electron temperature and density with high time resolution very valuable to the fusion community. To bridge the gap between a working fusion power reactor and the current state of technology, linear devices need to be employed with dedicated PMI experiments. Linear devices have a lower operational cost and an open capacity for diagnostics. Proto-MPEX, a radio frequency source, is one such device that is great for testing a diagnostic that can measure T_e and n_e with high time resolution.

HELIOS is a helium line ratio diagnostic that utilizes neutral helium lines to measure the electron temperature and density in a plasma. Neutral helium gas is puffed into the plasma column and optics are used to collect the light emitted from the collisional and radiative processes for specific helium lines of interest ($I_{667.90}$, $I_{706.53}$, and $I_{728.00}$). The light is transferred by fiber optics to a Filterscope radiometer and a McPherson spectrometer, where high time resolution (100 kHz) and spectrally resolved measurements are made, respectively. The measured ratios of the helium line intensities are compared to a CRM's calculated helium line ratios. The ratios dependence on electron temperature, $R_{T_e} = \frac{I_{706.53}}{I_{728.00}}$, and density, $R_{T_e} = \frac{I_{667.90}}{I_{728.00}}$, allow for the measurement of the plasma T_e and n_e. The CRM calculates the ratios by utilizing rate coefficients of specific transitions of the helium's electrons.

With the use of the filterscope, digitization rates up to 1 MHz can be achieved. Edge turbulence events occur between frequencies of 10 kHz and 1 MHz, making the Filterscope HELIOS diagnostic a viable turbulence monitoring system. HELIOS has an advantage over fast probes because it utilizes spectroscopy and neutral helium, which will not perturb the plasma through material sputtering and transport the same way that a probe would. HELIOS is also not limited to a specific time range and can be used for longer durations in the plasma. Probes are limited to short periods of time to avoid damage to the probe and introduction of impurities into the plasma. When compared to TS, HELIOS is less expensive and allows for more control of installation. The laser required for TS is very expensive to maintain, align, and keep safe. HELIOS as a T_e and n_e diagnostic offers a great alternative or cross-referencing diagnostic to DLPs and TS.

HELIOS has been used on tokamaks such as TEXTOR and ASDEX-U ($2.0 \times 10^{12}\ cm^{-3} < n_e < 2.0 \times 10^{13}\ cm^{-3}$ and $10\ eV < T_e < 250\ eV$). The experiments performed have been focused on advancing the diagnostic through improving atomic data, understanding the dominate helium transitions in the plasma column, and improving the gas puffing system. HELIOS has also been used on helium linear devices ($1.0 \times 10^{9} \leq n_e \leq 1.0 \times 10^{13}\ cm^{-3}, 5.0\ \leq T_e\ \leq 20\ eV$).

The development of HELIOS on Proto-MPEX involved exhaustive testing of the gas puffing systems, which fueled the plasma and introduced the neutral helium into the deuterium plasma. The gas injection of the fueling puffers as compared to the particles injected by the HELIOS puffers were on the same order of magnitude, which implies that non-perturbing HELIOS measurements will be difficult to accomplish in Proto-MPEX. Non-perturbing validation experiments were successfully completed and concluded that the helium emission from the gas puff was localized to the plasma edge. The high electron density of the deuterium plasma in Proto-MPEX ($> 2 \times 10^{-13}\ cm^{-3}$) was deterring the gas puff from penetrating into the plasma core, localizing the helium line emission to the edge. Increased density of the gas puff allowed for the He I particles to reach the plasma core for analysis. Inconsistencies between DLP data and HELIOS derived T_e and n_e concluded that some atomic physics was not accounted for in the ORN CRM.

The background neutral pressures and hence neutral densities of helium ($> 3.00 \times 10^{12}\ cm^{-3}$), caused radiation trapping of the singlet line transitions ($3^1D \rightarrow 2^1P$ and $3^1S \rightarrow 2^1P$) to occur between the plasma and the collection optics. This required that the Oak Ridge National Laboratory (ORNL) collisional radiative model (CRM) be modified to account for the radiation trapping atomic physics. The optical escape factor (OEF) method was used to account for the radiation trapping in the CRM. The OEF ORNL CRM was tested when the background neutral pressure in the vacuum vessel of Proto-MPEX was increased to reach the plasma core. Re-analysis of the experimental data, using the OEF ORNL CRM, concluded that the ambient neutral pressure in Proto-MPEX was significant factor in HELIOS measurements of T_e and n_e. Radiation trapping is a critical inclusion to the atomic physics in order to to accurately measure T_e and n_e.

References

(1) Unterberg, E. A.; Schmitz, O.; Fehling, D. H.; Stoschus, H.; Klepper, C. C.; Munoz-Burgos, J. M.; Van Wassenhove, G.; Hillis, D. L. HELIOS: a helium line-ratio spectral-monitoring diagnostic used to generate high resolution profiles near the ion cyclotron resonant heating antenna on TEXTOR. *Rev Sci Instrum* **2012**, *83*, 10D722.

(2) Rapp, J., Lumsdaine, A., Beers, C. J., Biewer, T. M., Bigelow, T. S., Caneses, J. F., ... & Lindquist, E. Latest results from Proto-MPEX and the future plans for MPEX. *Fusion Science and Technology* **2019**, *75*, 654-663.

(3) Colchin, R. J.; Hillis, D. L.; Maingi, R.; Klepper, C. C.; Brooks, N. H. The Filterscope. *Review of Scientific Instruments* **2003**, *74*, 2068-2070.

(4) DIII-D tokamak @ General Atomics. https://www.pinterest.com/pin/325736985518733478/.

(5) Hellwig, M. Influence of 3D geometry and surface roughness on plasma-wall interaction processes on tungsten surfaces. Ruhr-Universität Bochum, 2016.

(6) Schmitz, O.; Beigman, I. L.; Vainshtein, L. A.; Schweer, B.; Kantor, M.; Pospieszczyk, A.; Xu, Y.; Krychowiak, M.; Lehnen, M.; Samm, U.; Unterberg, B. Status of electron temperature and density measurement with beam emission spectroscopy on thermal helium at TEXTOR. *Plasma Physics and Controlled Fusion* **2008**, *50*.

(7) Griener, M.; Schmitz, O.; Bald, K.; Bosser, D.; Cavedon, M.; De Marne, P.; Eich, T.; Fuchert, G.; Herrmann, A.; Kappatou, A.; Lunt, T.; Rohde, V.; Schweer, B.; Sochor, M.; Stroth, U.; Terra, A.; Wolfrum, E.; Team, A. U. Fast piezoelectric valve offering controlled gas injection in magnetically confined fusion plasmas for diagnostic and fuelling purposes. *Rev Sci Instrum* **2017**, *88*, 033509.

(8) Sasaki, S., Takamura, S., Watanabe, S., Masuzaki, S., Kato, T., & Kadota, K. Helium I line intensity ratios in a plasma for the diagnostics of fusion edge plasmas. *Review of scientific instruments* **1996**, *67*, 3521-3529.

(9) Boivin, R. F.; Kline, J. L.; Scime, E. E. Electron temperature measurement by a helium line intensity ratio method in helicon plasmas. *Physics of Plasmas* **2001**, *8*, 5303-5314.

(10) Unterberg, E. A., Davda, K. M., Neff, A. L., Ray, H. R., & Fehling, D. T. . *The Filterscope: A Technical Guide & User's Manual*: ORNL Technical Report No2019.

(11) Nishijima, D.; Hollmann, E. M. Determination of the optical escape factor in the He I line intensity ratio technique applied for weakly ionized plasmas. *Plasma Physics and Controlled Fusion* **2007**, *49*, 791-802.

(12) Shin Kajita, D. N., Eric M. Hollmann, and Noriyasu Ohno. Ray tracing simulations for radiation trapping of the He I resonance transitions in a linear plasma device. *Physics of Plasmas* **2009**, *16*, 063303.

(13) Bonnin, X., & Coster. Full-tungsten plasma edge simulations with SOLPS. *Journal of nuclear materials* **2011**, *415*, S488-S491.

(14) Naujoks, D., Behrisch, R., Coad, J. P., & De Kock, L. C. J. M. Material transport by erosion and redeposition on surface probes in the scrape-off layer of JET. *Nuclear fusion* **1993**, *33*, 581.

(15) Maingi, R., Owen, L. W., Colchin, R. J., & Fenstermacher, M. E. Modeling of 2-D Neutral Density Measurements in DIII-D. *In Controlled Fusion and Plasma Physics* **1999**, *23*.

(16) Loch, S. D.; Ludlow, J. A.; Pindzola, M. S.; Whiteford, A. D.; Griffin, D. C. Electron-impact ionization of atomic ions in the W isonuclear sequence. *Physical Review A* **2005**, *72*.

(17) Johnson, C. A.; Loch, S. D.; Ennis, D. A. ColRadPy: A Python collisional radiative solver. *Nuclear Materials and Energy* **2019**, *20*.

(18) O. Auciello, D. F.: *Plasma Diagnostics: Dishcarge parameters and chemistry*; Academic Press, 2013; Vol. 1.

(19) Claeyssens, F. Fundamental studies of pulsed laster ablation. 2001.

(20) Stangeby, P. C.: *The Plasma Boundary of Magnetic Fusion Devices*; Taylor & Francis Group, LLC: New York, NY, 2000.

(21) Biewer, T. M. Electron Thermal Transport in the Madison Symmetric Torus. 2002.

(22) Hutchinson, I. H. Principles of plasam diagnostics: second edition. *Plasma Physics and Controlled Fusion* **2002**, *44*, 2603.

(23) McLean, A. G.; Soukhanovskii, V. A.; Allen, S. L.; Carlstrom, T. N.; LeBlanc, B. P.; Ono, M.; Stratton, B. C. Conceptual design of a divertor Thomson scattering diagnostic for NSTX-U. *Rev Sci Instrum* **2014**, *85*, 11E825.

(24) Banerjee, S.; Zushi, H.; Nishino, N.; Nagashima, Y.; Hanada, K.; Ishiguro, M.; Ryoukai, T.; Tashima, S.; Inoue, T.; Nakamura, K.; Idei, H.; Hasegawa, M.; Fujisawa, A.; Matsuoka, K. Fast visible imaging and edge turbulence analysis in QUEST. *Rev Sci Instrum* **2012**, *83*, 10E524.

(25) Carreras, B. A. Plasma edge cross-field transport: experiment and theory. *Journal of Nuclear Materials* **2005**, *337-339*, 315-321.

(26) Krasheninnikov, S. I.; D'Ippolito, D. A.; Myra, J. R. Recent theoretical progress in understanding coherent structures in edge and SOL turbulence. *Journal of Plasma Physics* **2008**, *74*, 679-717.

(27) Zweben, S. J. Search for coheret structure within tokamak plasma turbulence. *The Physics of fluids* **1985**, 974-982.

(28) Bleuel, J., Endler, M., Niedermeyer, H., Schubert, M., & Thomsen, H. The spatial structure of edge fluctuations in the Wendelstein 7-AS stellerator. *New Journal of Physics* **2002**, *4*, 38.31-38.38.

(29) Fenzi, C.; Fonck, R. J.; Jakubowski, M.; Mc Kee, G. R. 2D turbulence imaging in DIII-D via beam emission spectroscopy. *Review of Scientific Instruments* **2001**, *72*, 988-991.

(30) Zweben, S. J., Maqueda, R. J., Stotler, D. P., Keesee, A., Boedo, J., Bush, C. E., ... & Maingi, R. High Speed Imaging of Edge Turbulence in NSTX. *Nuclear Fusion* **2003**, *44*, 134.

(31) Rudakov, D. L.; Boedo, J. A.; Moyer, R. A.; Lehmer, R. D.; Gunner, G.; Watkins, J. G. Fast electron temperature diagnostic based on Langmuir probe current harmonic detection on DIII-D. *Review of Scientific Instruments* **2001**, *72*, 453-456.

(32) Rudakov, D. L., Boedo, J. A., Moyer, R. A., Krasheninnikov, S., Leonard, A. W., Mahdavi, M. A., ... & West, W. P. Fluctuation-driven transport in the DIII-D boundary. Plasma physics and controlled fusion. *Plasma Physics and Controlled Fusion* **2002**, *44*, 717.

(33) Boedo, J. A.; Gray, D.; Conn, R. W.; Luong, P.; Schaffer, M.; Ivanov, R. S.; Chernilevsky, A. V.; Van Oost, G. On the harmonic technique to measure electron temperature with high time resolution. *Review of Scientific Instruments* **1999**, *70*, 2997-3006.

(34) Turning the tables on turbulence. https://www.iter.org/newsline/-/2271.

(35) Plasma fingers point to the taming of the ELM. https://www.iter.org/newsline/229/1229.

(36) Zohm, H. Edge localized modes (ELMs). *Plasma Physics and Controlled Fusion* **1996**, *38*, 105.

(37) Kleva, R. G.; Guzdar, P. N. The impact of edge gradients in the pressure, density, ion temperature, and electron temperature on edge-localized modes. *Physics of Plasmas* **2011**, *18*.

(38) LeBlanc, B. P., Bell, R. E., Johnson, D. W., Hoffman, D. E., Long, D. C., & Palladino, R. W. . Operation of the NSTX Thomson scattering system. *Review of scientific instruments* **2003**, *74*, 1659-1662.

(39) Levinton, F. M., & Navratil, G. A. Multipoint Thomson Scattering. *Review of Scientific Instruments* **1983**, *54*, 35-40.

(40) iter. https://www.iter.org/.

(41) Hill, D. N.: *A review of ELMs in divertor tokamaks*: Lawrence Livermore National Lab., CA (United States), 1996.

(42) Brian Harold Bransden, J. J. C., J. Plivier Theodor: *Physics of atoms and molecules*; Pearson Education: India, 2003.

(43) Fujimoto, T. p.-. *Plasma spectroscopy*; Clarendon Press: Oxford, 2004.

(44) Muñoz Burgos, J. M.; Schmitz, O.; Loch, S. D.; Ballance, C. P. Hybrid time dependent/independent solution for the He I line ratio temperature and density diagnostic for a thermal helium beam with applications in the scrape-off layer-edge regions in tokamaks. *Physics of Plasmas* **2012**, *19*.

(45) Loch, S. D.; Burgos, J. M. M.; Ballance, C. P.; Ludlow, J.; Lee, T. G.; Fogle, M.; Pindzola, M. S.; Griffin, D. C.; Yumak, A.; Yavuz, I.; Altun, Z. Electron-impact ionization of atomic ions: Theoretical results. *Journal of Physics: Conference Series* **2009**, *194*.

(46) Loch, S. D.; Ballance, C. P.; Pindzola, M. S.; Stotler, D. P. The role of excited state ionization data on H and He generalized collisional–radiative coefficients. *Plasma Physics and Controlled Fusion* **2009**, *51*.

(47) Summers, H. P.; Dickson, W. J.; O'Mullane, M. G.; Badnell, N. R.; Whiteford, A. D.; Brooks, D. H.; Lang, J.; Loch, S. D.; Griffin, D. C. Ionization state, excited populations and emission of impurities in dynamic finite density plasmas: I. The generalized collisional–radiative model for light elements. *Plasma Physics and Controlled Fusion* **2006**, *48*, 263-293.

(48) Summers, H. P., & Hooper, M. B. On radiative power from impurities in plasmas. *Plasma Physics and Controlled Fusion* **1983**, *25*, 1311.

(49) OPEN-ADAS. https://open.adas.ac.uk/.

(50) Drake, G. W.: *Springer handbook of atomic, molecular, and optical physics*; Springer Science & Business Media, 2006.

(51) Brix, M.: *Messung von Elektronentemperatur und -dichte mittels Heliumstrahldiagnostik im Randschichtplasma eines Tokamaks*: Forschungszentrum Jülich., 1999.

(52) Rapp, J.; Biewer, T. M.; Bigelow, T. S.; Caneses, J. F.; Caughman, J. B. O.; Diem, S. J.; Goulding, R. H.; Isler, R. C.; Lumsdaine, A.; Beers, C. J.; Bjorholm, T.; Bradley, C.; Canik, J. M.; Donovan, D.; Duckworth, R. C.; Ellis, R. J.; Graves, V.; Giuliano, D.; Green, D. L.; Hillis, D. L.; Howard, R. H.; Kafle, N.; Katoh, Y.; Lasa, A.; Lessard, T.; Martin, E. H.; Meitner, S. J.; Luo, G. N.; McGinnis, W. D.; Owen, L. W.; Ray, H. B.; Shaw, G. C.; Showers, M.; Varma, V. Developing the science and technology for the Material Plasma Exposure eXperiment. *Nuclear Fusion* **2017**, *57*.

(53) Rapp, J. e. a. The development of plasma-material interaction facilities for the future of fusion technology. *Fusion Science and Technology* **2013**, 237-244.

(54) Showers, M.; Biewer, T. M.; Caughman, J. B.; Donovan, D. C.; Goulding, R. H.; Rapp, J. Heat flux estimates of power balance on Proto-MPEX with IR imaging. *Rev Sci Instrum* **2016**, *87*, 11D412.

(55) Beers, C. J.; Lindquist, E. G.; Biewer, T. M.; Caneses, J. F.; Caughman, J. B. O.; Goulding, R. H.; Kafle, N.; Ray, H.; Showers, M. A.; Zinkle, S. J.; Rapp, J. Characterization of

the helicon plasma flux to the target of Proto-MPEX. *Fusion Engineering and Design* **2019**, *138*, 282-288.

(56) Ray, H. B.; Biewer, T. M.; Fehling, D. T.; Isler, R. C.; Unterberg, E. A. Spectral survey of helium lines in a linear plasma device for use in HELIOS imaging. *Rev Sci Instrum* **2016**, *87*, 11E711.

(57) Beers, C. J., Goulding, R. H., Isler, R. C., Martin, E. H., Biewer, T. M., Caneses, J. F., ... & Rapp, J. Helicon plasma ion temperature measurements and observed ion cyclotron heating in proto-MPEX. *Physics of Plasmas* **2018**, *25*, 013526.

(58) piezosystemjena. https://www.piezosystem.com/.

(59) Bates, S. C.; Burrell, K. H. Fast gas injection system for plasma physics experiments. *Review of Scientific Instruments* **1984**, *55*, 934-939.

(60) Shesterikov, I.; Xu, Y.; Berte, M.; Dumortier, P.; Van Schoor, M.; Vergote, M.; Schweer, B.; Van Oost, G. Development of the gas-puff imaging diagnostic in the TEXTOR tokamak. *Rev Sci Instrum* **2013**, *84*, 053501.

(61) Parks, P. B.; Wu, W. Limitations of extended gas delivery tubes used for fuelling mitigated plasma disruptions, and a unique injection concept for prompt gas delivery. *Nuclear Fusion* **2011**, *51*.

(62) Tutorial on Gas Flow, Conductance, Pressure Profiles. https://indico.cern.ch/event/569714/contributions/2303871/attachments/1336491/2161880/JUAS_2017_-_Gas_Flow_Conductance_Pressure.pdf.

(63) Smith, C. G., & Lewin, G. Free molecular conductance of a cylindrical tube with wall sorption. *Journal of Vacuum Science and Technology* **1966**, *3*, 92-95.

(64) Senda, Y. Theoretical analysis of vacuum evacuation in viscous flow and its applications. *Atmosphere* **2010**, *100*, 0-1.

(65) Edgertronic. https://edgertronic.com.

(66) Cube-Mounted Pellicle Beamsplitters. https://www.thorlabs.com/newgrouppage9.cfm?objectgroup_ID=4138.

(67) Kafle, N.; Biewer, T. M.; Donovan, D. C. Dual-pass upgrade to the Thomson scattering diagnostic on the Prototype-Material Plasma Exposure eXperiment (Proto-MPEX). *Rev Sci Instrum* **2018**, *89*, 10C107.

(68) Parsons, A.: Photoionization, the Saha Equation, and Recombination. YouTube, 2014.

(69) Salzmann, D.: *Atomic physics in hot plasmas*; Oxford University Press on Demand, 1998.

(70) Menzel, M. H. H. D. H. Physical Processes in Gaseous Nebulae. X. Collisional Excitation of Nebulium. *Astrophysical Journal* **1940**, *92*, 408.

(71) Nishijima, D., Doerner, R. P., Baldwin, M. J., Pospieszczyk, A., & Kreter, A. Experimental determination of S/XB values of WI visible lines. *Physics of Plasmas* **2009**, *16*, 122503.

Appendices

Appendix A Derivation of the Unknown Volume (Equation 3.2.1)

$$(PV)_{initial} = nRT_{initial}\ ;\ \ (PV)_{final} = nRT_{final} \qquad Equation\ A.1, A.2$$

$$\frac{(PV)_{initial}}{(PV)_{final}} = \left[\frac{nRT_{initial}}{nRT_{final}}\right]\ ;\ \ T_{initial} = T_{final} \qquad Equation\ A.3$$

$$(PV)_{initial} = (PV)_{final} \qquad Equation\ A.4$$

PV is the pressure of the system times the volume of the system, so

$$PV = PV_{test} + PV_{box} \qquad Equation\ A.5$$

Substituting equation A.5 into equation A.4, yields.

$$[(PV)_{test} + (PV)_{box}]_{initial} = [(PV)_{test} + (PV)_{box}]_{initial} \qquad Equation\ A.6$$

$$(PV)_{test_{initial}} - (PV)_{test_{final}} = (PV)_{box_{final}} - (PV)_{box_{initial}} \qquad Equation\ A.7$$

$$V_{test}\left[P_{test_{initial}} - P_{test_{final}}\right] = V_{box}\left[P_{box_{final}} - P_{box_{inital}}\right] \qquad Equation\ A.8$$

Since the piezo box and plenum are brought to equilibrium with the vacuum chamber pressure.

$$P_{test_{final}} = P_{box_{final}} = P_{final} \qquad Equation\ A.9$$

$$V_{test} = V_{box}\left[\frac{P_{final} - P_{box_{initial}}}{P_{test_{initial}} - P_{final}}\right] \qquad Equation\ A.10$$

Appendix B Collisional Radiative Matrix in Matrix Notation Written out to the i=4 State

$$\begin{bmatrix} \frac{dn_1}{dt} \\ \frac{dn_2}{dt} \\ \frac{dn_3}{dt} \\ \frac{dn_4}{dt} \end{bmatrix} =$$

$$\begin{bmatrix} -n_e S_1 - \sum_{j\neq i}\left(A_{1\to j} + n_e F_{1\to j}\right) & \sum_{j\neq i}(A_{2\to 1} + n_e F_{2\to 1}) & \sum_{j\neq i}(A_{3\to 1} + n_e F_{3\to 1}) & \sum_{j\neq i}(A_{4\to 1} + n_e F_{4\to 1}) \\ \sum_{j\neq i}(A_{1\to 2} + n_e F_{1\to 2}) & -n_e S_2 - \sum_{j\neq i}\left(A_{2\to j} + n_e F_{2\to j}\right) & \sum_{j\neq i}(A_{3\to 2} + n_e F_{3\to 2}) & \sum_{j\neq i}(A_{4\to 2} + n_e F_{4\to 2}) \\ \sum_{j\neq i}(A_{1\to 3} + n_e F_{1\to 3}) & \sum_{j\neq i}(A_{2\to 4} + n_e F_{2\to 4}) & -n_e S_3 - \sum_{j\neq i}\left(A_{3\to j} + n_e F_{3\to j}\right) & \sum_{j\neq i}(A_{4\to 2} + n_e F_{4\to 2}) \\ \sum_{j\neq i}(A_{1\to 4} + n_e F_{1\to 4}) & \sum_{j\neq i}(A_{2\to 4} + n_e F_{2\to 4}) & \sum_{j\neq i}(A_{3\to 4} + n_e F_{3\to 4}) & -n_e S_4 - \sum_{j\neq i}\left(A_{4\to j} + n_e F_{4\to j}\right) \end{bmatrix} \begin{bmatrix} n_1 \\ n_2 \\ n_3 \\ n_4 \end{bmatrix}$$

Appendix C Table of Transitions from the Ground State

Table 4.1.B Electron Configuration of the Ground State Transitions and their Respective Orbital Angular Momentum, Spin State, Transition, and Wavelength.

Electron Configuration	ℓ	S	Transition	Wavelength [Ang]
$1S^1$	0	0	N/A	N/A
$1S^12S^1$	0	1	$1^1S \rightarrow 2^3S$	625.56
		0	$1^1S \rightarrow 2^1S$	601.41
$1S^12P^1$	1	1	$1^1S \rightarrow 2^3P$	591.42
		0	$1^1S \rightarrow 2^1P$	584.33
$1S^13S^1$	0	1	$1^1S \rightarrow 3^3S$	545.74
		0	$1^1S \rightarrow 3^1S$	540.94
$1S^13P^1$	1	1	$1^1S \rightarrow 3^3P$	538.89
		0	$1^1S \rightarrow 3^1P$	537.33
$1S^13D^1$	2	1	$1^1S \rightarrow 3^3D$	537.33
		0	$1^1S \rightarrow 3^1D$	537.33
$1S^14S^1$	0	1	$1^1S \rightarrow 4^3S$	525.49
		0	$1^1S \rightarrow 4^1S$	523.72
$1S^14P^1$	1	1	$1^1S \rightarrow 4^3P$	522.97
		0	$1^1S \rightarrow 4^1P$	522.34
$1S^14D^1$	2	1	$1^1S \rightarrow 4^3D$	522.34
		0	$1^1S \rightarrow 4^1D$	522.32
$1S^14F^1$	3	1	$1^1S \rightarrow 4^3F$	522.32
		0	$1^1S \rightarrow 4^1F$	522.21

In Table 4.1.B the spin state (S) determines whether transition is a triplet or single state. For example, if the transition is a singlet state then its excited spin will be anti-parallel or the same as the ground state spin and S $= \frac{1}{2} - \frac{1}{2} = 0$ and will be denoted by a 1 in the transition. If it is a triplet state then the excited state spin will be parallel to the ground state spin and S $= \frac{1}{2} + \frac{1}{2} = 1$ and is denoted by a 3 in the transition.

Vitae

Holly Ray was born in Murfreesboro, TN on March 14, 1991 to James G. and Nancy K. Ray. She was raised in McMinnville, TN with her only sister, Elisha F. Locke, where she attended Warren County High School before leaving to attend American University in Washington, D.C. During her time in D.C. she interned for Senator Lamar Alexander of Tennessee and learned that the best way to influence science policy was through a technical background. In the Summer of 2011, she moved back to Knoxville, TN in anticipation of attending the University of Tennessee, Knoxville for her bachelors in nuclear engineering. As an undergraduate she participated in several research internships at Oak Ridge National Laboratory (ORNL). After graduating with a B.S. in nuclear engineering in May of 2013, she accepted a post-bachelor's position at ORNL. In August of 2015 she became a graduate student in the Bredesen Center for Interdisciplinary Research at UTK, doing research on the Prototype Material Plasma Exposure Experiment (Proto-MPEX). In the Spring of 2020, she successfully defended her dissertation and graduated with a Ph.D. in Energy, Science, and Engineering from the University of Tennessee. Following graduation, she went on to accept a position at the Savannah River National Laboratory in South Carolina.